LIVER-SPECIFIC DELIVERY OF MDM2 ANTISENSE OLIGONEUCLEOTIDES COUNTERACTS DIET-INDUCED METABOLIC DYSFUNCTION-ASSOCIATED STEATOTIC LIVER DISEASE IN MOUSE MODELS

HOQUE MD MOINUL

PhD

The Hong Kong Polytechnic University

2025

The Hong Kong Polytechnic University

Department of Health Technology and Informatics

Liver-specific delivery of MDM2 antisense oligoneucleotides counteracts diet-induced metabolic dysfunction-associated steatotic liver disease in mouse models

HOQUE Md Moinul

A thesis submitted in partial fulfilment of the requirements for the degree of Doctor of Philosophy

April 2025

CERTIFICATE OF ORIGINALITY

I hereby declare that this thesis is my own work and that, to the best of my knowledge and belief, it reproduces no material previously published or written, nor material that has been accepted for the award of any other degree or diploma, except where due acknowledgment has been made in the text.

_____

HOQUE MD MOINUL

Date- 30th April 2025

DEDICATION

Dedicated to my parents.

Abstract

Metabolic dysfunction-associated steatotic liver disease (MASLD) encompasses a spectrum of pathogenic conditions ranging from steatosis, inflammation and fibrosis. This chronic metabolic disease progresses through multiple mechanisms, and the treatment options remain limited. We previously demonstrated an upregulation of hepatic murine double minute 2 (MDM2) in human subjects with MASLD, highlighting its potential role as therapeutic target. Genetic deletion of hepatic MDM2 and pharmacological inhibition of systemic MDM2 improves steatosis and fibrosis in mouse models. In this study, we developed and investigated the therapeutic potential of triantennary N-acetylgalactosamine (GalNAc)-conjugated antisense oligonucleotide targeting MDM2 (GalNAc-Mdm2ASO) in two diet-induced mouse models of MASLD: a high-fat-high-cholesterol (HFHC) diet and a choline-deficient L-amino acid-defined high-fat diet (CDAHFD). In the HFHC-induced MASLD model, GalNAc-Mdm2ASO not only alleviated liver injury, steatosis, and fibrosis but also improved obesity-related insulin resistance and hyperlipidaemia. The hepatoprotective effects of GalNAc-Mdm2ASO treatment were associated with a reduced accumulation of hepatic cholesterol and ceramide, both of which are known to trigger MASLD. In CDAHFD mouse model, GalNAc-Mdm2ASO significantly mitigated hepatic inflammation, cholesterol accumulation and fibrosis but not triglyceride accumulation. Overall, we prove hepatic inhibition of MDM2 using GalNAc-Mdm2ASO as a promising therapeutic agent for MASLD in two rodent models with distinct pathogenesis.

Graphical abstract

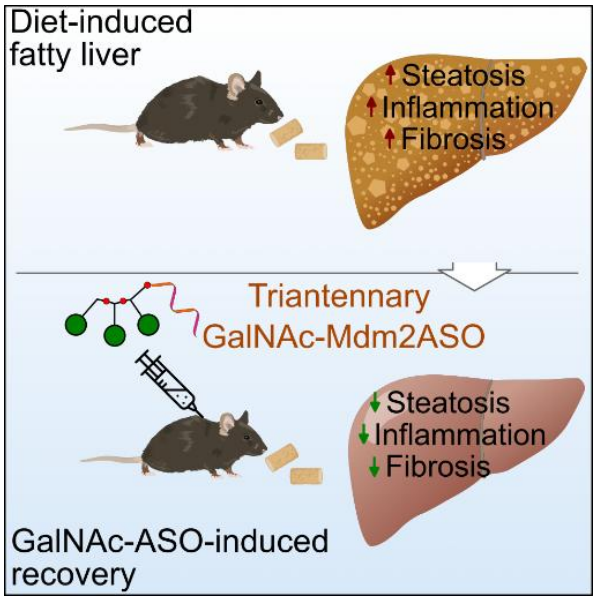

Highlights

- GalNAc-Mdm2ASO selectively reduced MDM2 expression in hepatocytes.
- Alleviated fatty liver conditions in two animal models.
- Decreased hepatic and serum cholesterol levels.

Conferences/symposiums and publications:

1) Hoque, Md Moinul, Lin Huige, Kenneth, King-yip Cheng. Hepatocyte specific delivery of MDM2 antisense oligonucleotides counteracts dietary-induced non-alcoholic fatty liver disease in the mouse model. Annual Scientific Meeting & Annual General Meeting organised by Hong Kong Society of Endocrinology, Metabolism, and Reproduction Limited (HKSEMR), HK, 24th November 2024 (Poster presentation).
2) Hoque, Md Moinul, Lin Huige, Kenneth, King-yip Cheng. Targeted delivery of MDM2 antisense oligonucleotides to hepatocytes counteracts dietary-induced metabolic dysfunction-associated steatotic liver disease in the mouse model. 7th China Endocrinology and Metabolism Pathophysiology Symposium, 15-17th November 2024 (Poster presentation).
3) Hoque, Md Moinul, Lin Huige, Kenneth, King-yip Cheng. Targeted delivery of MDM2 antisense oligonucleotides to hepatocytes counteracts dietary-induced metabolic dysfunction-associated steatotic liver disease in the mouse model. HTI Postgraduate Symposium, 7th June 2024 (Oral presentation).

Acknowledgments:

This thesis represents the culmination of a long and challenging journey that began with a detour from another path during the COVID-19 pandemic. While there were times I navigated this journey alone, I am deeply grateful for the moments when I had the guidance and support of many individuals, whom I wish to thank.

First and foremost, this research would not have been possible without my supervisor, Dr. Kenneth Cheng, who not only developed this research topic but also secured the funding to make it a reality. I am profoundly grateful to him for allowing me the freedom to pursue my own vision in exploring cutting-edge omics technology, which has opened up an entirely new area for my future career. At the same time, he adeptly kept me aligned with the project's framework whenever I began to stray. I would like to express my gratitude to Dr. Lin Huige. The dedication she showed during the manuscript preparation is truly exceptional and rarely seen. I would like to thank Dr. Gloria for her assistance in trouble-shooting the Rna-seq data analysis.

My deepest gratitude goes to my lab members—Dr. Kelvin, Dr. Jun Tao, Dr. Kekao Long, Dr. Kong Mengjie, Dr. Shama Mansoori, Thashma, Becca, Joseph, Tongxi, Tiff, Eva, Baomin, Melody, Xin Yi, Amber, Chico—who were there from the very beginning till now. I cannot imagine what my PhD journey would have been like without their unwavering support and advice, whether in discussing methodologies, troubleshooting or emotional support. Special thank goes to my long old friend, Thashma, without whom my PolyU journey would not have started. Dr. Kong Mengjie was a big source of my mental support who not only taught me animal experiments but also broadened my horizons beyond the lab. Together, we enjoyed amazing hiking and sightseeing activities. Melody, a good listener, a sink to dump my idiosyncratic ideas. Tongxi is always there to provide me with food during those odd hours in the office, and our conversations consistently offer me new perspectives to consider. Whenever I find myself lacking in critical thinking, I turn to Shama for guidance. Dr. Jun Tao’s entertaining and lighthearted personality always brought a sense of joy and levity to our work.

I am grateful to Tiff and Becca for their sincere help during my conference trip to Shenzhen. Dr. Huige is a role model for her serious demeanor and swift actions.

Speaking of my parents, who vicariously experienced every up and down of this PhD with me and kept things going whenever I was full of self-doubt. I couldn't have made it this far without their unconditional love and support.

Finally, I am grateful to the funding agency, Shenzhen Natural Science Foundation Basic research, to support this project and the Research Grant Council, for providing me generous support through PolyU Presidential PhD Fellowship Scheme.

Table of content

List of figures

List of tables

Chapter 1: Introduction

1.1 Obesity and metabolic dysfunction-associated steatotic liver disease

Obesity is a major public health issue, with its prevalence rising alarmingly in recent decades. It is generally defined as excessive fat accumulation in the adipose tissue that presents a risk to health. One of the most concerning consequences of obesity is its strong association with metabolic dysfunction-associated steatotic liver disease (MASLD), formerly known as non-alcoholic fatty liver disease (NAFLD) [1]. A key aspect of MASLD is the accumulation of ectopic fat in liver without significant alcohol consumption. When adipose tissue exceeds its storage capacity, triglycerides (TG) mobilizes to other organs like the liver, leading to ectopic fat deposition [2] (Figure 1.1).

Depending on the amount and duration of accumulated fat inside the hepatocytes, MASLD represents a spectrum of disease. It benigns with benign steatosis, or fatty liver, where liver fat exceeds 5% of liver weight [3], and can progress to non-alcoholic steatohepatitis (NASH), now referred to as metabolic dysfunction-associated steatohepatitis (MASH) [1]. MASH is a serious condition, with 10–25% of patients eventually developing cirrhosis [4]. This stage is marked by lobular and portal inflammation, hepatocyte ballooning, and differing degrees of fibrosis, cirrhosis, and potentially hepatocellular carcinoma (HCC) [5]. The pathogenesis of MASLD involves a complex interaction among multiple factors such as diet, obesity, inflammation, changes in gut microbiota, and genetic predispositions, all of which contribute to dysregulated lipid metabolism. The prevalence of MASLD has been increasing worldwide, driven in part by the rise in obesity rates. In Western countries, the condition affects an estimated 20-40% of the general population, while in Asia-Pacific regions, the prevalence ranges from 12-24% in various subgroups [6]. Indeed, epidemiological surveys have shown that the annual prevalence of NAFLD has been rising due to an oversupplied lifestyle, reaching approximately 25% globally [7].

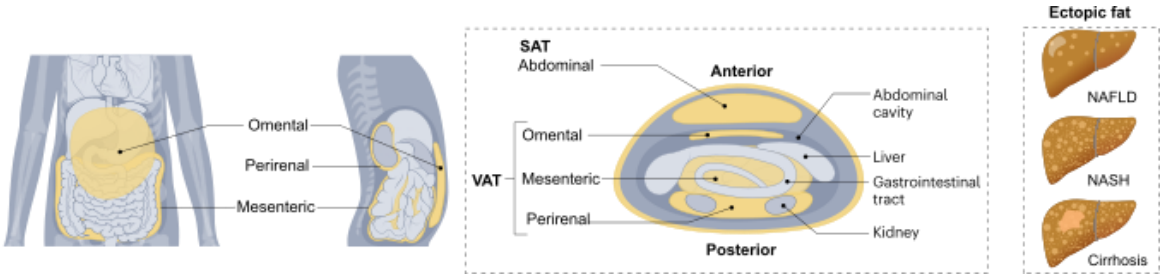

Figure 1.1. Accumulation of ectopic fat from the adipose tissue leads to MASLD.

1.2 Liver as a metabolic hub in lipid metabolism

The liver is essential for lipid metabolism, serving as a central hub for the synthesis, storage, and distribution of lipid molecules, all tightly regulated by various interrelated transcriptional and signaling pathways. It is responsible for producing triglycerides, cholesterols and other lipid species, which are then transported to various tissues throughout the body. Additionally, the liver regulates the breakdown and clearance of lipids, playing a crucial role in maintaining overall lipid homeostasis. In MASLD, alterations in this delicate balance of lipid metabolism can lead to the accumulation of ectopic fat in the liver.

1.3 Triglyceride metabolism in normal- and patho-physiology

TG metabolism, under normal physiological conditions, encompasses two distinct nutritional state: the fed state and the fasted state. In the fed state, insulin promotes *de novo lipogenesis* (DNL) which induces carbohydrate metabolism in the liver to produce FA via the activation of transcription factors such as sterol regulatory element binding protein 1c (SREBP-1c) and carbohydrate response element binding protein (ChREBP) [8, 9]. In addition to carbohydrates, dietary lipids are hydrolyzed in the intestinal lumen, transported to the liver, and processed intracellularly, leading to FA release within hepatocytes. Within the hepatocyte, FA are esterified to TG which can be either stored in cytoplasmic lipid droplets (LDs) or secreted into bloodstream as VLDL particles. In the fasted state, fatty acids from the plasma make up the primary source of hepatic triglycerides [10]. When plasma insulin levels are low during fasting, a lipolytic program is activated in white adipose tissue, leading

to an increase in the plasma FA pool available for liver uptake [11]. Once these FAs enter the liver, they serve both as a local energy source and as substrates to produce ketone bodies.

In the context of overnutrition and insulin resistance which leads to pathophysiological conditions, hepatic FA levels rise due to enhanced lipolysis within adipocytes [12]. This results in elevated circulating FA concentrations and increases hepatic DNL. The excess FAs cannot be fully metabolized through oxidative pathways and are instead channeled towards the synthesis of triglycerides, leading to enhanced hepatic triglyceride storage and overproduction of very low-density lipoproteins.

1.4 Cholesterol metabolism in normal- and patho-physilogy

The liver plays a key role in cholesterol homeostasis. Under normal physiological conditions, this homeostasis is maintained through input and output pathways, including *de novo* cholesterol synthesis (70% of input), dietary absorption (30% of input), LDL-receptor-mediated uptake, and excretion [13].

Cholesterol synthesis is a multistep enzymatic process. The first step of this process is catalyzed by 3 hydroxy 3 methylglutaryl -CoA synthase (HMGCS) and occurs in cytosol, while subsequent steps take place in the endoplasmic reticulum (ER), making ER the primary site for cholesterol synthesis [14]. The process begins with acetyl-coenzyme A (Co-A), derived from mitochondria and transported to the cytosol. One molecule of acetyl-Co-A combines with one molecule of acetoacetyl-CoA to form HMG-CoA, which is then reduced to mevalonate by HMG-CoA reductase (HMGCR). Mevalonate undergoes further phosphorylation to become isopentyl pyrophosphate, which is converted to geranyl pyrophosphate. Condensation with another isopentyl pyrophosphate results in farnesyl pyrophosphate. Squalene synthase then catalyzes the condensation of two farnesyl pyrophosphate molecules to produce squalene. Squalene is subsequently cyclized into lanosterol, which is eventually converted into cholesterol through 19 additional reactions. Both HMGCR and SQLE are rate-limiting enzymes and are regulated by transcriptional and posttranslational mechanisms that provide negative feedback based on cellular cholesterol levels [15].

A reduced cellular cholesterol level activates the master transcription factor—sterol regulatory element-binding protein isoform 2 (SREBP-2)—to induce the expression of both enzymes [15-17]. In contrast, elevated cholesterol levels promote the ubiquitination and subsequent degradation of HMGCR and SQLE [18-20].

Besides *de novo* cholesterol synthesis in the liver, LDLR-mediated lipoprotein uptake serves as another input pathway to clear excess blood cholesterol. This process involves the uptake of circulating cholesterol carried by lipoprotein particles, including chylomicron remnants (CR), intermediate-density lipoprotein (IDL), high-density lipoprotein (HDL), and low-density lipoprotein (LDL) [21]. The LDL uptake is regulated by feedback inhibition: when cellular cholesterol is high, SREBP2 is inhibited, leading to a reduction in LDLR transcription. This mechanism helps prevent cholesterol accumulation within cells. In pathogenic conditions, however, the oxidative stress generates oxidized LDL (OxLDL) [22], which can lead to lipotoxicity.

Dietary cholesterol absorption is a key source of cholesterol for maintaining homeostasis. Cholesterol from food is transported from the gut to the liver through the aqueous environments of lymph and blood. For this long-distance transport, enterocytes in the gut and hepatocytes in the liver encapsulate cholesterol and cholesteryl esters into lipoproteins of different sizes and compositions, which are further modified in the bloodstream. In brief, in the enterocytes, dietary cholesterol is packaged into chylomicrons along with triglycerides and apolipoprotein B (ApoB)-48 and crosses the brush-border membrane.

To prevent hepatic cholesterol accumulation, hepatocytes must efficiently remove excess cholesterol from the liver. One primary pathway for this is the packaging of cholesterol along with triglycerides, ApoB-100 and microsomal triglyceride transfer protein (MTTP) into very low-density lipoproteins (VLDL), which are then secreted into the circulation. From the circulation, VLDL delivers cholesterol and triglycerides to peripheral tissues, eventually transforming into low-density lipoprotein (LDL) after losing triglycerides [23]. Defects or inhibition of the packaging proteins-

ApoB and MTTP- can lead to hepatic lipid overload and contribute to the development of MASH and hepatocellular carcinoma (HCC) [24, 25].

Another key process for exporting cholesterol from liver is its conversion into bile acids through a series of enzymatic pathway, which helps eliminate some cholesterol. The rate-limiting enzyme in this process is cytochrome P4507A1 (CYP7A1). In humans, ileum enterocytes produce fibroblast growth factor 19, while in mice, they produce fibroblast growth factor 15, both of which inhibit CYP7A1 expression upon bile acid uptake

1.5 Hepatic macrophages in the healthy and MASH liver

The liver is a crucial organ for metabolism, detoxification, and immune function, housing many innate and adaptive immune cells [26]. Its highly vascularized structure, featuring fenestrated sinusoids, enhances immune cell exposure to pathogens from the bloodstream and gut [27, 28]. Approximately one-third of the body's blood volume flows through the liver each minute. The majority of this blood enters the liver through the portal vein, which drains blood from the gastrointestinal tract and the remaining 20-25% of the blood supply comes from the hepatic artery [29]. Within the liver, a wide range of lymphoid and myeloid cell lineages can be found. These immune cells primarily reside in the sinusoids but can also be found in the intravascular and subcapsular compartments of the liver [26, 30]. From an immunological perspective, the liver capillary system is lined with specialized cells that play important roles in immune responses. These include sinusoidal endothelial cells, Kupffer cells, and liver dendritic cells [26]. These specialized cells are responsible for initiating and shaping immune responses in the liver. Their antigen-presenting abilities, as well as their production of cytokines and chemokines, contribute to the regulation and modulation of liver immune responses.

Single-cell transcriptomics have provided valuable insights into how the immune cell repertoire is altered during non-alcoholic steatohepatitis (NASH) in mice [31, 32] and humans [33]. These studies show significant alterations in the myeloid compartment, particularly an influx of monocytes and monocyte-derived cells, which likely contribute to the inflammation driving liver

injury and NASH progression. The interactions between immune cells and liver cell types, such as hepatocytes and hepatic stellate cells, are crucial in NASH pathogenesis, though these dynamics are still being explored. Overall, advanced techniques like single-cell transcriptomics promise to enhance our understanding of immune cell dynamics and intercellular communication in NASH development.

1.6 MDM2 biology and its role in lipid homeostasis

Murine Double Minute 2 (MDM2) belongs to a large family of (Really Interesting New Gene) RING-finger-containing proteins and functions mainly as an E3 ligase [34]. Like other members in the E3 ligase, MDM2 regulating their substrates by mono- and/or poly-ubiquitylation and consequently controlling their levels by proteasome-dependent degradation and/or by changing their localization, e.g., nuclear export [35]. Conventionally, MDM2 is well known negative regulator of p53 tumor suppressor gene in different types of cancer. MDM2 is one of three highly amplified genes (MDM1, MDM2 and MDM3) initially discovered in spontaneously transformed Balb/c mouse 3T3 fibroblast cell line [36]. Soon after, it was found that MDM2 oncogene product forms a tight complex with the p53 tumor suppressor protein and amplification of MDM2 in human soft tissue sarcomas leads to escape from p53-regulated growth control [37, 38].

In addition to its well-known role in cancer biology regulating cell-cycle arrest, cell death and senescence, the MDM2-p53 signaling axis has been found to play a crucial role in lipid and glucose homeostasis [39-41]. This highlights the versatile nature of MDM2's involvement in various biological processes. It turns out, p53 acts as a mediator of cellular stress response by sensing and responding to a variety of stresses including both oncogenic and non-oncogenic insults. For example, excessive calorie intake can lead to oxidative stress accumulation in adipose tissue, triggering the expression of p53 [42]. This, in turn, results in increased production of proinflammatory cytokines. Inhibition of p53 has been shown to decrease the expression of proinflammatory cytokines and improve insulin resistance in mice with a disease similar to type 2 diabetes [42]. Furthermore, the accumulation of p53 has been observed in hepatocytes of patients with fibrotic liver diseases [43].

While involvement of p53 in metabolic regulation has been extensively studied, the role of its binding partner MDM2 in this context is relatively less understood. However, there is evidence suggesting that MDM2 has p53-independent functions in metabolic regulation. One study demonstrated that MDM2 acts as a transcription factor during the early stages of adipocyte differentiation, independent of its role in p53 regulation [44, 45]. This suggests that MDM2 may contribute to the development and function of adipose tissue through direct transcriptional regulation. Another study showed that genetic disruption of MDM2 in adipocytes triggers canonical p53-mediated apoptotic and senescent programs, leading to age-dependent lipodystrophy and its associated metabolic disorders, including type 2 diabetes, nonalcoholic fatty liver disease, hyperlipidemia, and energy imbalance [46]. This suggests that MDM2 plays a critical role in maintaining adipose tissue homeostasis and metabolic health. This further supports the involvement of MDM2 in metabolic regulation, particularly in adipose tissue. Additionally, hepatocyte-specific deletion of MDM2 in mice has been shown to activate the transcription factor CTGF (connective tissue growth factor) in a p53-dependent pathway, which increases hepatocyte apoptosis, and spontaneous liver fibrosis [43]. Overall, the available evidence suggests that MDM2 plays a role in metabolic regulation through both p53-dependent and p53-independent mechanisms, highlighting its versatile functions in metabolic homeostasis and associated disorders.

1.7 Evolution of gene silencing approaches

To understand the function of a gene in their behavior, we need to choose appropriate intervention method either by knock out (KO) or knock down (KD) approach. These intervention studies can be broadly categorized as pharmacological and genetic approach with each of them have certain advantages and disadvantages. For example, the pharmacological arms utilize a protein-protein interaction that acts as agonists or antagonists to target the protein of interest. However, they also bind to the off-target proteins. Additionally, the process of designing and developing new drugs can be time-consuming, complex, and expensive [47]. On the other hand, the genetic approach that utilizes various transgenic strategies are more versatile, provides the ability to target any number of

genes with great precision and cost-effective manner [48]. One commonly used genetic approach is the CreLoxP system, where specific genes can be knocked out in a tissue-specific manner by crossing mice carrying the gene of interest flanked by LoxP sites with mice expressing the Cre recombinase under tissue-specific control. Overall, while pharmacological approaches offer the advantage of targeting specific proteins, genetic approaches provide greater versatility and precision in manipulating gene function in a cost-effective manner.

Alongside transgenic mouse models, RNA interference (RNAi) techniques have been developed as a means to control gene expression. In the RNAi techniques, long double stranded RNA (dsRNA) is processed by the enzyme Dicer into small interfering RNA (siRNA). These siRNAs are then loaded into the RNA-induced silencing complex (RISC), which recognizes and targets mRNA molecules for degradation [49]. Antisense oligonucleotide (ASO) mediated knockdown is another widely used method for gene silencing. ASO's are generally DNA molecules instead of RNA. These single-stranded molecules inhibit gene expression without requiring Dicer processing or the RNA-induced silencing complex (RISC) [50]. ASO's work by utilizing the Watson-Crick base pairing between an oligonucleotide and its cognate mRNA to inhibit gene expression at the mRNA level. The hybrid-arrest and RNase H activation are two major mechanisms proposed for ASO-mediated knockdown [51].

In recent years, researchers have focused on developing cell specific delivery of ASO by conjugation of moieties that take advantage of high-capacity receptors such as the asialoglycoprotein receptor (ASGPR) expressed by hepatocytes [52-54]. One such example is the ASO conjugated with triantennary N-acetyl galactosamine (GalNAc3), a high-affinity ligand for the ASGPR. This ASO-GalNAc3 can substantially improve drug distribution to the hepatocytes and resulted in significant improvements in potency [53]. These advancements in ASO technology and cell-specific delivery strategies have improved the stability, specificity, and efficacy of ASO-mediated knockdown, making them a powerful tool for inhibiting gene expression and exploring gene function without the need for transgenic models or complex delivery systems.

1.8 General aim of the study

This project aims to investigate whether the N-acetylgalactosamine (GalNAc) conjugated MDM2 antisense oligonucleotides (ASO) (so-called GalNAc-Mdm2ASO hereafter) counteracts diet-induced MASLD in the mouse models. To test and validate this hypothesis, we conducted the following specific aims:

Aim 1: Established two diet-induced MASLD/MASH mouse models: a high-fat, high-cholesterol (HFHC) model and a choline-deficient, L-amino acid-defined high-fat diet (CDAHFD) model.

Aim 2: Established liver-specific MDM2 knockdown (KD) using GalNAc-Mdm2ASO in the two diet-induced MASLD/MASH mouse models.

Aim 3: Assessed the metabolic benefits of hepatocyte-specific MDM2 knockdown on MASLD/MASH development, evaluating changes in lipid metabolism and other pathways, such as inflammation.

Chapter 2: Materials and Methods

2.1 Materials:

Table 2.1. Chemicals and reagents

Chemical/ reagent	Name of company	Catalog no.
For RNA isolation and qPCR		
RNAiso plus (Trizol)	TaKaRa	#9101
Absolute Ethanol	Sigma-Aldrich	#459844
Isopropyl alcohol	DUKSAN	#d2377
QuantiNova SYBR Green PCR Kit	Qiagen	#208057
For western blotting		
Acryl/Bis 30% Solution (acrylamide solution)	Sangon Biotech Co., Ltd.	#B546018-0500
Ammonium Persulfate (APS)	Sigma-Aldrich	#A3678
TEMED	Thermo Fisher Scientific	#17919
PVDF membrane	SOLARBIO	#BSP0161
Protease Inhibitor Cocktail	MedChemExpress	#HY-K0010
Phosphatase Inhibitor Cocktail	Bimake	#B15002
2-Mercaptoethanol	Bio-Rad	#1610710
PageRuler™ Plus Prestained Protein Ladder	Thermofisher	#26620
Bovine serum albumin (BSA)	Sigma-Aldrich	#05470
Medical X-ray film	Fuji film	#Super HR-U30
Clarity Western ECL Substrate	Bio-Rad	#1705061
Clarity Max Western ECL Substrate	Bio-Rad	#1705062
For Histological analysis		
10% neutral buffered formalin	Epredia	#110909
Histological paraffin	Thermo Fisher Scientific	#8331
Xylene	Sigma-Aldrich	#185566
Absolute ethanol	Sigma-Aldrich	#459844
Haematoxylin	SOLARBIO	#G1121
Adhesive Glass Slide	Matsunami Glass	#210268W-SP6E
Cryomatrix	Epredia	#112070

Eosin	SOLARBIO	#G1121
DAPI	Thermo Fisher Scientific	#P36985
DPX mountant	Sigma-Aldrich	#06522
Acetic acid	VWR	#64-19-7
Picro Sirius Red Solution	Abcam	#ab246832
Oil Red O	powder Hopkin & Williams	#11950
Others		
Pierce™ TMB Substrate Kit	Thermofisher, USA	#34021
Glucose	FLUKA	#49138
Tyloxapol	*Sigma-Aldrich*	*#T8761*
Ketamine (10%)	*Alfasan International B.V.*	*#0904088-05*
Xylazine (2%)	*Alfasan International B.V.*	*#1205117-05*
High fat high cholesterol diet (HFHC)-Mice diet	*Research Diets, Inc. USA)*	*# D12079Bi*
Choline-deficient L-amino acid defined high-fat diet (CDAHFD)	Research Diets Inc, USA	# A06071309

Table 2.2. Biochemical Assays/Kits

Name	**Name of company**	**Catalog no.**
Pierce™ BCA Protein Assay Kit	Thermofisher	#23225
Mouse IL-1 beta/IL-1F2 DuoSet ELISA	R&D Systems	#DY401
Mouse CCL2/JE/MCP-1 DuoSet ELISA	R&D Systems	#DY479
Mouse Adiponectin ELISA kit	ImmunoDiagnostics Limited	#32010
Reverse transcription kit	Promega	#15596026
Stanbio Cholesterol LiquiColor®	Stanbio Laboratory	#1010
Stanbio LDL LiquiColor®	Stanbio Laboratory	# 0710-080
Stanbio HDL LiquiColor®	Stanbio Laboratory	# 0590-080
Blood urea nitrogen kit	Solarbio	#BC1535
Stanbio ALT/GPT (Liqui-UV®)	Stanbio Laboratory	#2930

Stanbio AST/SGOT (Liqui-UV®)	Stanbio Laboratory	#2920
Stanbio triglyceride LiquiColor®	Stanbio Laboratory	#2100
NEFA assay kit	Nanjing Jiancheng Bioengineering Institute	#A042-2-1
β-hydroxybutyric acid detection	Nanjing Jiancheng Bioengineering Institute	
Serum insulin	Mercodia	#10-1249-01

Table 2.3. Primer sequence

Name of target	Forward primer (5'-3')	Reverse primer (5'-3')
Mus Mdm2	GGGAGTGATCTGAAGGATCC	CTCATCTGTGTTCTCTTCTGTC
Mus p53	ACTGCATGGACGATCTGTTG	GTGACAGGGTCCTGTGCTG
Mus Cdkn1a (p21)	GCAGATCCACAGCGATATCC	CAACTGCTCACTGTCCACGG
Mus Cdkn2a (p16)	CGCAGGTTCTTGGTCACTGT	TGTTCACGAAAGCCAGAGCG
Mus Puma	ATGGCGGACGACCTCAAC	AGTCCCATGAAGAGATTGTACATGAC
Mus Cd36	ACATTTGCAGGTCTATCTACG	AATGGTTGTCTGGATTCTGG
Mus Pparα	GGATGTCACACAATGCAATTCGC	TCACAGAACGGCTTCCTCAGGT
Mus Cpt1α	CTCCGCCTGAGCCATGAAG	CACCAGTGATGATGCCATTCT
Mus Mcad	GATCGCAATGGGTGCTTTTGATAGAA	AGCTGATTGGCAATGTCTCCAGCAAA
Mus Acly	ACCCTTTCACTGGGGATCACA	GACAGGGATCAGGATTTCCTTG
Mus Fasn	GGCTCTATGGATTACCCAAGC	CCAGTGTTCGTTCCTCGGA
Mus Dgat2	AGTGGCAATGCTATCATCATCGT	TCTTCTGGACCCATCGGCCCCAGGA
Mus Scd1	TTCTTGCGATACACTCTGGTGC	CGGGATTGAATGTTCTTGTCGT
Mus Pparg2	GCATGGTGCCTTCGCTGA	TGGCATCTCTGTGTCAACCATG
Mus Acta2	GCATCCACGAAACCACCTA	CACGAGTAACAAATCAAAGC
Mus Mmp2	ACCTGAACACTTTCTATGGCTG	CTTCCGCATGGTCTCGATG
Mus Mmp13	TGTTTGCAGAGCACTACTTGAA	CAGTCACCTCTAAGCCAAAGAAA
Mus Mmp14	ACCCACACACAACGCTCAC	GCCTGTCACTTGTAAACCATAGA

Mus Col1α1	CAATGGTGAGACGTGGAAAC	GGTTGGGACAGTCCAGTTCT
Mus Col3α1	CTGTAACATGGAAACTGGGGAAA	CCATAGCTGAACTGAAAACCACC
Mus Col4α1	CTGGCACAAAAGGGACGAG	ACGTGGCCGAGAATTTCACC
Mus Timp1	CTTGGTTCCCTGGCGTACTC	ACCTGATCCGTCCACAAACAG
Mus Tgf β	GCAACATGTGGAACTCTACCAGA	GACGTCAAAAGACAGCCACTCA
Mus Ctgf	GTGCCAGAAAGCACACTG	CCCCGGTTACACTCCAAA
Mus Hmgcr	AGCTTGCCCGAATTGTATGTG	TCTGTTGTGAACCATGTGACTTC
Mus Srebp2	GTGGAGCAGTCTCAACGTCA	TGGTAGGTCTCACCCAGGAG
Mus Cyp7a1	AGCAACTAAACAACCTGCCAGTACTA	GTCCGGATATTCAAGGATGCA
Mus Cyp7b1	AGCCGATTATCAGCGAAAGCC	GCATCCAAAGGTTTGCCTTGT
Mus Cyp27a1	GCACAGGAGAGTACGGAGG	CGGGCAAGTGCAGCACATA
Mus Cyp8b1	CACGGGGATGTCTTCACGG	TGAGCACCAGTTCTTTTGCATAG
Mus 18S	AGTCCCTGCCCTTTGTACACA	CGATCCGAGGGCCTCACTA
Mus Gapdh	CTCATGACCACAGTCCATGC	CACATTGGGGGTAGGAACAC
Mus Mcp1 (Ccl2)	CCACTCACCTGCTGCTACTCA	TGGTGATCCTCTTGTAGCTCTCC
Mus Cd68	TTGGGAACTACACACGTGGGC	CGGATTTGAATTTGGGCTTG
Mus F4/80	CTTTGGCTATGGGCTTCCAGTC	GCAAGGAGGACAGAGTTTATCGTG
Mus A-fabp4	CCGCAGACGACAGGA	CTCATGCCCTTTCATAAACT

Table 2.4. Buffers and their recipe

Buffer/ Medium	Composition
RIPA-lysis buffer	50 mM Tris HCl, 150 mM NaCl, 2 mM EDTA, 0.1% SDS, 1% NP-40 (pH: 7.4)
Phosphate-buffered saline (PBS)	137 mM NaCl, 2.7 mM KCl, 1.8 mM KH_2PO_4, 10 mM Na_2HPO_4 (pH: 7.4)
Tris-buffered saline (TBS)	150 mM NaCl, 20 mM Tris (pH: 7.6)
1XPBST	1 X PBS (pH: 7.4) with 0.1 % Tween-20
1XTBST	1 X TBS (pH: 7.4) with 0.1 % Tween-20
Antigen retrieval buffer	10 mM Tris base, 1 mM EDTA, 0.05% Tween-20 (pH: 9.0)
Blocking buffer for IF	10% fetal bovine serum (FBS) and 0.1% Triton-X100 detergent in 1XPBST
Primary diluent for IF	3% BSA and 0.1% Triton-X100 detergent in 1xPBS
Transfer buffer	192 mM glycine, 25 mM Tris
Running buffer	192 mM glycine, 25 mM Tris, 0.1% SDS
5Xloading dye	0.05% Bromophenol blue, 0.25M Tris-Cl (pH: 6.8), 50% Glycerol, 10% SDS
Blocking buffer for western blotting	5 % skimmed milk in 1 X TBST
10XTAE buffer	0.4 M Tris, 0.01 M EDTA, 0.2 M Acetic acid (pH:8.0)
ELISA diluent	1% BSA in 1XPBS buffer
EISA wash buffer	1xPBST added with 0.05% Tween 20
Complete DMEM	DMEM with 10% fetal bovine serum (FBS) and 1% solution of penicillin and streptomycin (PS)
Sirius red stain	0.5 g Sirius red powder in 500 mL of saturated acetic acid

Table 2.5. List of antibodies used

Antibody	Catalogue number and supplier	Usage and dilution
MDM2	#OP115, Calbiochem (EMD Millipore)	WB (1:1000), IHC (1:100)
α-SMA	#19245S, Cell Signaling Technology	WB (1:1000), IHC (1:80)
APOB	#sc393636, Santa Cruz	WB (1:1000)
CYP7B1	#24889-1-AP, Proteintech	WB (1:1000)
MPO	#AF3667, R&D Systems	WB (0.5 μg/ml)
β-ACTIN	#sc47778, Santa Cruz	WB (1:2000)
HSP90	#4874S, Cell Signaling Technology	WB (1:1000)

Table 2.6. Equipments and softwares

Equipment	Name of the company
Refrigerated CentriVap Centrifugal Concentrator and CentriVap Cold Traps	Labconco
NanoDrop 2000 Spectrophotometer Thermo Fisher Scientific	Thermo Fisher Scientific
96 Microplate Reader	Bio-Rad Laboratories
Real-Time PCR System	Applied Biosystems
Viia7 Real-time PCR	Applied Biosystems
Excelsior AS Tissue Processor	Thermo Fisher Scientific
Paraffin Embedding Station	Thermolyne™
Leica RM2235 (Manual microtome)	Leica Biosystems
Nikon Eclipse Ni-U Fluorescent Microscope	Nikon Instruments Inc.
Nikon Polarizing Microscope	Nikon Instruments Inc.
Accu-Check Performa Glucose Meter	Roche
Bruker minispec LF90II Body Composition Analyzer (The Hong Kong University)	Bruker
Software	
GraphPad Prism 8.0.1	GraphPad
ImageJ 1.50	NIH

2.2 Methodology:

2.2.1 Generation of ASOs

All ASOs were screened, synthesized and provided by Ionis Pharmaceuticals. The oligonucleotides used in this study were 16 nucleotides (3-10-3 cEt gapmer with PS backbone) in length and conjugated with N-Acetylgalactosamine on the 5'-end. ASO#2 used in this study were as follows: GalNAC-conASO 5'-GGCCAATACGCCGTCA-3'; GalNAC-Mdm2ASO 5'-GTAGAAATGTTTTTCC-3'.

2.2.2 Animal studies

Eight-week-old male wild-type C57BL/6J mice were obtained from the Centralized Animal Facilities of The Hong Kong Polytechnic University (CAF, polyU) or the Laboratory Animal Services Centre of The Chinese University of Hong Kong. The mice had free access to food and water and were housed in groups of four to six per cage under a 12-hour light/dark cycle, with humidity maintained at 60-70% and temperature at 23±1°C in the CAF, PolyU. All animal experiments were conducted in accordance with institutional guidelines and received approval from the Animal Subjects Ethics Sub-Committee (ASESC) at Hong Kong Polytechnic University (ASESC number 21-22/44-HTI-R-OTHERS). After a 2-week adaptation period, ten-week-old male C57BL/6J mice were randomly assigned to experimental groups and maintained on one of three diets: a standard chow diet (STC; 13.2% kcal fat, D5053, LabDiet, USA), a high-fat high-cholesterol diet (HFHC; 41% kcal fat with 0.15% cholesterol, D12079B, Research Diets Inc, USA), or a choline-deficient L-amino acid defined high-fat diet (CDAHFD; 45% kcal fat with 0.1% methionine, A06071309, Research Diets Inc, USA) [55] for a duration indicated in the individual figures. Their body weight and food intake were monitored weekly for each mouse.

For the *in vivo* hepatic MDM2 knockdown experiment, a subcutaneous injection of GalNAc-MDM2-ASO or GalNAc-Control ASO in 1X PBS solution was administered at a dose of 5 mg/kg/week for the duration specified in the individual figures. Three days after the final injection,

the mice were sacrificed, and blood plasma along with selected organs (liver, heart, kidney, spleen, and adipose tissues) were collected for further analysis.

2.2.3 Primary hepatocyte isolation

Primary hepatocytes were obtained by perfusing the mouse liver with a pre-warmed perfusion buffer (119.8 mM NaCl, 23.8 mM $NaHCO_3$, 1 M HEPES, 4.8 mM KCl, 1.2 mM $MgSO_4$, 1.2 mM KH_2PO_4 and 5.55 mM glucose, pH 7.4, 1% penicillin-sterptomycin) containing 1mM EGTA (catalog #324626, Sigma-Aldrich). This was followed by digestion using the same buffer with 0.5 mg/ml collagenase IV (catalog #C5138, Sigma-Aldrich) and 5mM $CaCl_2$. After digestion, the liver cell suspension was prepared in the chilled William's E medium (catalog #12551032, Gibco) supplemented with 10% FBS, 1% penicillin-sterptomycin and 2 mM L-Glutamine (catalog #25030081, Gibco). Next the cell suspension was filtered through a 100-µm cell strainer and centrifuged at 50g for 3 minutes at 4^0 C. Supernatant with non-parenchymal cells (NPC) was collected in a separate tube and the primary hepatocyte pellet was resuspended with 10 ml complete William's E medium. The live hepatocytes were estimated by trypan blue staining and stored in -80^0C for mRNA/protein extraction.

2.2.4 TG-VLDL secretion assay and TG clearance test

For the TG-VLDL secretion assay, mice fasted for 16 hours were intravenously injected with Tyloxapol (catalog #T8761, Sigma-Aldrich) at a dose of 500 mg/kg body weight. This injection inhibits lipolysis by lipoprotein lipase (LPL) and is commonly used to assess hepatic TG-VLDL production rates [56, 57]. For the TG-TC clearance test, 16-hour fasted mice were orally gavaged with olive oil at a dosage of 10 µl/g body weight.

Blood samples were collected from the tail vein before the administration of Tyloxapol or olive oil, and then at 1-hour intervals for 5 hours following the injection or gavage for both tests. The samples were kept at room temperature for 1 hour and then centrifuged at 7000 rpm for 10 minutes to collect serum. Serum TG and TC levels were measured according to the manufacturer's protocol using

the enzymatic assay kits (catalog #2100, Stanbio LiquiColor® Triglycerides; catalog #1010, Stanbio Cholesterol LiquiColor®).

2.2.5 Intra-peritoneal glucose tolerance test (IPGTT) and insulin tolerance test (ITT)

For IPGTT, mice were fasted for 16 hours, followed by intraperitoneal injection of D-glucose (catalog #346351, Sigma-Aldrich). For ITT, mice were fasted for 6 hours and then given an intraperitoneal injection of human recombinant insulin (catalog #91077C, Sigma-Aldrich). Blood glucose was measured using a glucometer (ACCU-Check Performa, Roche) and the dosage of D-glucose and recombinant insulin is mentioned in the figure legends.

2.2.6 Histological analysis and immunofluorescence staining

Liver samples were fixed in 10% neutral buffered formaldehyde solution (catalog #5735SSC, Epredia) for 24 hours, then processed using the Excelsior AS Tissue Processor (Thermo Fisher Scientific) and sectioned into 5-µm slices. The paraffin sections were deparaffinized with xylene and rehydrated in serial dilutions of ethanol (100%, 95%, 70%). The sections were stained with hematoxylin-eosin (catalog #G1121, SolarBio; H&E) and Picro Sirius Red (catalog #ab246832, Abcam), and images were captured using a light microscope (Serial #275948, Nikon Eclipse Ni, Japan) at 200X magnification. The images were then analyzed using ImageJ software.

For H&E staining, after deparaffinization and rehydration, the sectioned slides were stained with hematoxylin (a nuclear stain) for 2 minutes, followed by a quick dip in an acid alcohol solution. The slides were then stained with eosin (a cytoplasmic stain) for 3-5 minutes, dehydrated with two washes of 75% ethanol, cleaned in xylene, and mounted with DPX mountant (catalog #06522, Sigma-Aldrich). The slides were allowed to dry before imaging.

For Picro Sirius Red staining, following deparaffinization and rehydration, the sectioned slides were stained with Sirius Red (a collagen fiber stain) for 1 hour in the dark. After staining, the slides were quickly rinsed twice with fresh acidified water (0.5% glacial acetic acid) and dehydrated

three times with 100% ethanol. The tissue slides were then cleared with xylene for 10 minutes and mounted with DPX mountant.

For Oil Red O staining, frozen liver tissues embedded in OCT compound were sectioned to a thickness of 5 µm and then stained with Oil Red O (catalog #11950, Hopkin & Williams,) to visualize lipid droplets. The process began with fixing the slides in 10% neutral buffered formaldehyde for 10 minutes. After fixation, the slides were briefly immersed in 60% isopropanol for 5 minutes. They were then incubated in a filtered 0.3% Oil Red O solution for 30 minutes to stain neutral lipids. Following this, the slides were dipped in isopropanol for 1-2 seconds and rinsed in two changes of double-distilled water (ddH2O). Hematoxylin staining was carried out for 30 seconds, followed by thorough rinsing in tap water and two final rinses in ddH2O. Finally, the slides were coverslipped using an aqueous mounting medium.

For the immunohistochemistry staining of MDM2, deparaffinized and rehydrated sections were subjected to antigen retrieval in a proteinase K solution (20 µg/ml in TE buffer (50 mM tris base, 1mM EDTA, pH 8.0) for 3 minutes at room temperature. The sections were then treated with 0.3% H_2O_2 for 15 minutes and incubated with a blocking buffer (3% FBS, 3% BSA, and 0.01% Tween 20 in 1X PBS) for 30 minutes at room temperature. Following this, the sections were incubated with the MDM2 antibody (catalog #OP-115, EMD Millipore, mouse mAb, 1:100) at 4°C overnight in a humid dark chamber. After washing the slides three times with 1X PBST, they were incubated with a secondary antibody conjugated with HRP (1:200) (catalog #7076S, Cell Signaling Technology, Anti-mouse IgG) at room temperature for 1 hour. The slides were then washed again with 1X PBST and incubated with DAB solution (catalog #Ab64238, Abcam). Finally, the slides were counterstained with hematoxylin, mounted with DPX mountant, and images were captured.

For the immunohistochemistry staining of α-SMA, deparaffinized and rehydrated sections were subjected to antigen retrieval using a Tris-EDTA Buffer (10×10^{-3} M EDTA solution, 0.01% Triton-X 100, pH 9.0) at 60^0C for 20 minutes. The sections were then treated with 3% H_2O_2 for 4 minutes and incubated with a blocking buffer (10% FBS, 0.1% Triton-X 100 in 1X PBS) for 30

minutes at room temperature. Following this, the sections were incubated with the α-SMA antibody (catalog #19245S, Cell Signaling Technology, Rabbit mAb, 1:80) at 4°C overnight in a humid dark chamber. After washing the slides three times with 1X PBST, they were incubated with a secondary antibody conjugated with HRP (1:200) (catalog #7074S, Cell Signaling Technology, Anti-rabbit IgG) at room temperature for 1 hour. The slides were then washed again with 1X PBST and incubated with DAB solution (catalog #Ab64238, Abcam). Finally, the slides were counterstained with hematoxylin, mounted with DPX mountant, and images were captured. All images were captured using a light microscope (Serial #275948, Nikon Eclipse Ni, Japan) at 200X magnification. The images were then analyzed using ImageJ software.

2.2.7 Hepatic TG and TC content

Liver tissues were weighed using an analytical balance, with approximately 20-25 mg samples minced in 500 µL of 1X PBS buffer using a tissue homogenizer (Precellys Evolution Homogenizer, Bertin Technologies). 10 µL of the lysate was taken to measure protein concentration, while the remaining tissue lysate (490 µL) was mixed with 6 mL of a chloroform-methanol mixture (Chloroform: Methanol 2:1, v/v). This mixture was incubated overnight at 4°C. Following incubation, 1.2 mL of 0.7% NaCl solution was slowly added to each tube and incubated overnight at 4°C or for at least 24 hours. The liquid separated into two phases, with the salt solution and methanol on top and chloroform at the bottom. The chloroform layer, containing the hepatic lipids (lower layer), was collected. The solvent was air-dried using a vacuum evaporator, and the extracted hepatic lipids were resuspended in 100 µL of isopropanol, followed by sonication for 20 minutes. The levels of TG and TC were measured according to the manufacturer's protocol using enzymatic assay kits (catalog #2100, Stanbio LiquiColor® Triglycerides; catalog #1010, Stanbio Cholesterol LiquiColor®). Finally, the hepatic lipid levels were normalized to protein concentration.

2.2.8 Bile acid measurement

Bile acid concentrations in mouse bile were measured using a Total Bile Acid Colorimetric Assay Kit (catalog #E-BC-K181, Elabscience) following the manufacturer’s instructions. Briefly,

2 μL of bile was first diluted in 100 μL of PBS, followed by a further 1:100 dilution in PBS prior to measurement. A total of 5 μL of the diluted sample was mixed with assay reagents, and the reaction was incubated at 37°C. Absorbance was recorded at 405 nm using a microplate reader. Bile acid concentrations were calculated based on a standard curve and corrected for the total dilution factor. For biliary TC content, 5 μL of bile was diluted in 30 μL of isopropanol. After centrifugation, 5 μL of diluted samples was used for cholesterol measurement using enzymatic assay kits (catalog #1010, Stanbio Cholesterol LiquiColor®).

2.2.9 Biochemical and immunological analysis

Serum LDL (Catalog #0710-080, Stanbio Laboratory), HDL (Catalog #0590-080, Stanbio Laboratory), and free fatty acids (Catalogue# A042-2-1, Nanjing Jiancheng Bioengineering Institute) were measured according to the manufacturer's protocols.

Cholesterol and TG levels in different subclasses of lipoproteins were analyzed using proprietary gel-filtration high-performance liquid chromatography (BioRad).

The activity of alanine aminotransferase (ALT) and aspartate aminotransferase (AST) was determined using the ALT/SGP+ Liqui-UV test (catalog #2930/430, Stanbio Laboratory) and the AST/SGOT Liqui-UV test kits (catalog #2930/2920, Stanbio Laboratory). Serum adiponectin (catalog #32010, Immunodiagnostics Ltd.) was quantified using ELISA kits. MCP-1 levels in liver lysate and serum were assessed using the mouse MCP-1 DuoSet ELISA (catalog #DY479, R&D Systems). Serum urea and serum creatinine levels were measured using Blood urea nitrogen kit (catalog #BC1535, Solarbio) and Creatinine (Cr) Assay kit (sarcosine oxidase) (catalog #C011-2-1, Nanjing Jiancheng Bioengineering Institute), respectively. All measurements were conducted following the manufacturer's instructions.

2.2.10 Real-time PCR analysis

Total RNA from tissues were extracted using RNAiso Plus (catalog #9101, Takara) following the manufacturer’s instructions. cDNA was synthesized by reverse transcription of 1000 ng of RNA using the GoScript Reverse Transcription Kit (catalog #A2801, Promega) with random universal

hexamer primers. Quantitative real-time PCR was conducted using the Quantinova SYBR Green PCR Kit (catalog #208057, Qiagen) with gene-specific primers in the ViiA7 Real-time PCR System (Applied Biosystems). The gene expression level was analyzed using the ΔΔCT threshold cycle method and normalized against housekeeping gene *Gapdh*. Primer sequences are shown in Table 2.3.

2.2.11 Western blot analysis

Tissues were homogenised in a Radioimmunoprecipitation assay (RIPA) buffer (50 mM Tris HCl, 150 mM NaCl, 2 mM EDTA, 0.1% SDS, 1% NP-40, pH7.4), supplemented with 1µM DTT and a cocktail of protease inhibitors (catalog #HY-K0010, MedChemExpress, USA) and phosphatase inhibitors (catalog #B15002, Bimake, USA). An equal amount of proteins was separated by SDS-PAGE and transferred to a polyvinylidene difluoride (PVDF) membrane (catalog #1620177, Bio-Rad). For detection of ApoB in serum and liver tissues, protein was transferred using a modified transfer buffer (40×10^{-3} m Tris, 20×10^{-3} m sodium acetate, 2×10^{-3} m EDTA, pH 7.4, 10% v/v methanol, 0.005% w/v SDS) at 350 mA for 6 h at 4°C. The membrane was blocked with 10% non-fat milk in TBST and incubated with the primary antibody overnight at 4°C. Following this, the membrane was washed with TBST and incubated with corresponding secondary antibodies conjugated to horseradish peroxidase for 1 hour at room temperature. Specific protein signals were visualized using enhanced chemiluminescence reagents (catalog #1705061 & #1705062, Bio-Rad, USA), and the intensity of protein bands was quantified using ImageJ software. List of antibodies used in this study are tabulated in Table 2.5.

2.2.12 Body composition analysis

The body composition of mice including lean mass, fat mass, total body fat, and fluid content was measured *in vivo* with the use of Bruker minispec LF90II Body Composition Analyzer and data was collected. It utilizes the time domain-nuclear magnetic resonance (NMR) to access the mentioned parameters *in vivo*.

2.2.13 Animal sacrifice and collection of tissue samples

At the endpoint of the dietary treatment regime, mice were culled using the overdose of anaesthesia (ketamine and xylazine). The cardiac puncture was performed using a 25G needle to collect the blood samples. The blood samples were kept at RT for 3-4 hours for clotting and the serum was separated by centrifugation at 4000rpm for 15-20 minutes. The pellet was discarded, and the supernatant was centrifuged again to maximize the recovery of serum samples. The serum samples were kept at -80˚C until further use.

Following blood collection, different tissue samples were harvested, weighed, and snap-frozen in liquid nitrogen before putting them in -80˚C freezer storage. All tissue samples were kept at -80˚C. A small piece of tissue was put into a cassette (for tissue processing) and placed in 10% neutral formalin for fixation for 24 hours and further proceeded with Excelsior™ AS Tissue Processor.

2.2.14 RNA sequencing

RNA-seq (library preparation and sequencing run) was performed by the BGI Health (Hong Kong) and Novogene (Hong Kong). RNA from liver samples (approximately 20 mg) of GalNAc-conASO and GalNAc-Mdm2ASO groups (n=4) fed the HFHC/CDAHFD diet was extracted using the RNeasy mini kit (catalog #74104, Qiagen) following manufacturer's instructions. Total RNA was quantified with NanoDrop (Thermo Fisher) and quality control was performed using an Agilent Bioanalyzer system (Agilent Technologies). In the BGI Health, ribosomal RNA was depleted prior to library preparation, and the DNBseq sequencing platform was used for sequencing [58]. The Novogene facility utilized the Illumina platform to generate the raw sequence reads. Raw reads were mapped against the GRCm39 mouse genome assembly using STAR aligner (v2.7.10b) with the default options [59]. The number of reads mapped to each of genes was counted by using featureCounts of subread package (v 2.0.3) [60], with the option: -s 0 -p --countReadPairs -t exon -g gene_id. To visualize expression levels by principal component analysis (PCA), count data were first normalized using variance stabilized transformation (VST) method from DESeq2 R package (v1.36.0) Differential expression analysis was done using DESeq function from DESeq2 with default settings

[61]. The significance threshold was set to FDR < 5%, |log2FC| < 2 and base mean at least 20. Pathway enrichment was performed using QIAGEN IPA. Gene set enrichment analysis (GSEA) was performed using clusterProfiler (v4.4.4).

2.2.15 Targeted lipidomics

Sample preparation and lipid extraction: Targeted lipidomics using the multiple reaction monitoring (MRM) technique was performed at Applied Protein Technology, Shanghai Zhongke New Life Biotechnology Co. Ltd. Lipid extraction from liver samples (approximately 30-40 mg) of GalNAc-conASO and GalNAc-Mdm2ASO groups (n=4) fed the HFHC diet was conducted using the MTBE (Methyl tert-butyl ether) method [62]. Briefly, liver lysates were combined with 200 µL of methanol, followed by the addition of 10 µL of internal lipid standards and 800 µL of MTBE. The mixture was thoroughly vortexed and sonicated for 20 minutes at 4°C, then allowed to sit at room temperature for 30 minutes. Next, 200 µL of MS-grade water was added, and the mixture was vortexed and centrifuged at 14,000 rpm for 15 minutes at 4°C. The upper organic solvent layer was then collected and dried using liquid nitrogen. For LC-MS analysis, the samples were re-dissolved in 200 µL of Isopropyl alcohol/Acetonitrile (9:1, v/v) solvent and centrifuged at 14000 rpm at 4 ℃ for 15 min, then the supernatant was injected.

LC-MS/MS method for lipid analysis: The analysis was performed on a UHPLC system (LC-30AD, Shimadzu) coupled with QTRAP MS (6500+, Sciex). The analytes were separated on a C18 column (Phenomenex, Kinetex C18, 2.1 × 100 mm, 2.6 µm). The column temperature was set at 45℃. Mobile phase A consisted of 70% acetonitrile, 30% water, and 5 mM ammonium acetate, while mobile phase B was an isopropanol solution. A gradient was established, starting with 20% B at 0 minutes, increasing to 60% B at 5 minutes, reaching 100% B at 13 minutes, and returning to 20% B from 13.1 to 17 minutes, all at a flow rate of 0.35 mL/min. Throughout the analysis, the sample was kept at 10°C.

The 6500+ QTRAP (AB SCIEX) was operated in both positive and negative switching modes. The conditions for the ESI positive source were as follows: source temperature at 400°C, Ion Source

Gas 1 (GS1) at 50, Ion Source Gas 2 (GS2) at 55, Curtain Gas (CUR) at 35, and IonSpray Voltage (IS) at +3000 V. In negative mode, the source conditions remained the same except for the IonSpray Voltage (IS), which was set to -2500 V. The MRM method was employed for quantitative data acquisition in mass spectrometry. Additionally, pooled quality control (QC) samples were included in the sample queue to assess the system's stability and repeatability. *Data processing*: Sciex OS was used for quantitative data processing, with quality control (QC) samples analyzed alongside the biological samples. Metabolites in the QCs that exhibited a coefficient of variation (CV) of less than 30% were classified as reproducible measurements.

2.2.16 Mendelian randomization (MR) analysis

We used Version 8 release of the expression quantitative trait loci (eQTL) summarized data from the Genotype Tissue Expression (GTEx) project to identify the cis-eQTL genetic variant as the instrumental variables (IVs). The summary data-based MR (SMR) method extends this approach by integrating cis-eQTL data with genome-wide association studies (GWAS) data, which has been successfully applied to identify gene expressions that are pleiotropically or potentially causally associated with various complex phenotypes [63, 64]. GWAS summary statistics for ceramide and DG levels were derived from the study by Cadby et al. [65], which included 6,057 European participants. We used SMR method to perform Two-sample MR analysis by using gene expression of the MDM2 in the liver as the exposure, and ceramide and DG levels as the outcome. The threshold for the eQTL p-value was set at 5×10^{-6}, while the default values were used for other parameters [66]. The effect size estimate (β) from the SMR analysis represents the change in ceramide and DG levels associated with a 1-SD increase in MDM2 gene expression, as presented in (β [95% confidence interval (CI)]. The Inverse-Variance Weighted (IVW) method was used as the main MR analysis to assess the total effect of the exposure on the outcome, complemented by the weighted median and MR-Egger method. To assess the robustness of the IVW estimates, sensitivity analyses such as the weighted median method, the MR-Egger regression method, and the MR Pleiotropy RESidual Sum and Outlier method (MR-PRESSO) were performed.

2.2.17 Statistical analysis

All statistical analyses were conducted using Prism 8.0.1 (GraphPad Software Inc., La Jolla, CA, USA). Results are presented as means ± standard error of the mean (SEM), with sample sizes (n) for each experiment indicated in the figure legends. Prior to using parametric tests, data were assessed for normality and equal variance using the D'Agostino-Pearson omnibus test and Levene's test, respectively. For normally distributed data with equal variance, statistical significance was evaluated using a two-tailed Student's t-test, as noted in the figure legends. Nonparametric tests, such as the Mann-Whitney U test and Welch's T-test, were employed when data did not meet normality or variance assumptions. Two-tailed tests were used for analysis unless otherwise indicated. A p-value of less than 0.05 was considered statistically significant, represented as *$p < 0.05$, **$p < 0.01$, or specified in the figure legend. Animal experiments were performed once or twice, treating each animal as a biologically independent sample, and all experiments were repeated at least three times. In addition, all MR analyses were conducted using R version 4.4.1. SMR were conducted in version 1.3.1 [64]. Two sample MR analyses were performed using the TwoSampleMR package v.0.5.6 [67]. MR-PRESSO analysis was performed using “MRPRESSO” package [67].

Chapter 3: GalNAc-ASO conjugation allows for selective MDM2 reduction in the hepatocytes

3.1 Introduction

Antisense oligonucleotides (ASOs) are short, synthetic strands of nucleotides designed to bind specifically to target RNA sequences to regulate their expression. Initial progress in the oligonucleotide field faced challenges due to issues with stability, immune responses, and insufficient delivery to target tissues. The effectiveness of ASOs is influenced by their nucleotide sequence and any chemical modifications they possess. These modifications can enhance the ASO's functionality, stability, safety, and distribution throughout the body.

In this chapter, I will provide details on the preliminary screening process, including sequence selection, chemical modifications, and safety profiles. I will also discuss the specificity of the ASO using a mouse model.

3.2 Results

3.2.1 Identification and optimization of hepatocyte-targeted MDM2 Antisense Oligonucleotides

In preliminary screenings conducted by Ionis Pharmaceuticals, 315 oligonucleotides (oligos) were synthesized and tested *in vitro*. From this initial screening, 14 were selected for *in vivo* evaluation, leading to the identification of two lead candidates (ASO#03 and ASO#04) that effectively reduced *Mdm2* mRNA levels in the liver by approximately 80%. Importantly, this silencing was accomplished without significant adverse effects on liver and kidney function (Table 3.1). To generate hepatocyte specific delivery, ASO#04 was modified with 2′-O-methyl (2′-OMe) and constrained ethyl (2′ cEt) modifications conjugated with N-Acetylgalactosamine (GalNAc) on the 5’-end, resulting in GalNAc-Mdm2ASO. These modifications facilitate thermodynamic stability, increase nuclease resistance, and optimize its pharmacokinetic and pharmacodynamic profiles [68].

Table 3.1. Candidate Mdm2ASOs (ASO#03 and ASO#04) effectively reduce *Mdm2* expressions in the liver without causing adverse effects on liver and kidney function.

	% *Mdm2* mRNA			Liver function test			Kidney function test		
	Liver	Kidney	Heart	Albumin (g/dL)	ALT (U/L)	AST (U/L)	Bilirubin	Creatinine (mg/dL)	BUN (mg/dL)
PBS	100	100	100	2.85 ± 0.12	23.75 ± 1.71	32.75 ± 3.50	0.09 ± 0.01	0.16 ± 0.01	28.68 ± 2.12
ASO#1	17	27	44	2.93 ± 0.14	1933.50 ± 246.78	942.00 ± 222.03	0.21 ± 0.00	0.16 ± 0.04	27.90 ± 8.91
ASO#2	80	36	49	2.28 ± 0.11	1582.00 ± 231.93	1235.00 ± 403.05	6.18 ± 7.00	0.14 ± 0.07	16.95 ± 1.63
ASO#3	21	46	57	2.77 ± 0.04	38.00 ± 8.49	57.00 ± 4.24	0.12 ± 0.00	0.13 ± 0.02	24.95 ± 3.18
ASO#4	17	45	67	2.94 ± 0.09	138.50 ± 130.81	291.50 ± 330.22	0.21 ± 0.09	0.11 ± 0.03	17.00 ± 4.10
ASO#5	16	28	52	2.98 ± 0.14	571.00 ± 480.83	472.00 ± 74.95	0.24 ± 0.04	0.11 ± 0.03	15.30 ± 1.70
ASO#6	17	25	40	3.05 ± 0.04	703.00 ± 294.16	345.00 ± 104.65	0.18 ± 0.05	0.17 ± 0.05	16.90 ± 0.57
ASO#7	27	43	56	3.08 ± 0.09	357.00 ± 195.16	260.00 ± 15.56	0.16 ± 0.02	0.16 ± 0.06	18.70 ± 1.98
ASO#8	10	32	51	3.11 ± 0.05	260.50 ± 58.69	261.50 ± 17.68	0.16 ± 0.02	0.12 ± 0.01	21.80 ± 2.40
ASO#9	31	46	58	2.92 ± 0.23	197.00 ± 148.49	205.50 ± 96.87	0.13 ± 0.02	0.11 ± 0.01	26.65 ± 4.45
ASO#10	16	27	66	2.78 ± 0.05	211.50 ± 169	188.00 ± 72.12	0.12 ± 0.01	0.11 ± 0.01	26.10 ± 5.23
ASO#11	68	45	89	2.77 ± 0.06	208.00 ± 173.95	163.00 ± 107.48	0.10 ± 0.05	0.11 ± 0.01	23.35 ± 1.34
ASO#12	34	37	56	2.66 ± 0.10	254.50 ± 239.71	188.00 ± 142.84	0.09 ± 0.04	0.10 ± 0.00	22.40 ± 2.69
ASO#13	28	40	60	2.69 ± 0.14	398.50 ± 36.06	269.00 ± 28.28	0.11 ± 0.01	0.12 ± 0.02	20.90 ± 0.57
ASO#13	32	38	56	2.76 ± 0.04	316.00 ± 80.61	222.50 ± 37.48	0.11 ± 0.01	0.13 ± 0.00	23.60 ± 3.25

In a preliminary screening by Ionis Pharmaceuticals, 14 MDM2 antisense oligonucleotides (ASOs) were evaluated. To enhance targeted delivery, ASO#04 was modified with 2′-O-methyl (2′-OMe) and constrained ethyl (2′ cEt) modifications conjugated with GalNAc on the 5′-end, resulting in GalNAc-Mdm2ASO. Data represent mean ± standard deviation (n = 2).

3.2.2 GalNAc-Mdm2ASO confers selective MDM2 reduction in the hepatocytes but not in the NPC or other tissues

After selecting GalNAc-Mdm2ASO, we conducted an animal experiment to evaluate its specificity. To this end, we subcutaneously injected male C57BL/6J mice on the STC diet with either GalNAc-conASO or GalNAc-Mdm2ASO once weekly at a dose of 5 mg/kg per week for three weeks. Liver fractions and other tissues were collected three days following the final injection (Figure 3.1).

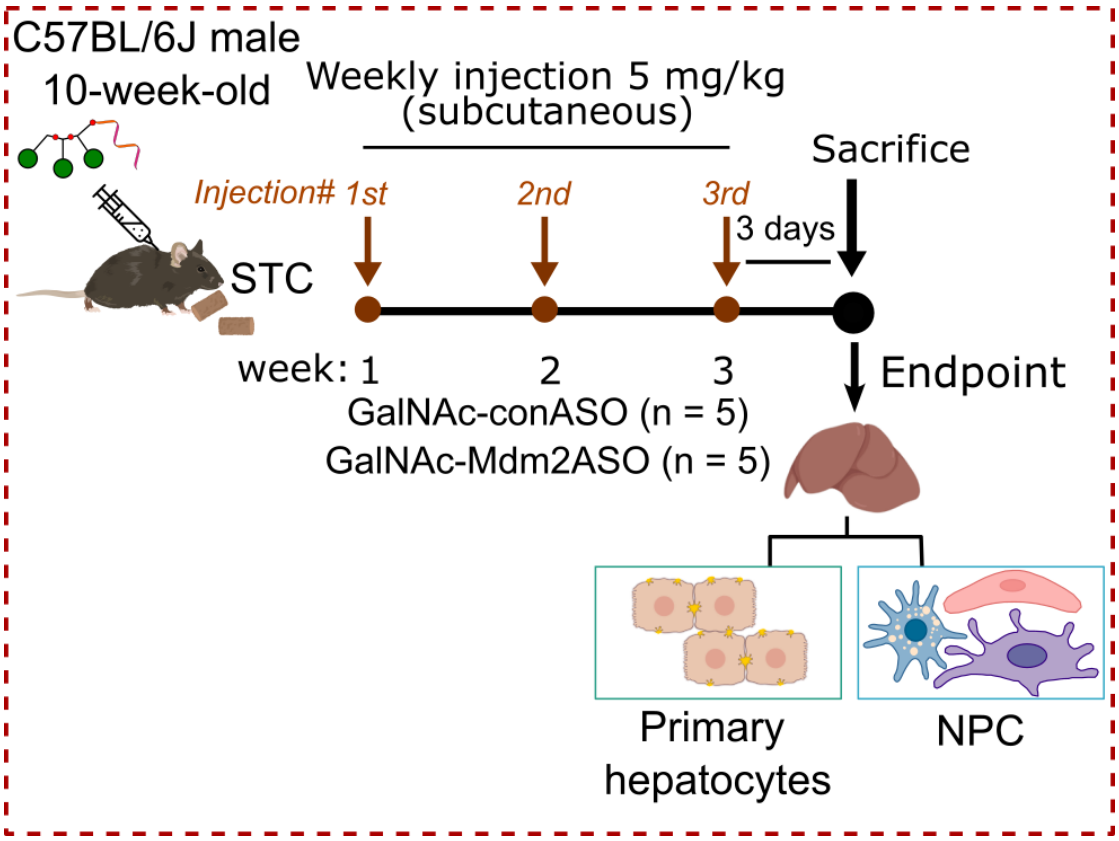

Figure 3.1. Animal experiment 1.

Male C57BL/6J mice fed the STC diet were injected once weekly for 3 weeks with GalNAc-conASO or GalNAc-Mdm2ASO at the indicated doses. Three days after the last injection, the mice were sacrificed, and the liver was perfused to collect the primary hepatocyte and NPC which were analyzed by qPCR and immunoblot. Abbreviations: STC, standard chow; ASO, antisense oligonucleotide; NPC, non parenchymal cells.

To evaluate the hepatocyte specificity of GalNAc-Mdm2ASO, we first analyzed the expression of MDM2 and p53-regulated genes (*p53, p21, p16*) in liver fractions, including primary hepatocytes and non-parenchymal cells (NPCs), as well as in other tissues including the heart, muscle, pancreatic islets, and kidney from mice injected with either GalNAc-conASO or GalNAc-Mdm2ASO. We confirmed that GalNAc-Mdm2ASO significantly reduced both mRNA and protein levels of hepatic MDM2 in primary hepatocytes (Figure 3.2 A, B), with no significant changes observed in the NPC fractions (Figure 3.2 C, D). This hepatocyte-specific knockdown suggests that the GalNAc-Mdm2ASO effectively targets hepatocytes, with minimal effects on other liver cell types. The reduction in *Mdm2* was accompanied by an increase in canonical p53 effectors, *p21* and *p16* mRNA levels, though the *p53* expression remained unchanged (Figure 3.2 A). This increase in the expression of canonical p53 target genes (p21, p16) following GalNAc-Mdm2ASO treatment, despite no change in p53 mRNA, likely reflects MDM2's known role in post-translational regulation of p53 stability. A similar observation was made in the CDAHFD model, where we measured both mRNA and protein level of p53 and demonstrated that the protein levels of p53 increased, despite no change in the mRNA level (Figure 5.2 C).

Additionally, GalNAc-Mdm2ASO did not affect *Mdm2* expression in the heart, muscle, and pancreatic islets, though a modest reduction was observed in the kidney (Figure 3.2 E).

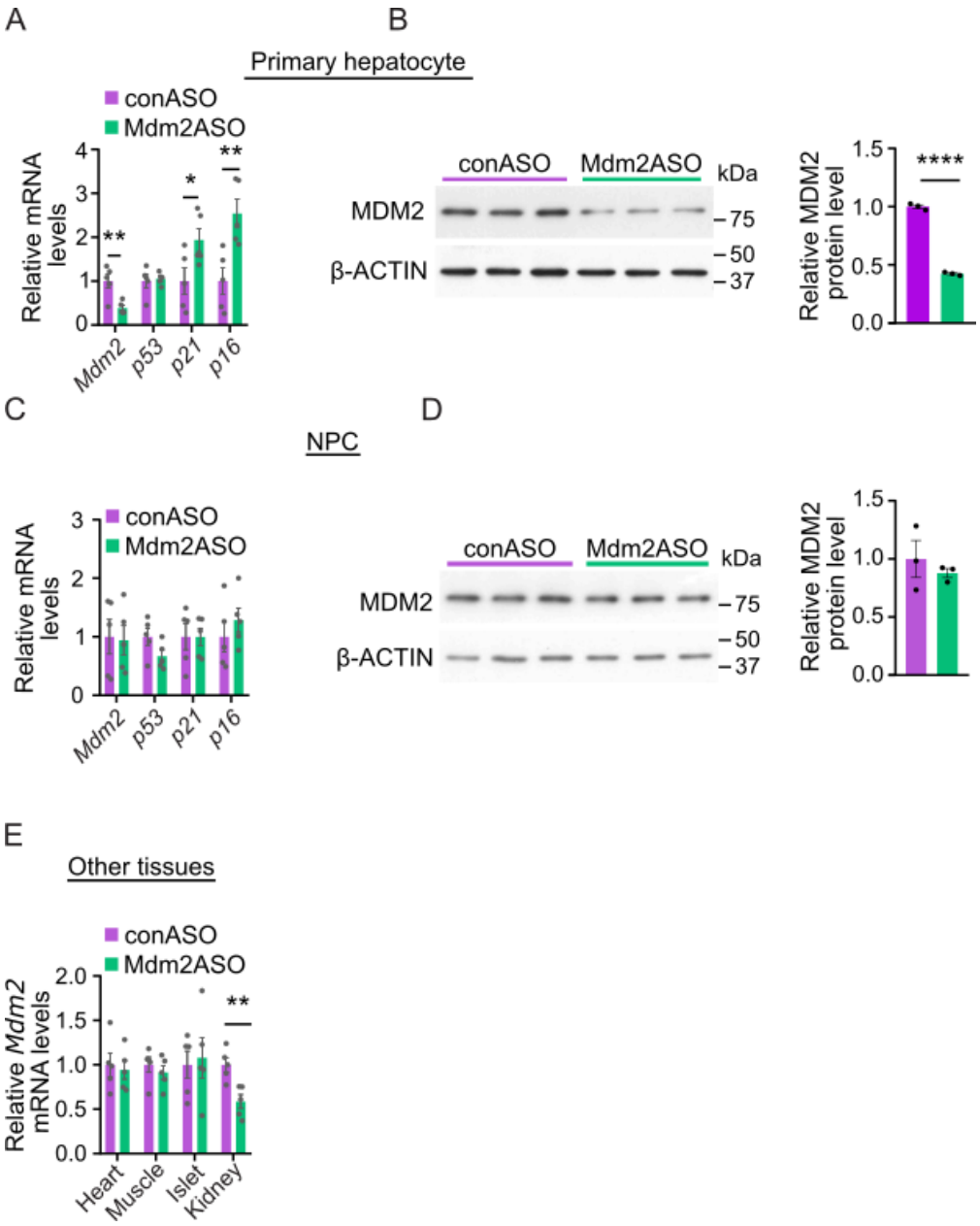

Figure 3.2. GalNAc-ASO mediated selective reduction of MDM2 expression in the primary hepatocyte but not in the NPC or other tissues.

(A-D) mRNA levels of *Mdm2*, *p53*, *p21* and *p16* normalized with *Gapdh* in the primary hepatocytes (n = 5) (A) and NPCs (n = 5) (C). Immunoblotting analysis of MDM2 and β-ACTIN in the primary hepatocyte (B) and NPC (D) fractions. The bar chart is the densiometric analysis of MDM2 normalized with β-ACTIN. Representative immunoblot images are shown (n = 3). (F) mRNA levels of Mdm2 in other tissues (n = 5). Data represent mean ± standard error of mean. *p < 0.05 and **p < 0.01 (Two-tailed independent Student's t-test). Abbreviations: STC, standard chow; HFHC, high fat high cholesterol; ASO, antisense oligonucleotide; NPC, non parenchymal cells.

3.3 Conclusion

In this chapter, I have emphasized the development of GalNAc-Mdm2ASO and its promising therapeutic potential for selectively targeting hepatic MDM2 while minimizing effects on other metabolic organs.

Through a comprehensive screening process, we identified effective MDM2 antisense oligonucleotides, particularly ASO#04, which demonstrated significant silencing of Mdm2 mRNA levels in the liver without adverse effects on liver and kidney function. The modifications that enhance the oligonucleotide's stability and specificity facilitated targeted delivery to hepatocytes, resulting in the upregulation of critical p53-regulated genes. These findings underscore the importance of tailored ASO designs in advancing liver-targeted therapies, providing a strategic approach to mitigate liver pathologies while minimizing off-target effects.

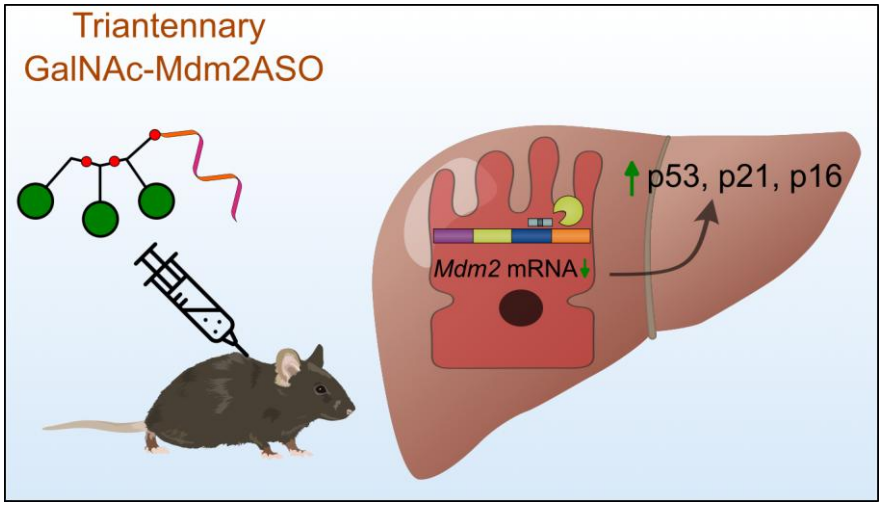

Figure 3.3. GalNAc-ASO mediated selective reduction of MDM2 in the hepatocytes upregulates p53 and its downstream regulated genes.

Chapter 4: GalNAc-Mdm2ASO alleviates hepatic steatosis and fibrosis and improves obesity-related insulin resistance and hyperlipidemia in a HFHC-induced MASLD model

4.1 Introduction

High-fat diets (HFDs) often lead to obesity and insulin resistance, but the onset of metabolic-associated steatotic liver disease (MASLD) in lab animals typically requires prolonged feeding and is less severe than in humans [69, 70]. For instance, mice on a HFD (60% fat) developed steatosis in 10 weeks, mild inflammation after 34 weeks, and slight fibrosis after 50 weeks [71]. Rats showed steatosis and mild inflammation after 4 weeks on a HFD (58% fat) and fibrosis after 24 weeks [72]. While these models highlight key fibrogenic mechanisms, they reflect only the early stages of MASLD, suggesting that additional nutritional factors are necessary for disease progression, especially fibrosis.

Cholesterol may drive the transition from steatosis to MASLD, potentially acting with lipids to cause cellular damage and increased reactive oxygen species [73], leading to inflammation and fibrogenesis [74, 75]. Higher cholesterol levels correlate with hepatic fibrosis, and a rise in intracellular free cholesterol often precedes fibrosis [76]. In line with the dietary characteristics associated with human MASLD/MASH, experimental diets high in cholesterol have been shown to exacerbate disease severity, resulting in severe steatosis, inflammation, and mild fibrosis in mice fed a high-fat (33% fat) and high-cholesterol (1%) diet for 30 weeks [77]. Overall, high-cholesterol diets can significantly induce advanced fibrosis.

4.2 Result

4.2.1 HFHC diet-induced MASLD mouse model

To explore the therapeutic effect of GalNAc-Mdm2ASO on the progression of MASLD, male mice were fed a HFHC diet for 8 weeks before receiving subcutaneous injection of either GalNAc-conASO or GalNAc-Mdm2ASO at a dose of 5 mg/kg. For comparison, two control groups were maintained on a STC diet and received the same ASO treatments. 24-weeks after ASO treatment, the mice were sacrificed, and the liver and plasma were collected for histopathology, biochemical assay and mRNA/protein expression (Figure 4.1).

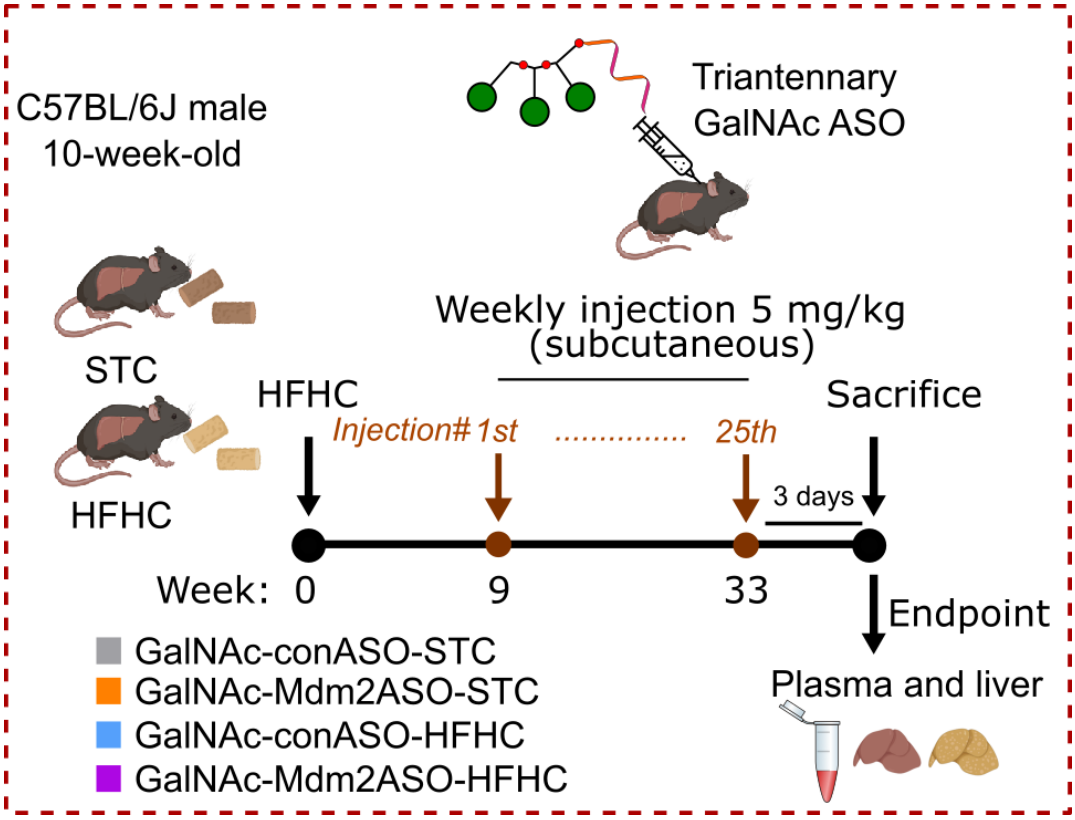

Figure 4.1. Animal experiment 2.

Male C57BL/6J mice were fed the STC or HFHC diet for 8-weeks followed by injections of either GalNAc-conASO or GalNAc-Mdm2ASO for additional 25-weeks. Three days after the last injection the mice were sacrificed, and the liver and plasma were collected for histopathology, biochemical assay and mRNA/protein expression. Abbreviations: STC, standard chow; HFHC, high fat high cholesterol; ASO, antisense oligonucleotide.

The knockdown of MDM2 in the liver was confirmed by immunostaining and real-time quantitative PCR (qPCR) (Figure 4.2, A-C), accompanied by upregulation of *p53*-regulated genes (*p53, p21, p16*) in the HFHC-fed mice (Figure 4.2 C). The expression of p53 protein and the canonical p53 effector, p21 was also elevated in the GalNAc-Mdm2ASO-treated mice compared to the control group (Figure 4.2, D), indicating post-translational stabilization due to MDM2 silencing.

Notably, although GalNAc-Mdm2ASO also reduced MDM2 expression in the kidney, kidney functions, as measured by the circulating levels of urea and creatinine, remained unaffected (**Error! R eference source not found.**). Liver weight, liver-to-body weight ratio, serum markers of liver injury (alanine aminotransferase; ALT) and systemic inflammatory marker (monocyte chemoattractant protein1; MCP1) were comparable between the GalNAc-conASO and GalNAc-Mdm2ASO groups fed the STC diet. However, these measurements were significantly reduced in the GalNAc-Mdm2ASO group fed the HFHC diet, indicating the protective effect of GalNAc-ASO-based hepatic MDM2 reduction against steatosis and liver injury (Figure 4.2, D-G).

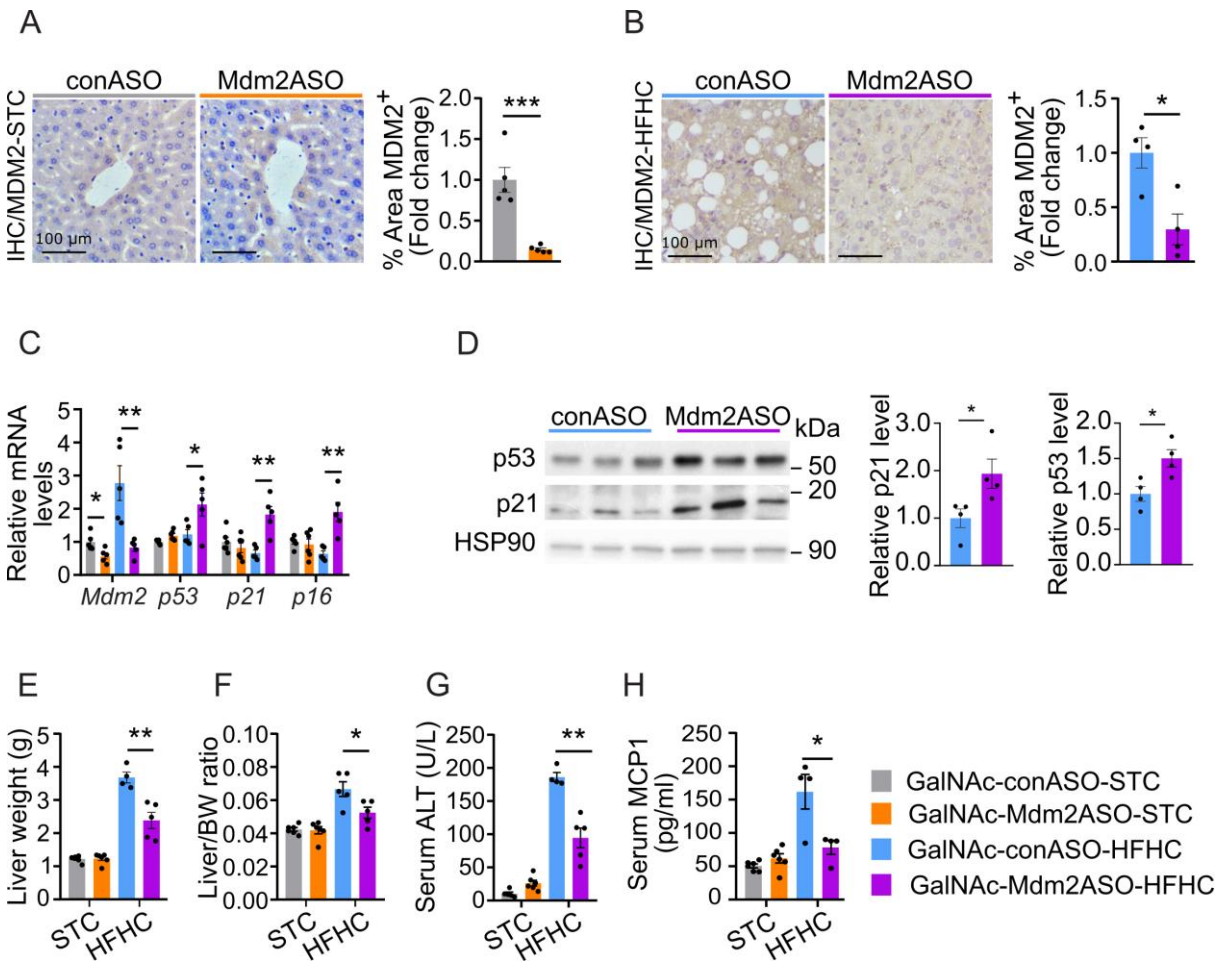

Figure 4.2. GalNAc-Mdm2ASO mediated reduction of MDM2 and improved liver injury.

(A-B) Liver sections of STC (A) and HFHC (B) groups were subjected to immunohistochemical (IHC) staining of MDM2. The bar charts in the right panel are quantification % of MDM2+ area. (C) mRNA levels of *Mdm2, p53, p21* and *p16* normalized with *Gapdh* in livers (n = 6 STC, n = 5 HFHC). (D) Immunoblotting analysis of p53 and p21 in the liver. The bar chart is the densiometric analysis normalized with HSP90. Representative immunoblot images are shown (n = 3). (E-F) Liver weight (E), liver to body weight ratio (F). (G) Serum ALT. (H) Serum MCP1. Data represent mean ± standard error of mean. *$p < 0.05$ and **$p < 0.01$ (Two-tailed independent Student's t-test). Abbreviations: STC, standard chow; HFHC, high fat high cholesterol; ALT, alanine aminotransferase; MCP1, monocyte chemoattractant protein 1.

Table 4.1. Effect of GalNAc-Mdm2ASO on body/tissue weight and serum levels in mice on a HFHC diet.

	conASO	Mdm2ASO	*P* value	Measurement time
Body weight (g)	51.83 ± 1.39	44.74 ± 2.09	0.03 (*)	Endpoint
Liver weight (g)	3.68 ± 0.16	2.38 ± 0.24	0.004 (**)	Endpoint
sWAT weight (g)	3.03 ± 0.22	2.28 ± 0.21	0.04 (*)	Endpoint
eWAT weight (g)	3.15 ± 0.29	3.32 ± 0.13	0.60	Endpoint
BAT weight (g)	0.24 ± 0.02	0.22 ± 0.03	0.65	Endpoint
ALT (U/L)	187 ± 6.94	95.24 ± 15.08	0.001 (**)	Endpoint
AST (U/L)	141.49 ± 7.92	121.85 ± 13.04	0.268	Endpoint
serum MCP1 (pg/mL)	161.87 ± 26.03	78.22 ± 10.43	0.025 (*)	Endpoint
serum Adiponectin (μg/mL)	43.56 ± 5.68	29.65 ± 3.13	0.087	Endpoint
serum creatinine (μM)	32.83 ± 3.97	27.51 ± 2.35	0.282	Endpoint
serum urea (mg/dL)	51.56 ± 2.38	57.22 ± 2.39	0.144	Endpoint

Ten-week-old male C57BL/6J mice were fed the HFHC diet for 8-weeks followed by injections of either GalNAc-conASO or GalNAc-Mdm2ASO at a dose of 5 mg/kg for an additional 25-weeks. Three days after the final injection, the mice were sacrificed, and tissues and plasma were collected for biochemical assays. Data represent mean ± standard error of mean. *p (Two-tailed independent Student's t-test). Abbreviations: sWAT, subcutaneous white adipose tissue; eWAT, epididymal white adipose tissue; BAT, brown adipose tissue; ALT, alanine aminotransferase; AST, aspartate transaminase; MCP1, monocyte chemoattractant protein 1.

4.2.2 Hepatic Mdm2 silencing by GalNAc-Mdm2ASO alleviated HFHC diet-induced steatosis and fibrosis

Chronic overnutrition is known to promote ectopic lipid storage and meta-inflammation in the liver [78]. Consistent with this, histological analysis of H&E-stained liver sections showed pronounced steatosis in the GalNAC-conASO, while the density and size of lipid droplets were notably reduced in mice treated with GalNAC-Mdm2ASO, with no differences observed under the STC diet (Figure 4.3 A).

Histological assessments were performed using the scoring system developed by the NASH Clinical Research Network [79]. Treatment with GalNAc-Mdm2ASO led to a reduction in HFHC-induced hepatic steatosis, lobular inflammation (characterized by immune cell infiltration), ballooning (a structural change indicative of hepatic injury in steatohepatitis), and the overall NASH activity score (NAS) (Figure 4.3 B). Furthermore, there was a decrease in hepatic lipid content, as indicated by Oil Red O staining (Figure 4.3 C) and biochemical assay measuring hepatic triglyceride (TG) (Figure 4.3 D).

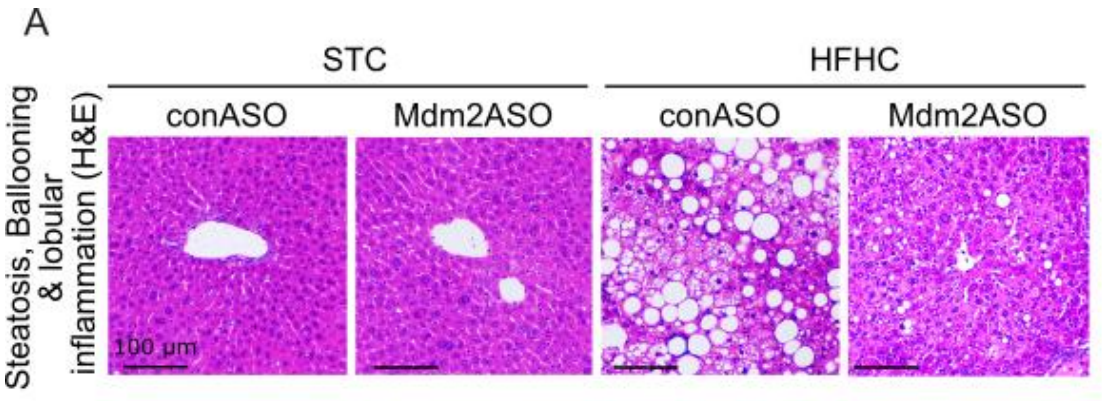

B

Histological scores of liver sections (HFHC)

	conASO	Mdm2ASO	P-value
Steatosis	44.35 ± 1.76	19.08 ± 5.73	0.017 (**)
Inflammation	2.86 ± 0.11	0.95 ± 0.23	0.001 (**)
Ballooning	9.53 ± 1.18	2.73 ± 0.60	0.005 (**)
NAS	5.00 ± 0.00	2.25 ± 0.25	0.001 (**)

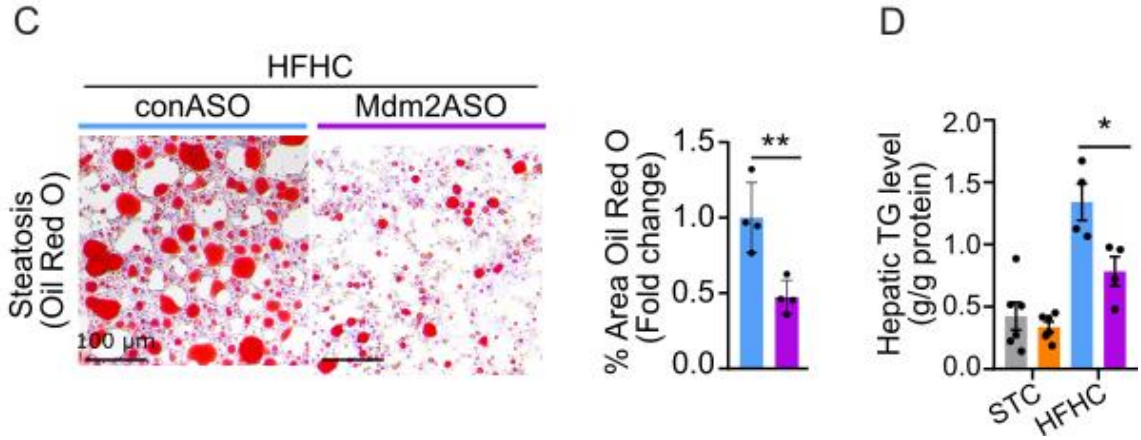

Figure 4.3. GalNAc-Mdm2ASO mediated reduction of hepatic steatosis.

(A-B) H&E staining of liver sections (A). Quantitative analysis of the grades of steatosis, inflammation, and the total NASH activity score (NAS) for the H&E staining (B). (C) Oil Red O (ORO) staining of liver sections. The right panel is quantification % of ORO+ area. (D) Hepatic TG (n =6 STC, n = 4-5 HFHC). Data represent mean ± standard error of mean. *$p < 0.05$ and **$p < 0.01$ (Two-tailed independent Student's t-test). Abbreviations: STC, standard chow; HFHC, high fat high cholesterol.

While MASLD encompasses a spectrum of liver disorders ranging from simple steatosis to more severe conditions, the progression to fibrosis represents a critical turning point in disease severity. Therefore, we investigated whether GalNAc-Mdm2ASO could mitigate liver fibrosis. Hepatic stellate cells (HSCs) are the primary sources of collagen and other extracellular matrix proteins in liver fibrosis [80]. When exposed to oxidative stress, inflammatory cytokines or excessive cholesterol, HSCs become activated and transition to proliferative fibrogenic cells [81]. To assess liver fibrosis, we evaluated hepatic collagen deposition using picrosirius red staining of liver tissues. Collagen levels were significantly reduced in the GalNAc-Mdm2ASO-treated mice compared to the GalNAc-conASO group (Figure 4.4 A). Similarly, immunoblot analysis of alpha-smooth muscle actin (α-SMA), a marker for activated HSCs responsible for liver collagen deposition, also showed decreased levels in the livers of mice treated with GalNAc-Mdm2ASO (Figure 4.4 B). In line with the reduction in collagen deposition, we observed decreased expression of pro-fibrotic genes, including collagen type 1 alpha 1 (*Col1α1*), collagen type 3 alpha 1 (*Col3α1*), and tissue inhibitor of metalloproteinase 1 (*Timp1*), which are part of the collagen protein family (Figure 4.4 C). Additionally, our RNA sequencing data indicate that markers associated with activated HSCs are downregulated, whereas markers for quiescent HSCs are upregulated in the GalNAc-Mdm2ASO-treated mice compared to the controls (Figure 4.5 B). This was accompanied by an increased abundance of the liver resident macrophage, Kupffer cell (KC), which are known to maintain hepatic homeostasis (Figure 4.5 C) [82, 83]. Consistent to the reductions in liver injury, systemic inflammation, and immune cell infiltration (Figure 4.2 F-G, Figure 4.3 J-K), the anti-inflammatory pathways, including the classical IL10 pathway, were upregulated in GalNAc-Mdm2ASO-treated mice (Figure 4.5 D, E).

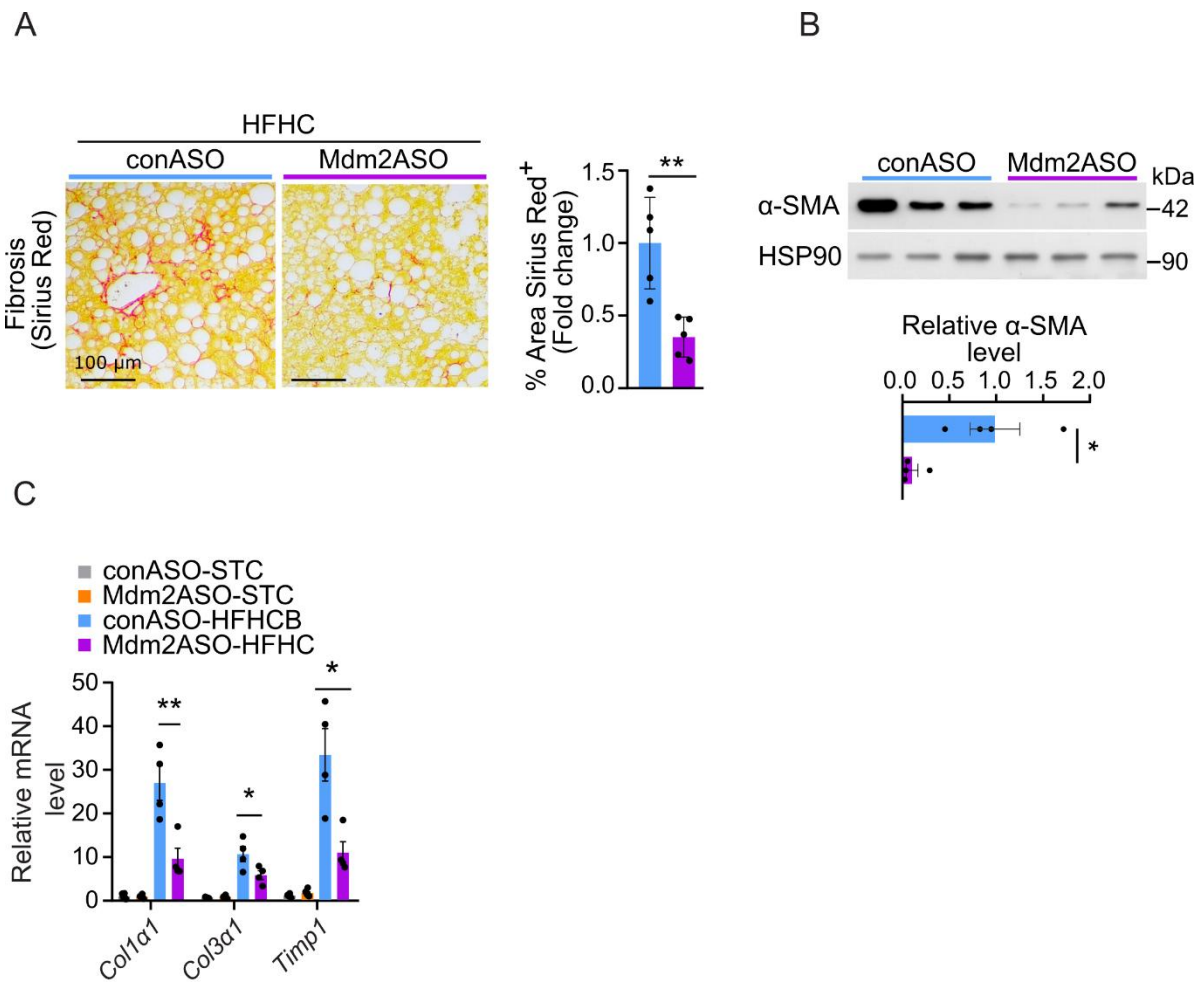

Figure 4.4. GalNAc-Mdm2ASO mediated reduction of hepatic fibrosis.

(A) Sirius red (SR) staining of liver sections. The right panel is quantification % of SR+ area. (B) Immunoblotting analysis of α-SMA and HSP90 in liver lysates. The bottom panel is densiometric analysis of α-SMA normalized with HSP90. Representative immunoblot images are shown (n = 3). (C) mRNA levels of profibrotic genes (*Col1α1, Col3α1, Timp1*) normalized with *Gapdh* in livers (n = 6 STC, n = 5 HFHC). Data represent mean ± standard error of mean. *p < 0.05 and **p < 0.01 (Two-tailed independent Student's t-test). Abbreviations: STC, standard chow; HFHC, high fat high cholesterol.

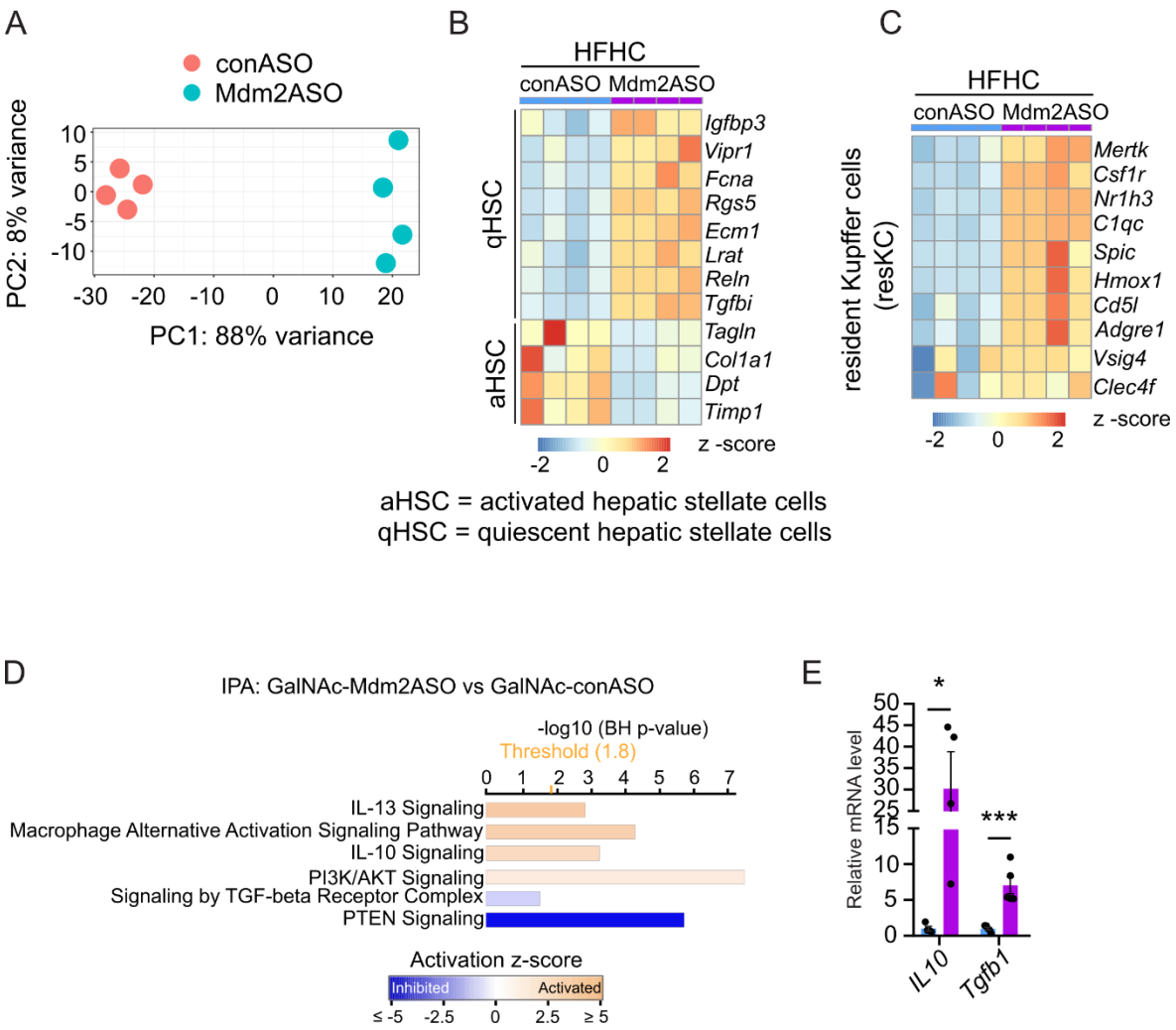

Figure 4.5. RNAseq analysis of livers from the mice fed with HFHC diet.

(A) Principle component analysis (PCA) (n = 4 conASO, n = 4 Mdm2ASO). (B-C) Heatmap showing genes associated with hepatic stellate cells (HSC) (B), liver resident macrophage (C). (D) Ingenuity pathway analysis (IPA) for the anti-inflammatory pathways. (E) mRNA levels of anti-inflammatory genes (*Il10, Tgfb1*) normalized with *Gapdh* in livers (n = 4-5, HFHC). Data represent mean ± standard error of mean. *p < 0.05 and **p < 0.01 (Two-tailed independent Student's t-test). Abbreviations: STC, standard chow; HFHC, high fat high cholesterol.

4.2.3 GalNAc-Mdm2ASO treatment improved insulin sensitivity in MASLD

Insulin signaling is crucial for regulating glucose and lipid metabolism, promoting glucose uptake and fat storage while inhibiting gluconeogenesis and lipolysis. Disruptions in this signaling pathway leads to insulin resistance and fatty liver disease. Ectopic fat deposition, especially in the liver, is a hallmark of insulin resistance, leading to lipotoxicity, inflammation, disrupted insulin signaling, excessive hepatic glucose production, and mitochondrial dysfunction [84]. Reducing ectopic fat can improve insulin sensitivity [85].

To investigate whether GalNAc-Mdm2ASO also improves insulin sensitivity in the HFHC model, we measured glucose and lipid profiles over time (Figure 4.6 A). Weekly body weight and food intake were not significantly different among mice in the two groups (Figure 4.6 C, D). However, insulin and tolerance tests (ITT and GTT) after 18 and 20 weeks of HFHC feeding showed that GalNAc-Mdm2ASO-treated mice had better insulin sensitivity (Figure 4.7 A) and glucose tolerance (Figure 4.7 B). We further assessed hepatic insulin sensitivity using a pyruvate tolerance test (PTT), a reliable measure of hepatic gluconeogenesis [86, 87]. Following the administration of pyruvate, a precursor for gluconeogenesis, the mice treated with GalNAc-Mdm2ASO showed lower glucose excursions (Figure 4.7 C), suggesting an improved hepatic insulin sensitivity. This improved insulin sensitivity may be associated with decreased ectopic liver fat and/or subcutaneous white adipose tissue (sWAT) mass [88], ultimately enhancing insulin response.

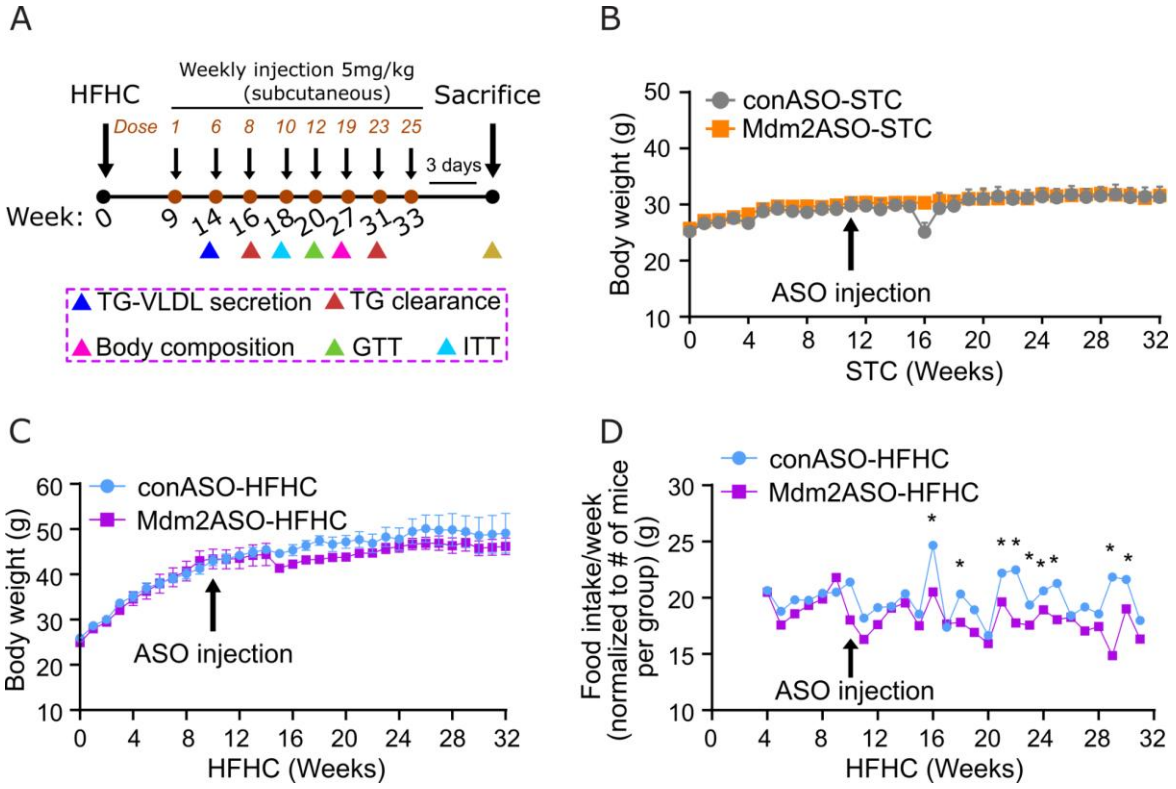

Figure 4.6. Effect of GalNAc-Mdm2ASO on glucose and lipid profiles.

(A) Experimental timeline. (B-D) Body weight changes (B, C) and Food intake (D) over time (n = 6). Data represent mean ± standard error of mean. *p < 0.05 and **p < 0.01 (Two-tailed independent Student's t-test).

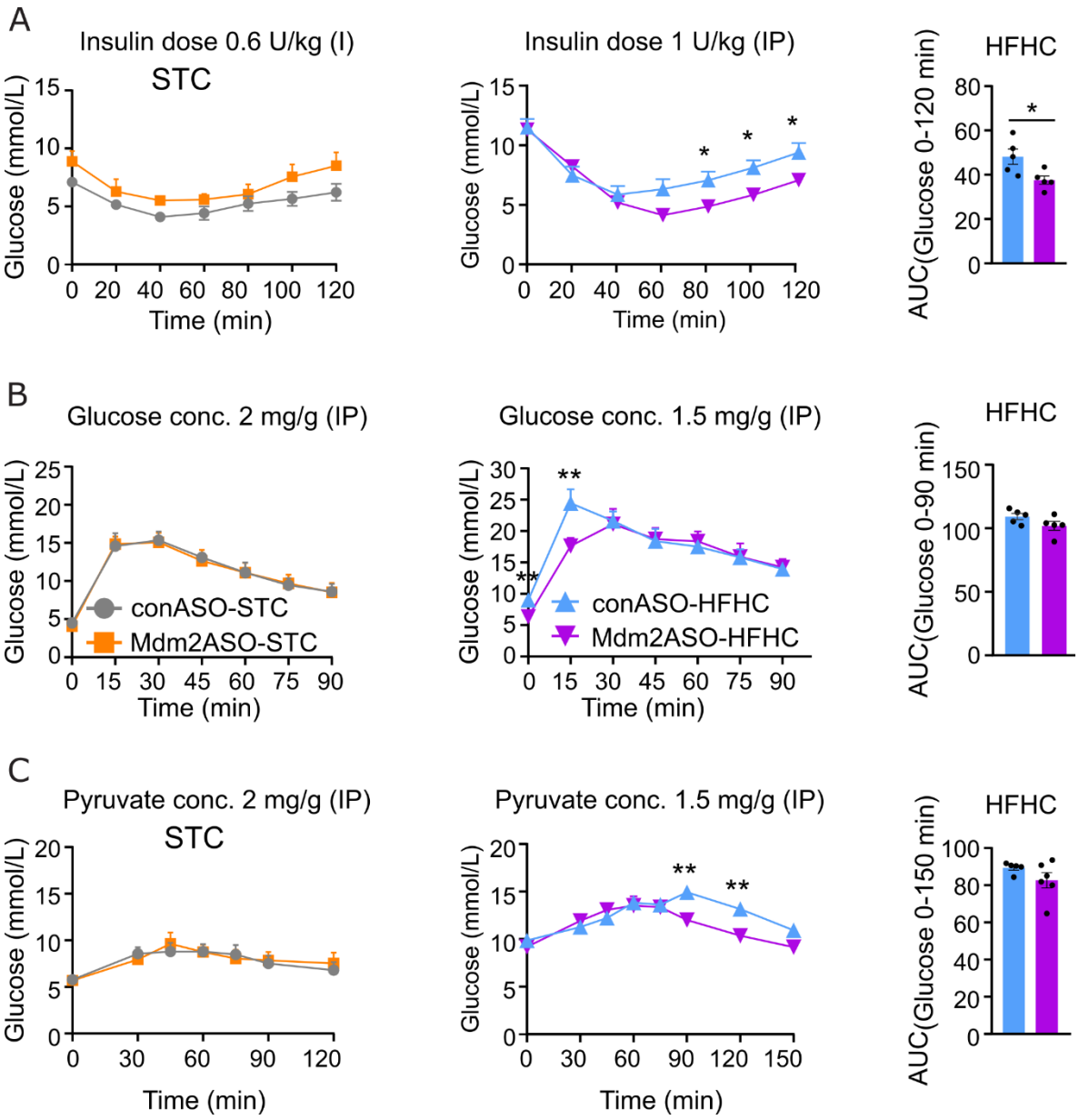

Figure 4.7. GalNAc-Mdm2ASO treatment improves insulin sensitivity.

(A) ITT. Blood glucose levels after an IP injection of insulin in the 6 hr fasted mice (n = 6 STC, n= 6 HFHC). Right panel is the calculation of AUC of ITT of the HFHC group. (B) GTT. Blood glucose levels after an IP injection of glucose in the 16 hr fasted mice (n = 6 STC, n = 6 HFHC). Right panel is the calculation of area under the curve (AUC) of GTT of the HFHC group. (C) PTT. Blood glucose level after an IP injection of sodium pyruvate in the 16 hr fasted mice (n = 6 STC, n = 6 HFHC). Right panel is the calculation of AUC of PTT of HFHC group. Data represent mean ± standard error of mean. *p < 0.05 and **p < 0.01 (Two-tailed independent Student's t-test). Abbreviations: STC, standard chow; HFHC, high fat high cholesterol; ITT, insulin tolerance test; GTT, glucose tolerance test; PTT, pyruvate tolerance test; IP, intraperitoneal.

4.2.4 Effect of GalNAc-Mdm2ASO treatment on hepatic lipid metabolism

Our previous study demonstrated that the inactivation of hepatic MDM2 enhances TG-VLDL secretion through the upregulation of ApoB expression [25]. Therefore, we explored the effects of GalNAc-Mdm2ASO on TG metabolism. We focused on mice fed HFHC diet, as GalNAc-Mdm2ASO treatment only improved hepatic TG accumulation under this dietary condition.

To evaluate hepatic TG-VLDL secretion, we measured serum TG levels following the administration of tyloxapol, a lipase (LPL) inhibitor that prevents the peripheral TG-VLDL catabolism and clearance [89, 90]. Contrary to our previous findings [25], GalNAc-Mdm2ASO treatment resulted in significant lower serum levels of TG after tyloxapol injection (Figure 4.8 A). Interestingly, GalNAc-Mdm2ASO treatment also increased circulating and hepatic levels of ApoB after fasting for 4 hours (Figure 4.8 B, C), consistent to our earlier study [25]. Lipid tolerance test indicated that GalNAc-Mdm2ASO treatment dramatically promoted TG clearance (Figure 4.8 D). It is noteworthy that previous research suggests a potential delay in LPL inhibition induced by tyloxapol at the early time points [91]. The observed lower TG levels during the TG-VLDL assay might be attributed to the increased TG clearance shortly after tyloxapol injection, yet further investigation is warranted to test this speculation. Apart from TG levels, GalNAc-Mdm2ASO treatment reduced circulating level of free fatty acid (FFAs) under feeding and fasting conditions (**Error! Reference s ource not found.**), accompanied by lower expression of hepatic genes involved in FFA uptake, oxidation, and lipogenesis (Figure 4.9). Taken together, GalNAc-Mdm2ASO treatment alters hepatic lipid metabolism under obese conditions.

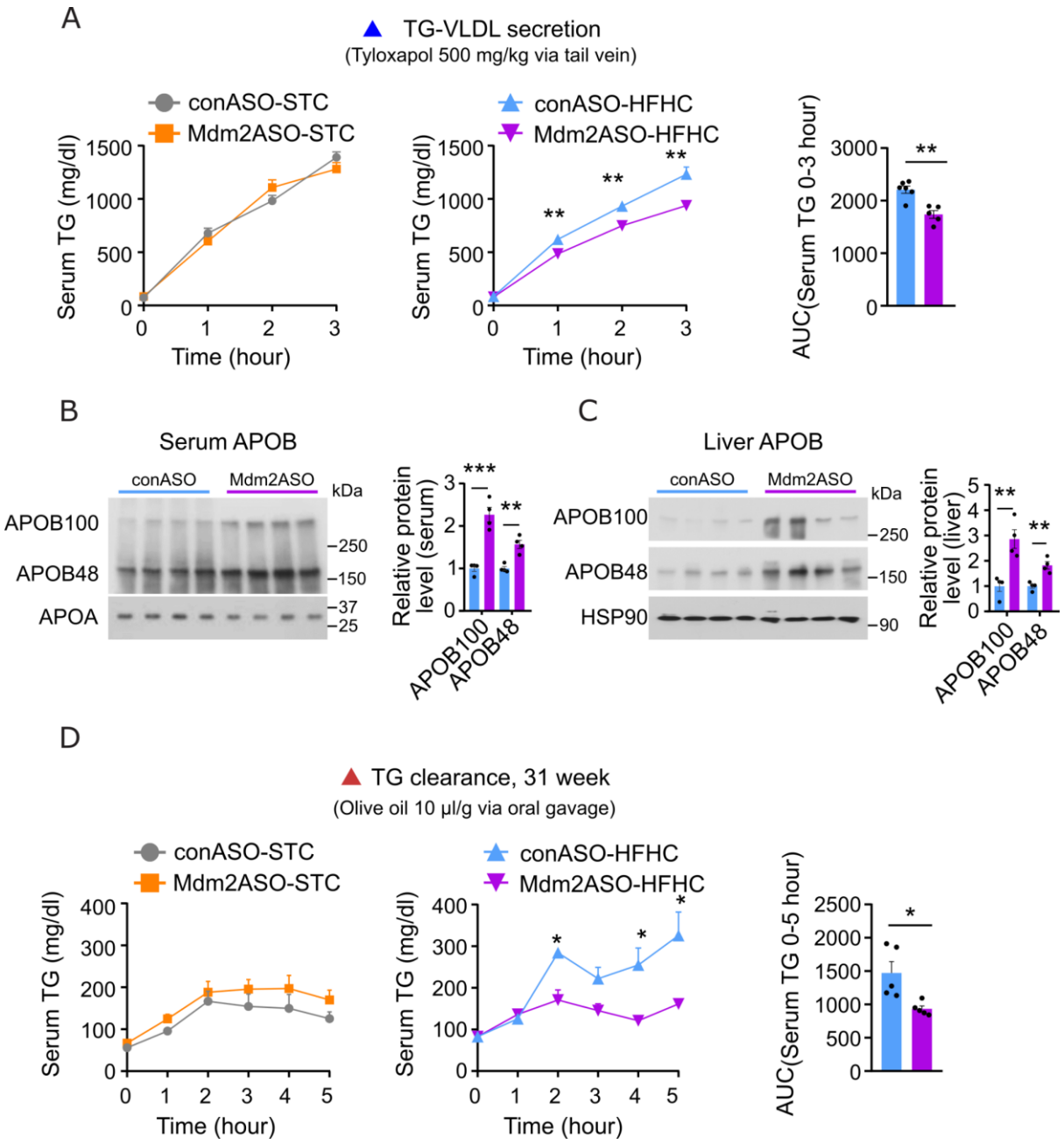

Figure 4.8. GalNAc-Mdm2ASO treatment improves circulating TG clearance.

(A) TG-VLDL secretion assay. Serum TG levels after tyloxapol injection in the 16 hr fasted mice (n = 6 STC, n = 6 HFHC). Right panel is the calculation of AUC of serum TG of HFHC group. (B-C) Immunoblot analysis of serum (B) and liver (C) APOB. Right panel is the densiometric analysis normalized with internal control (APOA for serum and HSP90 for liver lysate). Representative immunoblot images are shown (n = 4). (D) TG clearance test. Serum TG levels after oral gavage with olive oil in the 16 hr fasted mice fed a HFHC for 31 week (n = 5 HFHC). Right panel is the calculation of AUC of serum TG of HFHC group. Data represent mean ± standard error of mean. *p < 0.05 and **p < 0.01 (Two-tailed independent Student's t-test). Abbreviations: STC, standard chow; HFHC, high fat high cholesterol; TG, triglyceride; VLDL, very low density lipoprotein.

Table 4.2. Effect of GalNAc-Mdm2ASO on serum glucose and lipid profiles in mice on a HFHC diet.

	conASO	Mdm2ASO	*P* value	Measurement time
Fasting glucose (mmol/L), 6h	8.85 ± 0.53	8.50 ± 0.56	0.618	23 week, dose 15
Fasting insulin (ng/mL), 6h	0.85 ± 0.23	0.71 ± 0.19	0.591	23 week, dose 15
Fasting glucose (mmol/L), 16h	9.20 ± 0.77	8.48 ± 0.43	0.438	23 week, dose 15
Fasting insulin (ng/mL), 16h	0.50 ± 0.11	0.61 ± 0.17	0.528	23 week, dose 15
serum TG (mg/dL)	58.20 ± 6.50	57.76 ± 9.97	0.970	Endpoint
serum TC (mg/dL)	256.36 ± 17.80	66.37 ± 3.10	< 0.001 (**)	Endpoint
serum LDL (mg/dL)	106.52 ± 16.04	21.44 ± 1.77	0.008	Endpoint
serum HDL (mg/dL)	48.52 ± 6.57	13.92 ± 1.40	< 0.001 (**)	Endpoint
serum FFA (mg/dL); Fed	18.39 ± 0.97	13.59 ± 1.89	0.019 (**)	26 week, dose 18
serum FFA (mg/dL); Fast (16h)	26.65 ± 1.19	21.65 ± 1.60	0.039 (*)	26 week, dose 18
serum FFA (mg/dL); Re-fed	33.31 ± 0.84	29.31 ± 2.75	0.227	26 week, dose 18

Ten-week-old male C57BL/6J mice were fed the HFHC diet for 8-weeks followed by injections of either GalNAc-conASO or GalNAc-Mdm2ASO at a dose of 5 mg/kg for an additional 25-weeks. Three days after the final injection, the mice were sacrificed, and tissues and plasma were collected for biochemical assays. Data represent mean ± standard error of mean. *p (Two-tailed independent Student's t-test). Abbreviations: TG, triglyceride; TC, total cholesterol; LDL, low-density lipoprotein; HDL, high-density lipoprotein; FFA, free fatty acid.

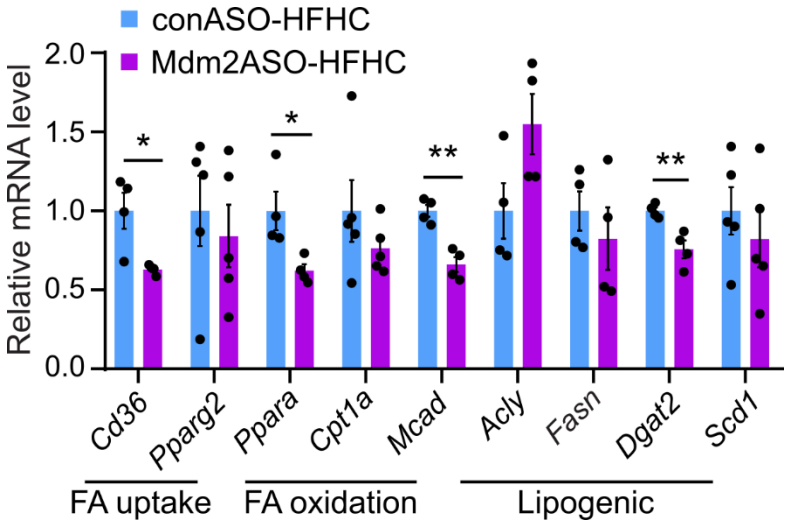

Figure 4.9. GalNAc-Mdm2ASO mediated reduction of FA uptake, FA oxidation and lipogenic genes.

mRNA levels of FA uptake (*Cd36, Pparg2*), FA oxidation (*Ppara, Cpt1a, Mcad*), and lipogenesis (*Acly, Fasn, Dgat2, Scd1*) normalized with *Gapdh* in livers (n = 5 HFHC). Data represent mean ± standard error of mean. *$p < 0.05$ and **$p < 0.01$ (Two-tailed independent Student's t-test). Abbreviations: HFHC, high fat high cholesterol.

4.2.5 GalNAc-Mdm2ASO treatment protects against hepatic cholesterol accumulation

Given that GalNAc-Mdm2ASO demonstrated a significant impact on hepatic TG, we also measured hepatic total cholesterol (TC), another key factor contributing to hepatic lipid dysmetabolism and advanced steatohepatitis [92]. No significant difference was observed between the two groups under STC feeding (Figure 4.10 A). In contrast, GalNAc-Mdm2ASO treatment almost completely prevented HFHC diet-induced hepatic cholesterol accumulation and circulating TC levels compared to those received GalNAc-conASO treatment (Figure 4.10 A-B). The reduction of TC was due to decrease in LDL-C and HDL-C (Figure 4.10 C-D). To confirm this further, we fractionated circulating lipoproteins into VLDL, LDL, and HDL using high-performance liquid chromatography (HPLC). This analysis revealed a significant reduction in cholesterol levels in VLDL and LDL and modest reduction in HDL of the mice treated GalNAc-Mdm2ASO under HFHC feeding condition (Figure 4.10 E).

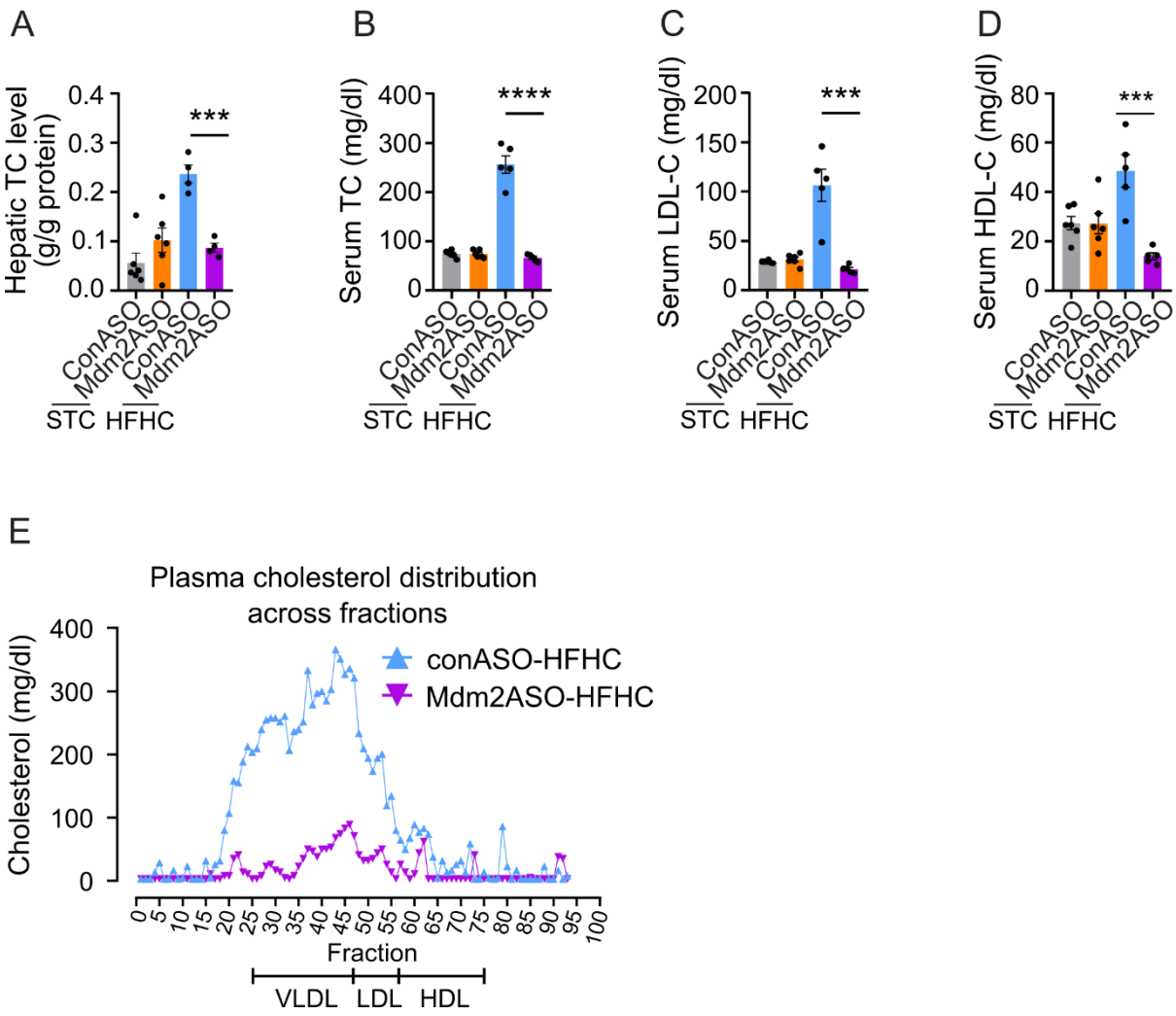

Figure 4.10. GalNAc-Mdm2ASO mitigates HFHC diet-induced cholesterol accumulation in liver and systemic circulation.

(A-B) Endpoint hepatic TC (A), serum TC (B) (n = 6 STC, n= 4 HFHC). (C-D) Serum LDL-C (C), serum HDL-C (D) (n = 6 STC, n = 5 HFHC). (E) Serum cholesterol in different density of lipoproteins in the mice fed with HFHC (n= 6). Data represent mean ± standard error of mean. *p < 0.05 and **p < 0.01 (Two-tailed independent Student's t-test). Abbreviations: TC, total cholesterol; LDL-C, low density lipoprotein-cholesterol; HDL-C, high density lipoprotein-cholesterol; VLDL, very low density lipoprotein.

Given the dramatic impact of GalNAc-Mdm2ASO on TG and cholesterol metabolism, we performed a targeted lipidomic analysis of liver samples from the HFHC diet groups. Orthogonal partial least squares discriminant analysis (OPLS-DA) demonstrated tight clustering of lipidomes within each group and revealed significant differences between the two groups (Figure 4.11 A). Lipidomics analysis revealed notable reductions in both hepatic TG and cholesteryl esters (CE) in GalNAc-Mdm2ASO-treated mice (Figure 4.11 B-C). The reduction was observed across numerous CE species (Figure 4.11 D). While levels of sphingomyelin (SM), fatty acids (FA), and lysophosphatidylethanolamine (LPE) were increased, the lipotoxic lipid species such as diacylglycerides (DG) and ceramides (Cer) were significantly decreased (Figure 4.11 B, C). DG and Cer are recognized as harmful lipids linking to MASLD development through oxidative stress, inflammation and insulin resistance [93].

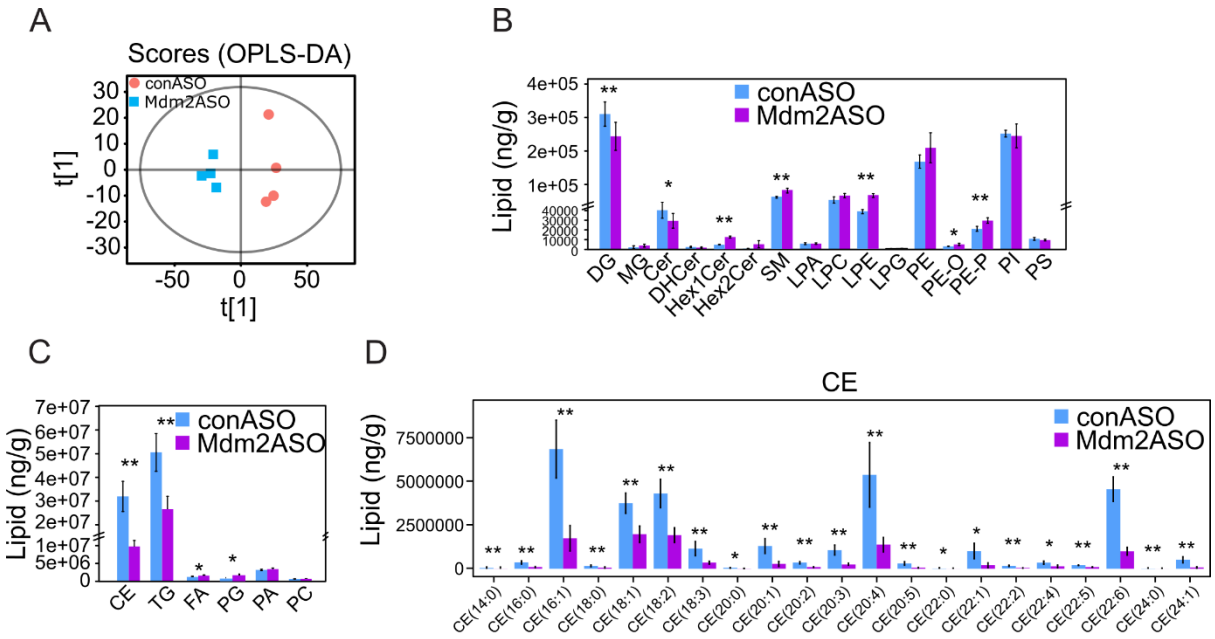

Figure 4.11. Lipidomic analysis of livers from the mice fed with HFHC diet.

(A) OPLS-DA scores (n = 4 conASO, n = 4 Mdm2ASO). (B-C) Differential abundance of all lipid class. (D) CE lipid species. Data represent mean ± standard error of mean. *p < 0.05 and **p < 0.01 (Two-tailed independent Student's t-test).

Abbreviations: DG, diacylglycerol; MG, monoacylglycerol; Cer, ceramide; DHCer, dihydroceramide; HexCer, hexosylceramide; SM, sphingomyelin; LPA, lysophosphatic acid; LPC,lysophosphatidylcholine; LPE, lysophosphatidylethanolamine; LPG, lysophosphatidylglycerol; PE, phosphatidylethanolamine; PI, phosphatidylinositol; PS, phosphatidylserine; TC, total cholesterol; CE, cholesteryl esters; TG, triacylglyceride; PC, phosphatidylcholine; PA, phosphatic acid; FA, fatty acid.

Next, we explored whether hepatic MDM2 expression is associated with circulating DG and Cer levels in humans using Mendelian randomization (MR) analysis [94]. This analysis leverages genetic variants as instrumental variables using GWAS summary statistics from the study by *Cadby* et al. [65], which included 6,057 European participants. The MR analysis revealed significantly positive associations between hepatic MDM2 and both DG [IVW estimate (β) = 0.100, 95% CI: 0.085-0.114, $P = 1.95 \times 10^{-40}$] and ceramide [IVW estimate (β) = 0.033-95% CI: 0.019, 0.048, $P = 8.02 \times 10^{-6}$] (Figure 4.12 A-C).

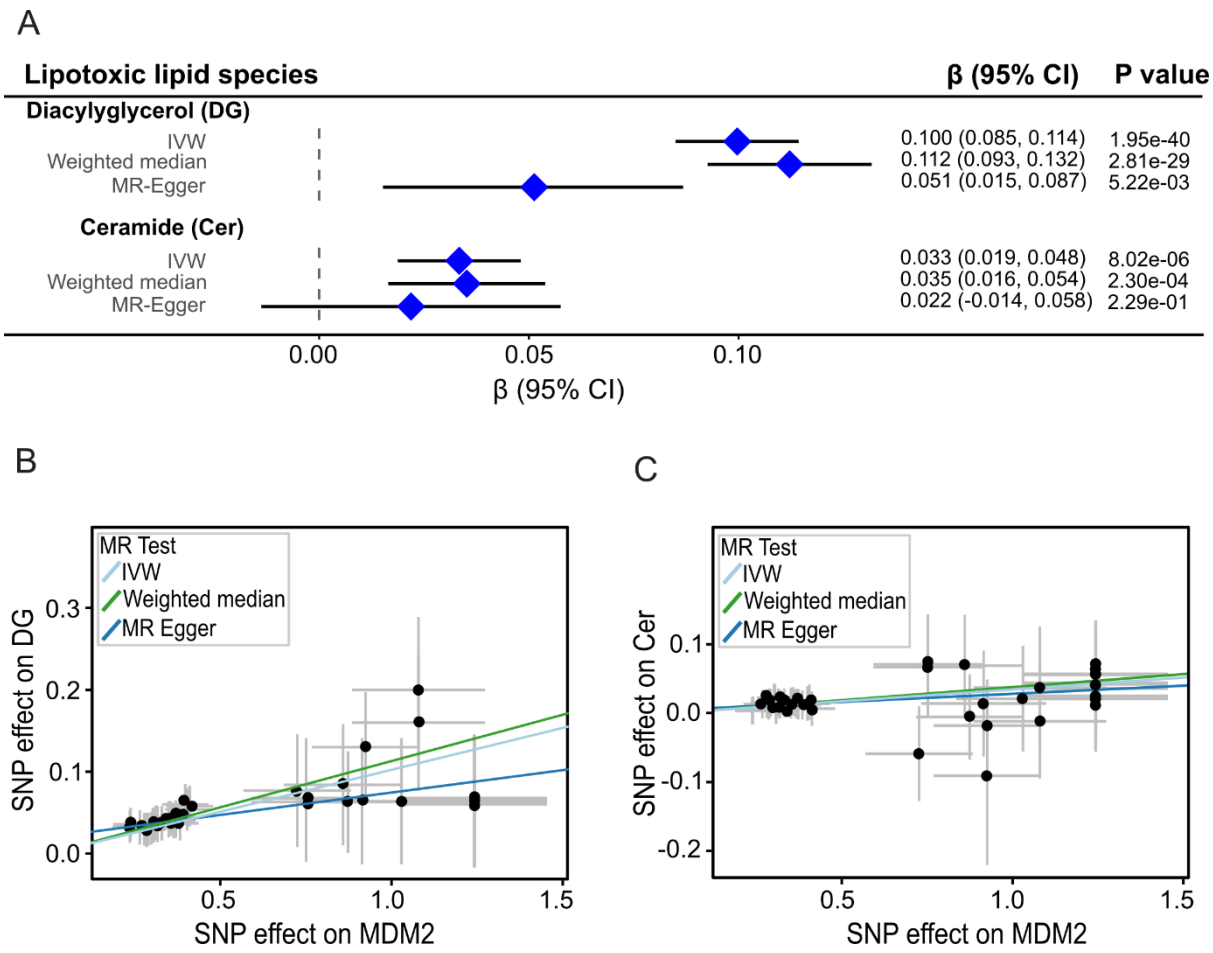

Figure 4.12. Causal associations between MDM2 genetic variants and the lipotoxic lipid species using two-sample Mendelian Randomization (MR) analysis.

(A) Forest plot showing the association between MDM2 genetic variants and lipotoxic lipid species such as Diacylglycerol (DG) and Ceramide (Cer). Each horizontal line represents the estimated effect size (beta coefficient) with 95% confidence intervals. The vertical line indicates the null effect (β = 0). (B-C) Scatter plot of single nucleotide polymorphism (SNP) potential effects between MDM2 and DG (B), MDM2 and Cer (C).

Taken together, these findings collectively support the protective effect of GalNAc-Mdm2ASO treatment against hepatic cholesterol accumulation and hyperlipidemia in MASLD.

4.2.6 GalNAc-Mdm2ASO treatment facilitates excess cholesterol elimination from the body through biliary secretion and bile conversion

Hepatic cholesterol is maintained by the dietary intake, *de novo* cholesterol biosynthesis and excretion to the bile. GalNAc-Mdm2ASO treatment did not alter food intake under the HFHC diet feeding condition (Figure 4.6 D). QPCR analysis revealed that GalNAc-Mdm2ASO treatment exerted inconsistent effect on the *de novo* cholesterol biosynthetic genes (increase of *Hmgcr, Sqle, and Srebp2* but no change in *Hmgcs, Lxra, and Acat2*) (Figure 4.13 B). We speculated that the increase of the cholesterol biosynthetic genes might be the compensatory response for a reduction of hepatic and circulating TC in GalNAc-Mdm2ASO-treated mice. Next, we investigated whether cholesterol reduction was due to cholesterol excretion from the body through biliary secretion. Bile acids (BAs) represent the primary pathway for body's cholesterol clearance (Figure 4.13 A). Increase of cholesterol and bile acid efflux have been shown to reduce the accumulation of lipids such as cholesterol, free fatty acids (FFA), and TG in the liver under obese condition [95, 96]. Our results indicated that GalNAc-Mdm2ASO treatment significantly increased biliary bile acids and biliary cholesterol (Figure 4.13 C-D), suggesting enhanced cholesterol excretion.

Our RNAseq data showed that *Cyp7b1*, a rate limiting enzyme in the alternative bile acid synthetic pathway [97], was upregulated, while genes involved in the classical bile synthesis pathway are downregulated (Figure 4.13 A). The upregulation of *Cyp7b1* was confirmed by qPCR and western blot (Figure 4.13 E-F).

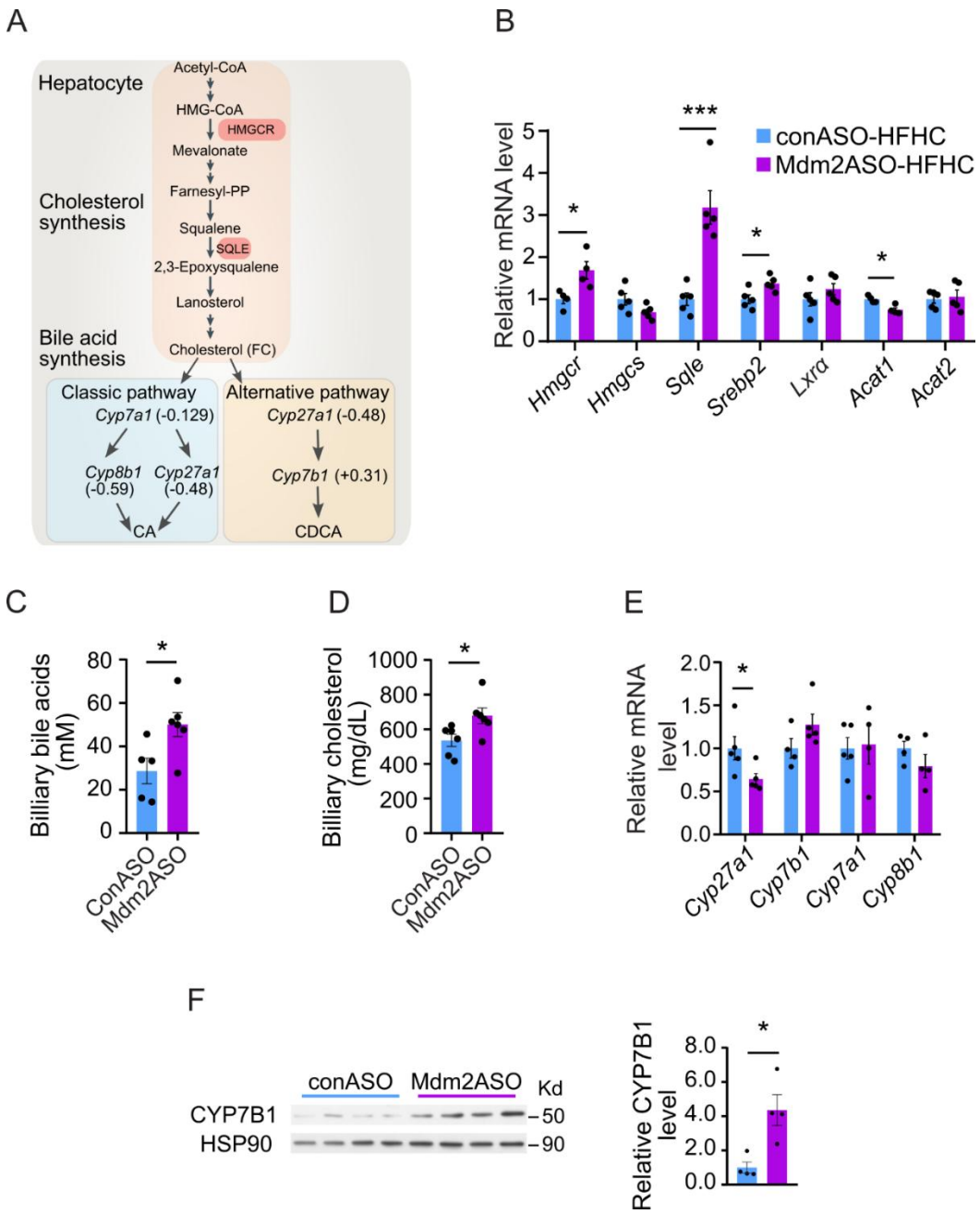

Figure 4.13. GalNAc-Mdm2ASO increases cholesterol synthesis and exretion from the liver.

(A) Schematic diagram of hepatic cholesterol metabolism in relation to biliary sterol secretion. The numbers in the parentheses represent the log2 fold change derived from RNA-seq data obtained from mice treated with GalNAc-conASO and GalNAc-Mdm2ASO fed the HFHC diet. (B) mRNA levels of cholesterol biosynthesis genes (*Hmgcr, Hmgcs, Sqle, Srebp2, Lxrα, Acat1, Acat2*) normalized with *Gapdh* in the HFHC fed mice. (C-D) Biliary bile acid (C) and biliary cholesterol (D). (E) mRNA levels of bile acid synthesis genes (*Cyp27a1, Cyp7b1, Cyp7a1, Cyp8b1*) normalized with *Gapdh* in the HFHC fed mice. (F) Immunoblotting analysis of CYP7B1 and HSP90 in liver lysates. The right panel is densiometric analysis of CYP7B1 normalized with HSP90. Representative immunoblot images are shown (n =4). Data represent mean ± standard error of mean. *$p < 0.05$ and **$p < 0.01$ (Two-tailed independent Student's t-test). Abbreviations: CA, cholic acid; CDCA, chenodeoxycholic acid.

4.3 Conclusion

In this chapter, I have highlighted the therapeutic potential of GalNAc-Mdm2ASO in addressing hepatic steatosis and fibrosis in the high-fat high-cholesterol (HFHC) diet-induced obesity mouse model. By silencing Mdm2 in hepatocytes, GalNAc-Mdm2ASO demonstrates a multifaceted approach to improving liver health and overall metabolic profiles in this obese model.

The significant reduction of MDM2 in the liver, accompanied by the upregulation of p53 and its downstream effectors, indicates a restoration of cellular homeostasis and a reversal of pathological changes associated with MASLD. Histological improvements, including reduced steatosis and lobular inflammation, substantiate the treatment's efficacy. Moreover, GalNAc-Mdm2ASO significantly mitigated liver fibrosis by reducing collagen deposition and HSC activation, emphasizing the potential to halt fibrotic progression, a critical concern in liver disease. The treatment also improved insulin sensitivity and lipid metabolism, highlighting its systemic benefits. Lipidomic analyses revealed reductions in harmful lipid species and prevented HFHC-induced cholesterol accumulation. Importantly, the study elucidates the mechanisms by which GalNAc-Mdm2ASO enhances cholesterol elimination from the body through increased biliary excretion. The upregulation of alternative bile acid synthesis pathways presents a novel approach to enhance cholesterol clearance, thereby mitigating the accumulation of lipids in the liver and improving overall metabolic health.

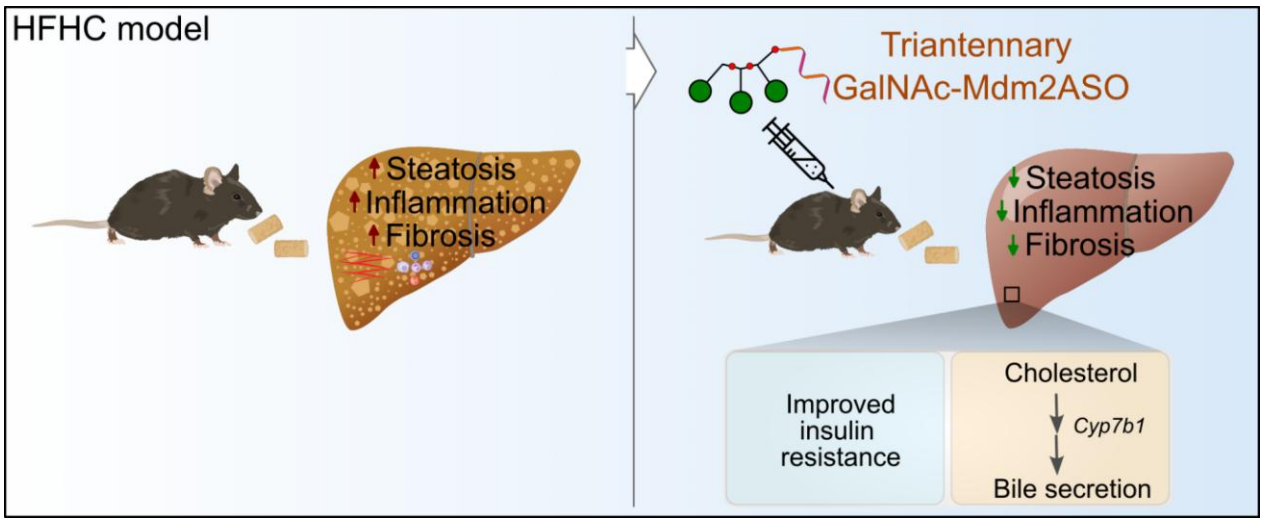

Figure 4.14. GalNAc-ASO mediated selective reduction of MDM2 protects HFHC-diet induced steatosis, inflammation and fibrosis through a cholesterol-to-bile-acid axis.

Chapter 5: GalNAc-Mdm2ASO mitigates hepatic inflammation and fibrosis in a CDAHFD-induced MASLD model

5.1 Introduction

To validate the therapeutic effect of GalNAc-Mdm2ASO on MASLD in various dietary contexts, we employed a CDAHFD diet-induced mouse model. This model induces hepatic steatosis by impairing the secretion of hepatic TG-VLDL, consequently leading to steatohepatitis with fibrosis in the short period of 6 weeks [55, 98].

5.1.1 CDAHFD-induced-MASLD mouse model

Twelve-week-old male C57BL/6J mice were fed a CDAHFD for 2 weeks prior to initiating treatment with either GalNAc-conASO or GalNAc-Mdm2ASO at a dose of 5 mg/kg for a duration of 5 weeks (Figure 5.1).

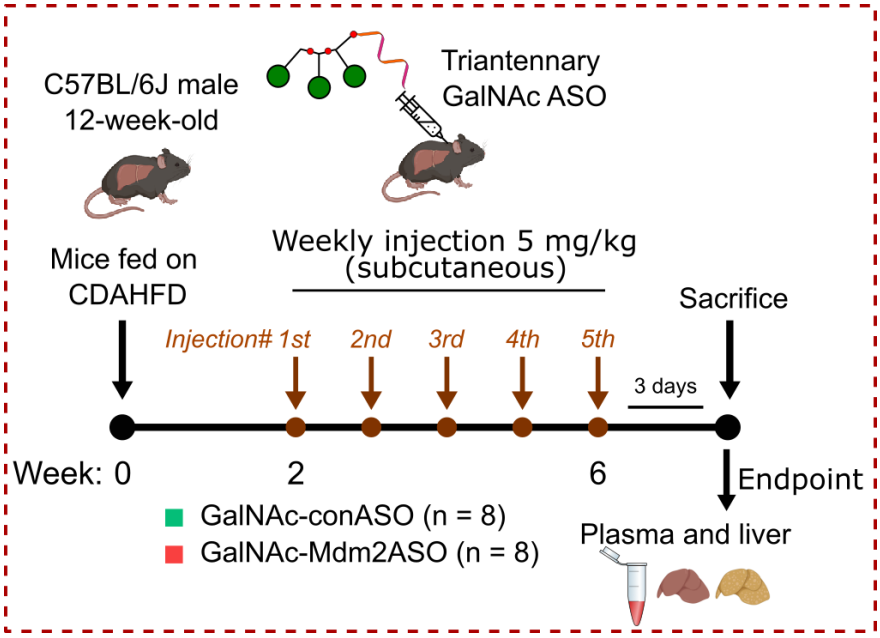

Figure 5.1. Animal experiment 3.

Male C57BL/6J mice fed the CDAHFD for 2 weeks prior to initiating injection with GalNAc-conASO or GalNAc-Mdm2ASO at the indicated doses for a duration of 5 weeks. Three days after the last injection the mice were sacrificed, and the liver and plasma were collected for histopathology, biochemical assay and mRNA/protein expression. Abbreviations: CDAHFD, choline-deficient L-amino acid-defined high-fat diet; ASO, antisense oligonucleotide.

The knockdown of MDM2 by GalNAc-Mdm2ASO in the liver was confirmed by immunostaining and qPCR (Figure 5.2 A, B). Consistent with findings from the HFHC model, the reduction of *Mdm2* levels was accompanied by an upregulation of p53-regulated genes (*p21*, *p16*, *Puma*), although there was no change in *p53* mRNA levels (Figure 5.2 B). However, p53 protein and it's canonical target p21 was increased (Figure 5.2 C), indicating post-translational stabilization due to MDM2 silencing, thereby functional reactivation of the p53 pathway in the liver. Additionally, liver weight was significantly reduced in the GalNAc-Mdm2ASO group (Figure 5.2 D).

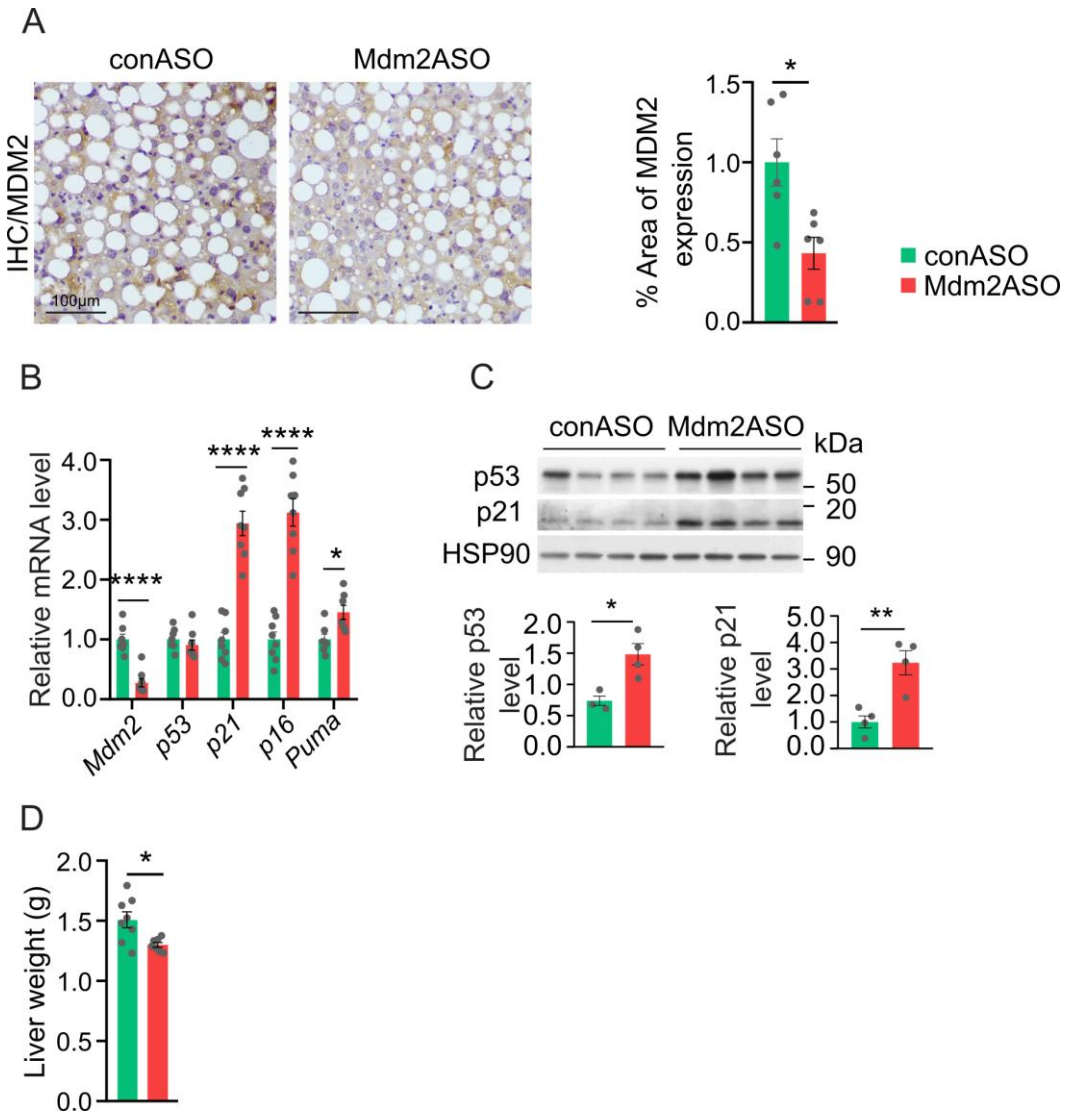

Figure 5.2. GalNAc-Mdm2ASO mediated reduction of MDM2 in the CDAHFD model.

(A) Liver sections were subjected to immunohistochemical (IHC) staining of MDM2. The bar charts in the right panel are quantification of % of MDM2+ area. (B) mRNA levels of *Mdm2*, *p53*, *p21*, *Puma* and *p16* normalized with *Gapdh* in livers (n = 7-8). (C) Immunoblotting analysis of p53 and p21 in the liver. The bar chart is the densiometric analysis normalized with HSP90. Representative immunoblot images are shown (n = 4). (D) Liver weight (n = 8). Data represent mean ± standard error of mean. *p < 0.05 and **p < 0.01 (Two-tailed Student's t-test). Abbreviations: CDAHFD, choline-deficient L-amino acid-defined high-fat diet.

5.1.2 Effect of GalNAc-Mdm2ASO treatment on steatosis in the CDAHFD-induced-MASLD model

Unlike observations in HFHC-fed mice, GalNAc-Mdm2ASO did not significantly alter steatosis (Figure 5.3 A-D) or liver injury markers (Figure 5.3 E-F) in CDAHFD-fed mice. This discrepancy between the two models led us to reason that, while both diets induce features of MASLD, the fundamental differences in their compositions result in varying lipid accumulation in the liver and distinct downstream pathophysiological processes. The accumulation of specific bioactive lipid species activates signaling pathways that promote inflammation and fibrosis to different extents, leading to unique pathogenic features. Consequently, the resolution mediated by GalNAc-Mdm2ASO showed variable responses across the different dietary models. To validate our hypothesis, we conducted lipidomics analysis of the liver in the CDAHFD fed mouse model. From the comparative analysis of lipidomics data between the two dietary models (Figure 5.4 A,B), it is evident that in the liver, neutral lipids (Triglyceride (TG) and cholesteryl ester (ChE); the major components of lipid droplets) are significantly reduced by GalNAc-Mdm2ASO in both models. However, the magnitude of change is greater in the HFHC model compared to the CDAHFD model. Similarly, toxic lipid species such as diacylglycerol (DG) and ceramide are also significantly reduced in both models.

Interestingly, we still observed a significant reduction in hepatic TC alongside a modest increase in Cyp7b1 expression (Figure 5.5 A-C). Although an elevated hepatic ApoB expression was observed in the GalNAc-Mdm2ASO group (Figure 5.5 D, E), it did not impact circulating total cholesterol (TC) and triglyceride (TG) levels (**Error! Reference source not found.**).

In HFHC mice, dietary cholesterol is a major driver of lipid droplet formation. Our data support that GalNAc-Mdm2ASO resolves steatosis primarily through a cholesterol-to-bile-acid axis. It consistently reduces hepatic cholesterol and elevates CYP7B1 in both dietary models, indicating a shared cholesterol-clearance pathway. In CDAHFD-fed mice, the absence of dietary cholesterol

diminishes this axis, resulting in less steatosis reversal, though reductions in toxic lipids still contribute to attenuated inflammation and fibrosis.

It is also noteworthy that our targeted lipidomics analysis detected a reduction in hepatic TG in CDAHFD-fed mice treated with GalNAc-Mdm2ASO (Figure 5.4 B), whereas this reduction was not apparent when assessed by biochemical kit assay or histological staining. This discrepancy likely reflects differences in assay sensitivity and specificity: lipidomics provides a high-resolution quantification of individual lipid species, including less abundant or compartmentalized TG pools, whereas staining and enzymatic kits predominantly capture bulk TG content and may underestimate subtle but biologically relevant changes.

In the cholesterol-free CDAHFD model, the decreased phosphatidylcholine (PC): phosphatidylethanolamine (PE) ratio (↓PC) within lipid droplets is thought to destabilize the lipid droplet monolayer, allowing free cholesterol to leak into intracellular organelles such as lysosomes [99]. This process can promote macrophage inflammation and HSC activation through cell–cell crosstalk [99]. Our data show that therapeutic intervention with GalNAc-Mdm2ASO restores PC and reduces PE content, increasing PC:PE ratio in CDAHFD model (Figure 5.4 B). This might reduce free cholesterol in lipid droplets, thereby mitigating hepatocyte injury and liver fibrosis, even in the absence of complete steatosis resolution.

We also observed that certain phospholipids [e.g., phosphatidylglycerol (PG)], sphingolipids [e.g., sphingomyelins (SM]), hexosylceramides [e.g., mono- and di-hexosylceramides (Hex1Cer, Hex2Cer)], and specific types of phosphatidylethanolamine (PE; e.g., PE-P and PE-O) exhibit contrasting lipid profiles between the two diets (Figure 5.4). PG which is often impaired in MASLD, is a crucial mitochondrial phospholipid that helps maintain the structure and function of mitochondrial cristae [100]. Notably, PG levels are significantly reduced in the GalNAc-Mdm2ASO group of the CDAHFD model compared to that of the HFHC model, indicating that mitochondrial dysfunction—one of the pathophysiological drivers of MASLD—may not resolved by GalNAc-Mdm2ASO. Other phospholipid changes (SM, PE species) appear highly context-dependent, reflecting associations

rather than direct causal mechanisms [101, 102]. Therefore, we remain agnostic about drawing any solid conclusions regarding these discrepancies, but we speculate on their differential contributions between the two diets.

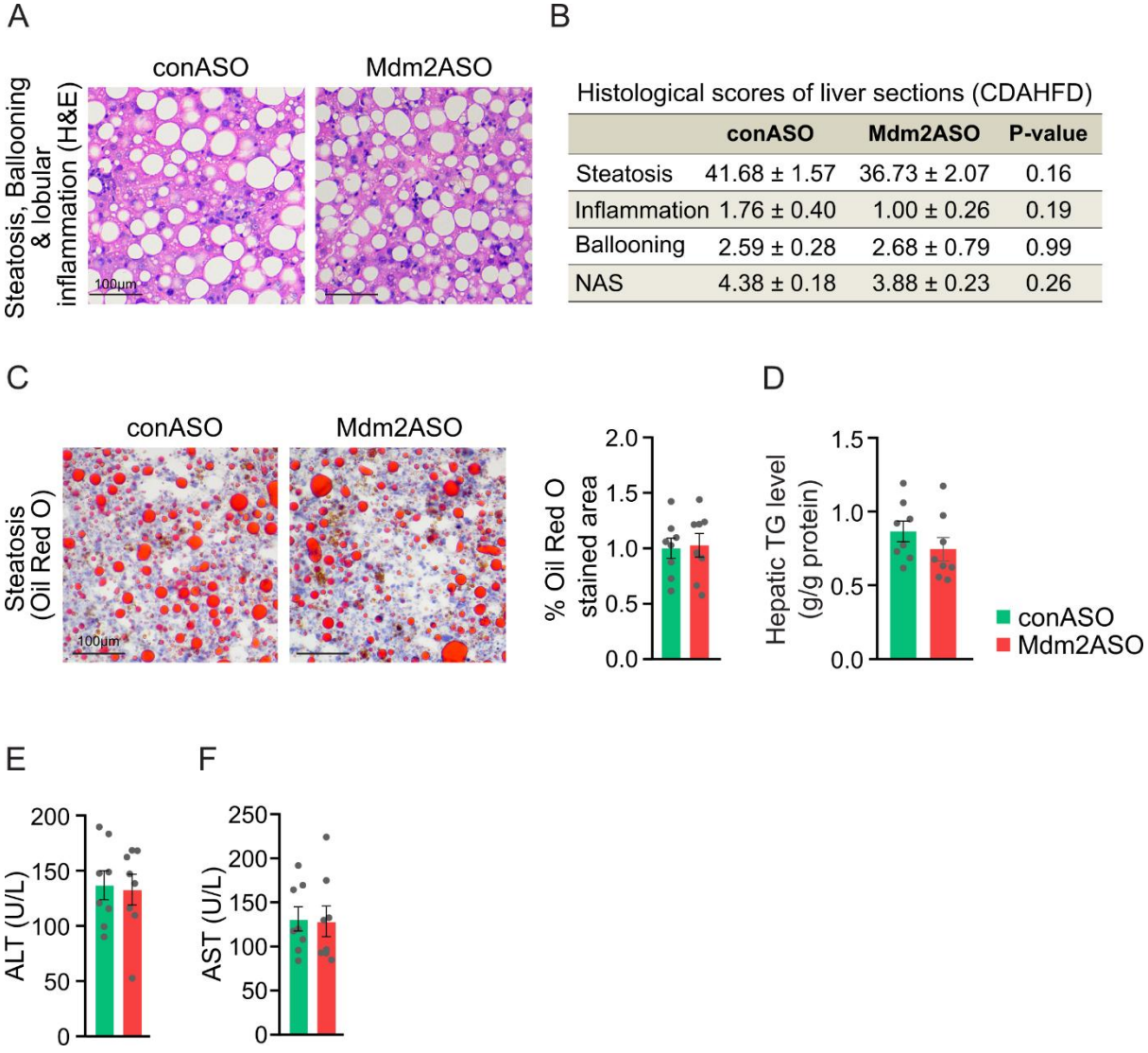

	conASO	Mdm2ASO	P-value
Steatosis	41.68 ± 1.57	36.73 ± 2.07	0.16
Inflammation	1.76 ± 0.40	1.00 ± 0.26	0.19
Ballooning	2.59 ± 0.28	2.68 ± 0.79	0.99
NAS	4.38 ± 0.18	3.88 ± 0.23	0.26

Figure 5.3. Mdm2 silencing by GalNAc-Mdm2ASO has no obvious effect on hepatic steatosis in the CDAHFD mouse model.

(A-B) H&E staining of liver sections (A). Quantitative analysis of the grades of steatosis, inflammation, and the total NASH activity score (NAS) for the H&E staining (B). (C) Oil-red-O (ORO) staining of liver sections. The right panel is quantification of % of ORO+ area. (D) Hepatic TG content normalized with protein concentration (n = 7-8). (E) Serum ALT, (F) Serum AST (n =7-8). Representative histological images are shown. Abbreviations: CDAHFD, choline-deficient L-amino acid-defined high-fat diet; TG, triglyceride; ALT, alanine aminotransferase; AST, aspartate aminotransferase.

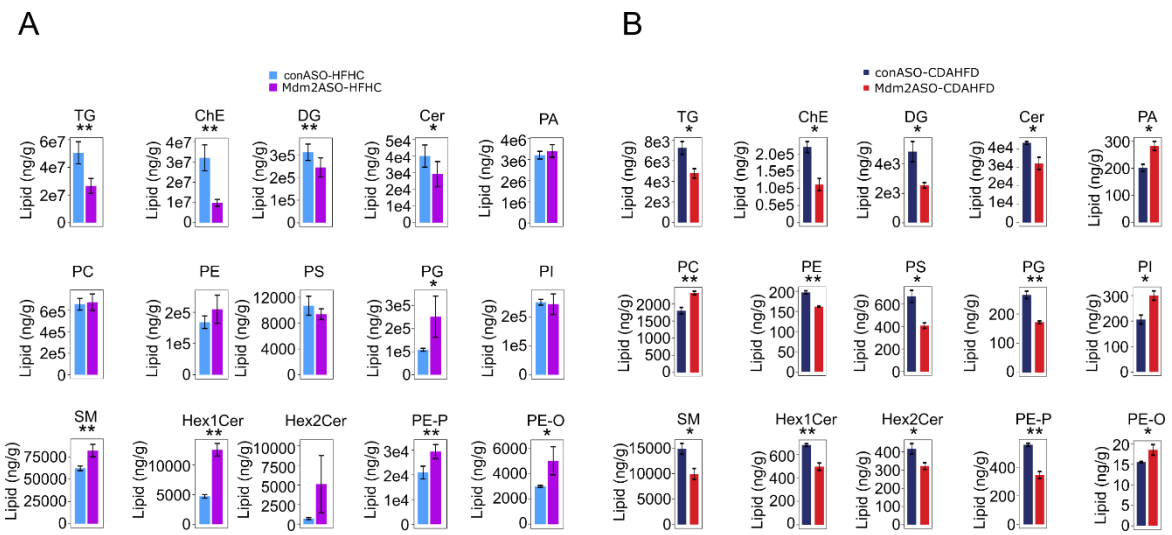

Figure 5.4. Comparative analysis of lipidomics data between the (A) HFHC and (B) CDAHFD models.

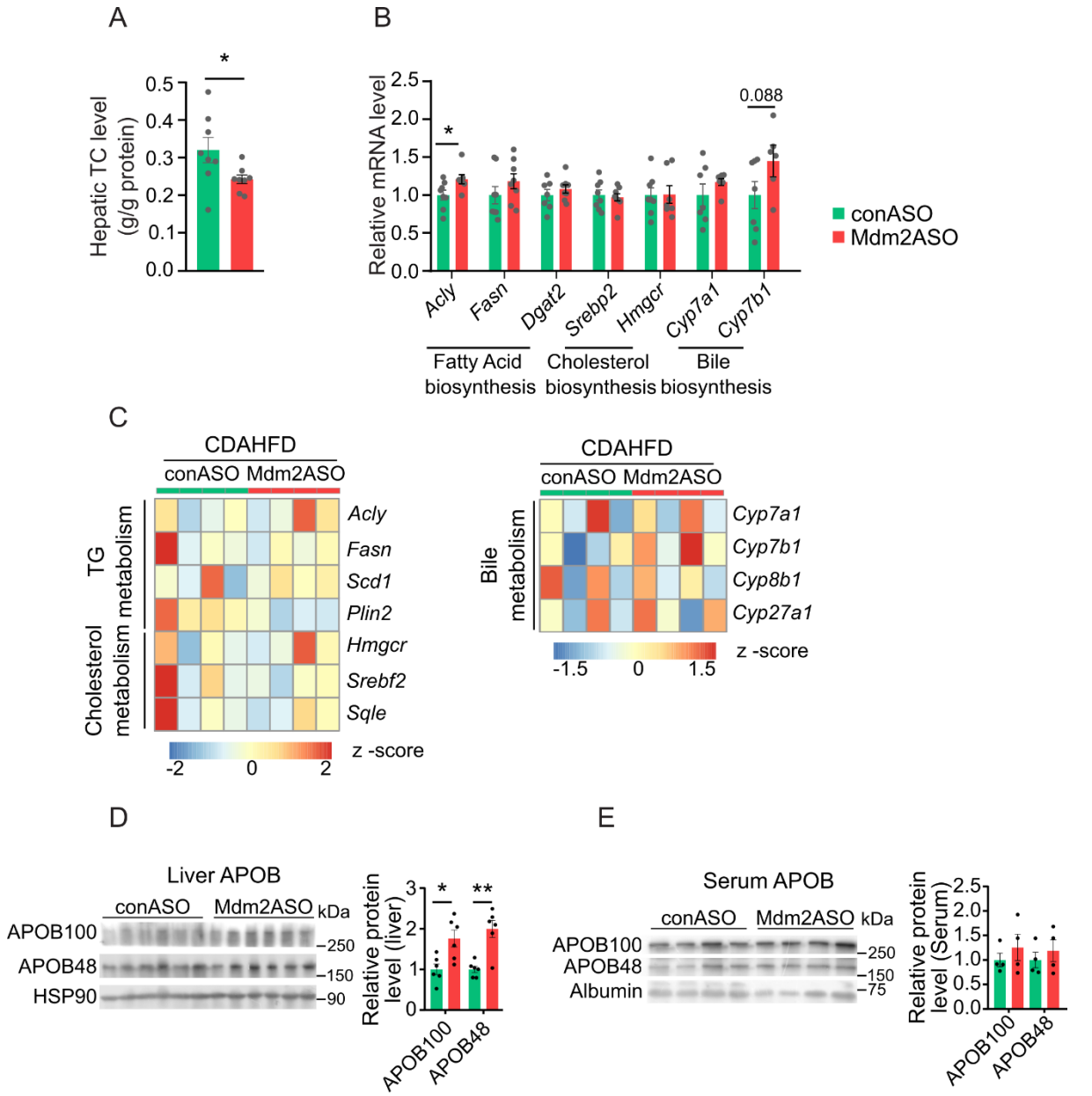

Figure 5.5. Effect of GalNAc-Mdm2ASO on hepatic lipid (TG and TC) metabolism in CDAHFD-induced mouse model.

(A) Hepatic TC content normalized with protein concentration (n = 7-8). (B) mRNA levels of FA biosynthesis (Acly, Fasn, Dgat2), cholesterol biosynthesis (Srebp2, Hmgcr) and bile biosynthesis (Cyp7a1, Cyp7b1) genes normalized with Gapdh in livers (n = 8 CDAHFD). (C) Heatmap showing genes associated with TG, cholesterol and bile metabolism. (D-E) Immunoblot analysis of liver (F) and serum (G) APOB. Right panel is the densiometric analysis normalized with internal control (n = 4 serum, n = 6 liver) (Albumin for serum and HSP90 for liver lysate). Data represent mean ± standard error of mean. *p < 0.05 and **p < 0.01 (Two-tailed Student's t-test). Abbreviations: CDAHFD, choline-deficient L-amino acid-defined high-fat diet, TC, total cholesterol; TG, triglyceride.

Table 5.1. Effect of GalNAc-Mdm2ASO on body/tissue weight and serum levels in mice on a CDAHFD diet.

	conASO	Mdm2ASO	*P* value	Measurement time
Body weight (g)	24.60 ± 0.60	25.11 ± 0.77	0.609	Endpoint
Liver weight (g)	1.51 ± 0.07	1.26 ± 0.04	0.008 (**)	Endpoint
sWAT weight (g)	0.37 ± 0.05	0.45 ± 0.05	0.288	Endpoint
eWAT weight (g)	0.79 ± 0.09	0.94 ± 0.12	0.336	Endpoint
BAT weight (g)	0.07 ± 0.01	0.08 ± 0.01	0.466	Endpoint
ALT (U/L)	136.86 ± 13.02	132.82 ± 13.93	0.835	Endpoint
AST (U/L)	131.34 ± 13.74	128.54 ± 17.32	0.901	Endpoint
serum TG (mg/dL)	49.53 ± 3.03	61.05 ± 7.20	0.173	Endpoint
serum TC (mg/dL)	46.26 ± 2.96	55.19 ± 7.39	0.290	Endpoint
Hepatic TG (mg/dL)	0.87 ± 0.07	0.75 ± 0.08	0.274	Endpoint
Hepatic TC (mg/dL)	0.32 ± 0.03	0.24 ± 0.01	0.058	Endpoint
serum MCP1 (pg/mL)	44.54 ± 4.68	24.48 ± 2.43	0.012	Endpoint
serum Adiponectin (μg/mL)	25.76 ± 1.71	24.85 ± 0.79	0.678	Endpoint

Twelve-week-old male C57BL/6J mice were fed a CDAHFD for 2-weeks, followed by injections of either GalNAc-conASO or GalNAc-Mdm2ASO at a dose of 5 mg/kg for an additional 4-weeks. Three days after the final injection, the mice were sacrificed, and tissues and plasma were collected for biochemical assays. Data are presented as mean ± standard error of the mean. *p (Two-tailed independent Student's t-test). Abbreviations: sWAT, subcutaneous white adipose tissue; eWAT, epididymal white adipose tissue; BAT, brown adipose tissue; ALT, alanine aminotransferase; AST, aspartate transaminase; TG, triglyceride; TC, total cholesterol; MCP1, monocyte chemoattractant protein 1.

Nevertheless, we consistently observed a significant reduction in fibrosis as measured by Sirius red staining, immunostaining of α-SMA and expression of profibrotic genes (Figure 5.6 A-C).

To further characterize the protective effect of GalNAc-Mdm2ASO under the CDAHFD, we performed RNAseq analysis comparing GalNAc-Mdm2ASO and GalNAc-conASO groups. Ingenuity Pathway Analysis (IPA) revealed that GalNAc-Mdm2ASO treatment downregulated several inflammatory pathways including neutrophil degranulation, while upregulated anti-inflammatory IL-10 signalling (Figure 5.7 A). The expression of pro-inflammatory cytokines was also significantly reduced in the liver (Figure 5.7 B), along with a systemic reduction of MCP1 (Figure 5.7 C).

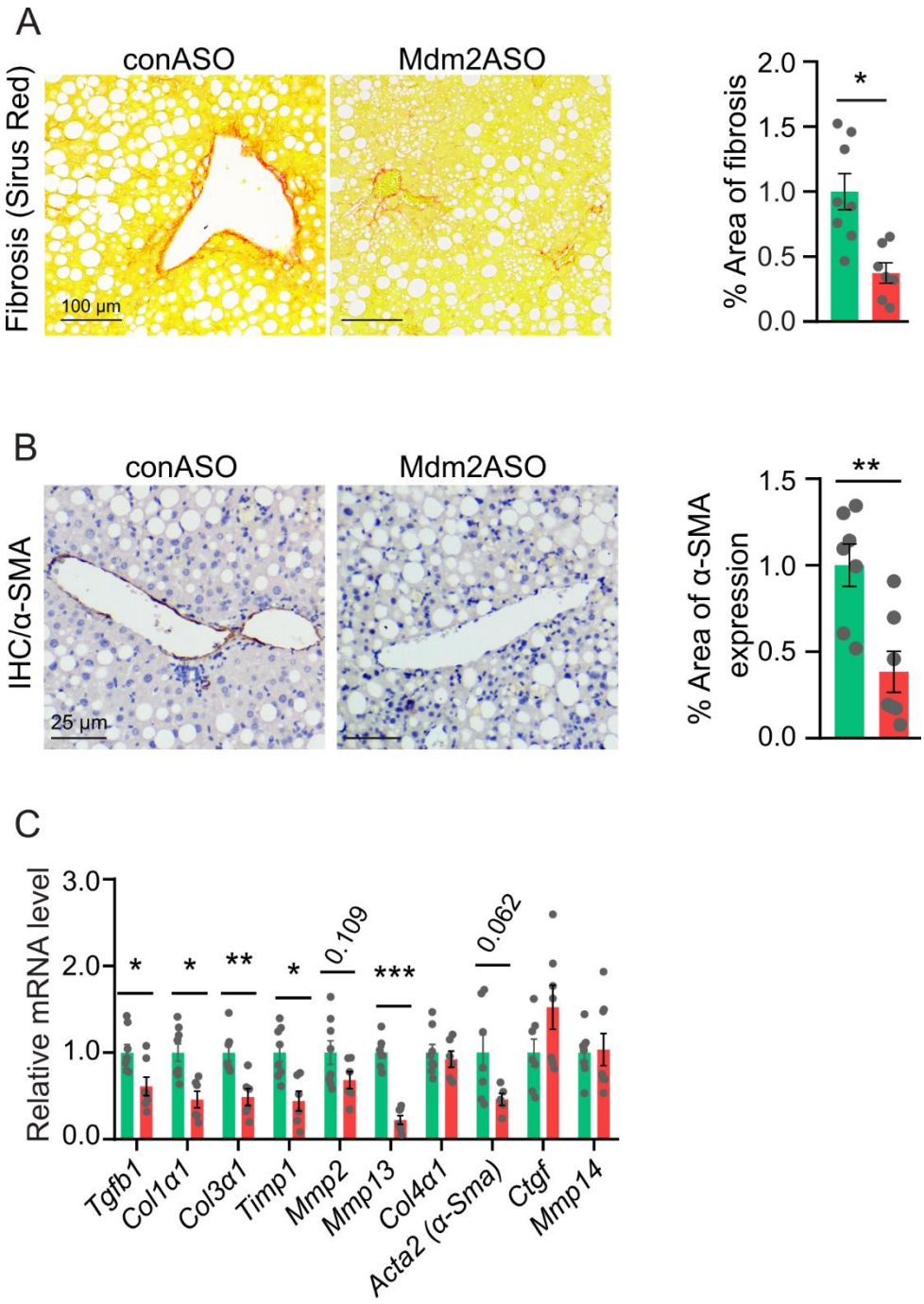

Figure 5.6. GalNAc-Mdm2ASO alleviated CDAHFD-induced fibrosis.

(A) Sirus red (SR) staining of liver sections. The right panel is quantification % of SR+ area. (B) Liver sections of CDAHFD fed mice were subjected to immunohistochemical (IHC) staining of α-SMA. The bar charts in right panel are quantification % of α-SMA+ area. (C) mRNA levels of profibrotic genes (*Tgfb1, Col1α1, Col3α1, Timp1, Mmp2, Mmp13, Col4α1, α-Sma, Ctgf, Mmp14*) normalized with *Gapdh* in livers (n = 7-8 CDAHFD). Representative histological images are shown. Data represent mean ± standard error of mean. *p < 0.05 and **p < 0.01 (Two-tailed Student's t-test).

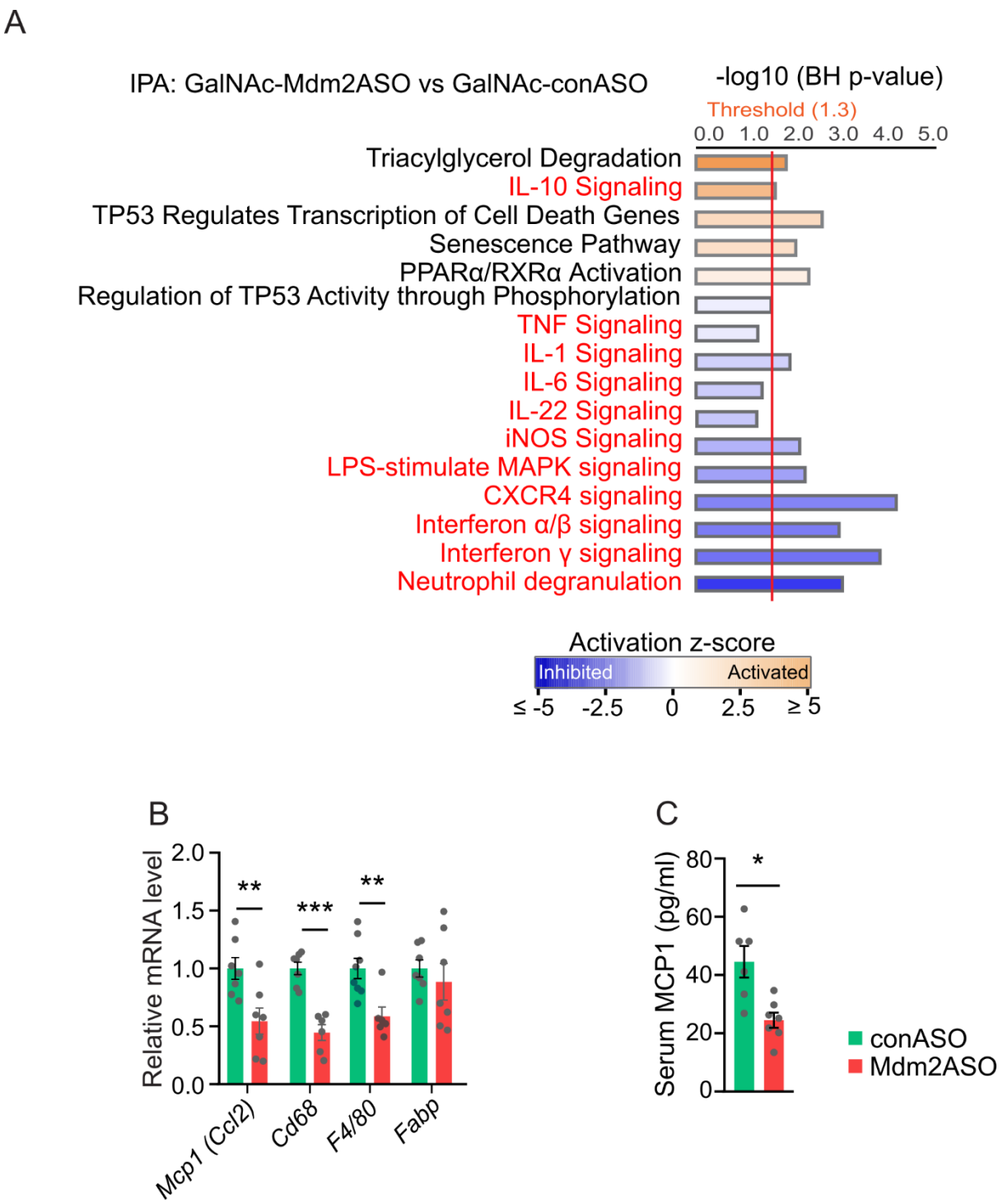

Figure 5.7. Mdm2 silencing by GalNAc-Mdm2ASO improves inflammation in the CDAHFD model.

(A) Liver samples from the mice fed with CDAHFD diet were subjected to RNA sequencing and differential gene expression analysis. Ingenuity pathway analysis (IPA) for top enriched pathways. (B) mRNA levels of *Mcp1, Cd68, F4/80, Fabp* normalized with *Gapdh* in livers (n = 7-8 CDAHFD). (C) Serum MCP1. Data represent mean ± standard error of mean. *p < 0.05 and **p < 0.01 (Two-tailed independent Student's t-test). Abbreviations: CDAHFD, choline-deficient L-amino acid-defined high-fat diet; MCP1, monocyte chemoattractant protein 1.

5.2 Conclusion

In this chapter, I have demonstrated the therapeutic potential of GalNAc-Mdm2ASO in alleviating hepatic inflammation and fibrosis in a choline-deficient L-amino acid-defined high-fat diet (CDAHFD) model of Metabolic Associated Steatotic Liver Disease (MASLD).

Similar to the HFHC model, the treatment successfully reduced MDM2 levels in the liver, leading to an upregulation of p53 and its downstream-regulated genes such as p21 and Puma, thereby restoring the p53 pathway essential for cellular homeostasis. However, unlike the HFHC model, GalNAc-Mdm2ASO did not significantly alter steatosis or liver injury markers in the CDAHFD model. Nevertheless, it effectively reduced liver fibrosis by decreasing collagen deposition and expression of profibrotic genes, underscoring its ability to halt fibrotic progression. The observed differences in disease resolution mediated by GalNAc-Mdm2ASO are likely due to variable responses across the different dietary models, particularly the differential lipid accumulation in the liver and the associated pathophysiological processes. For instance, lipidomic analyses revealed a reduction in toxic lipid species, such as diacylglycerol and ceramide, in both the CDAHFD and HFHC models. Notably, therapeutic intervention with GalNAc-Mdm2ASO increased the PC:PE ratio in the CDAHFD model, potentially reducing free cholesterol in lipid droplets. This effect may help mitigate inflammation, and liver fibrosis, even in the absence of complete resolution of steatosis.

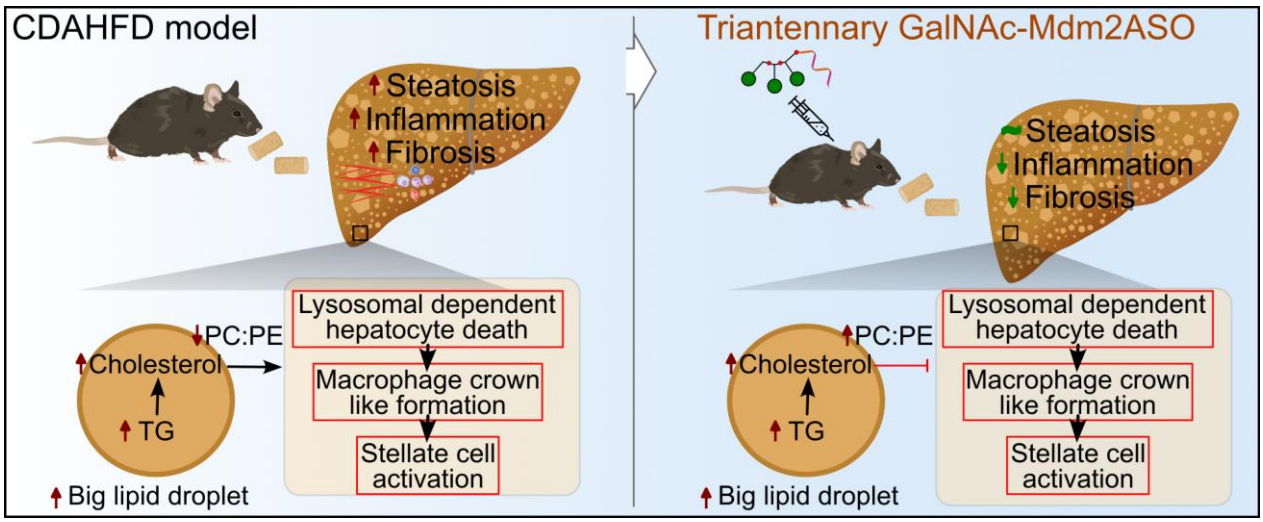

Figure 5.8. GalNAc-ASO mediated selective reduction of MDM2 protects CDAHFD induced inflammation and fibrosis by preventing cholesterol leakage from the big lipid droplets.

Chapter 6: Discussion and future directions

6.1 Discussion and future directions

The growing global prevalence of MASLD underscores the urgent need for effective therapeutic strategies. We previously identified hepatic MDM2 as a key contributor to MASLD pathogenesis in both humans and rodent models [25]. In this study, we demonstrated that GalNAc-Mdm2ASO provides broad therapeutic benefits, effectively attenuating hepatic steatosis, fibrosis, inflammation, and liver injury in two well-established MASLD mouse models.

Cholesterol plays a central role in the development of hepatic steatosis and fibrosis in MASLD. Excess hepatic cholesterol promotes triglyceride accumulation by enhancing *de novo* lipogenesis and suppressing fatty acid β-oxidation and TG-VLDL secretion [92, 96, 103]. Additionally, cholesterol activates hepatic stellate cells (HSCs), which drive fibrosis through the production of collagen and extracellular matrix proteins and activation of inflammatory and fibrogenic pathways [80, 92]. Consistent with previous studies showing that enhancing cholesterol efflux and bile acid synthesis reduces hepatic lipid deposition in obese mice [95, 96, 104], our findings demonstrate that GalNAc-Mdm2ASO treatment dramatically lowers both plasma and hepatic cholesterol levels in HFHC-fed mice to normal levels, while alleviating steatosis and fibrosis. This cholesterol reduction was accompanied by increased biliary excretion of bile acids and cholesterol—key pathways for systemic cholesterol clearance [105]—suggesting that GalNAc-Mdm2ASO enhances hepatobiliary cholesterol elimination. We also observed a modest upregulation of CYP7B1, a rate-limiting enzyme in the alternative bile acid synthesis pathway. Consistently, it was reported that when the classical CYP7A1 pathway is compromised, CYP7B1 activity becomes more prominent, generating a hydrophilic bile acid pool that reduces cholesterol disposal and lipid absorption [106]. CYP7B1 also antagonizes intestinal farnesoid X receptor (FXR) signaling, lowering ceramide production and enhancing insulin sensitivity [106]—effects that were also observed in GalNAc-Mdm2ASO–treated mice under HFHC. Notably, CYP7B1 is often suppressed in metabolic diseases such as NAFLD and diabetes [107, 108], underscoring the therapeutic relevance of its restoration.

Interestingly, in both dietary HFHC and CDAHFD models, GalNAc-Mdm2ASO demonstrated a significant reduction in hepatic TC with a concomitant increase in CYP7B1 expression, suggesting a common pathway for hepatobiliary cholesterol clearance. However, in the CDAHFD model, the reduction in hepatic TC and the increase in CYP7B1 were modest, with no change in serum TC, indicating a much less pronounced effect compared to the HFHC model. These results suggest that the differential anti-steatosis effect of GalNAc-Mdm2ASO in HFHC-fed and CDAHFD-fed mice may depend on dietary cholesterol. The HFHC diet, abundant in both fat and cholesterol, could provide conditions where dietary cholesterol enhances the cholesterol-lowering action of GalNAc-Mdm2ASO, leading to a more pronounced reduction in hepatic cholesterol levels. In contrast, the CDAHFD lacks cholesterol, making the cholesterol-targeted action of GalNAc-Mdm2ASO less effective and diminishing its anti-steatotic impact in this model. However, further investigation is required to reveal how MDM2 controls CYP7B1 expression, and whether the increase of CYP7B1 mediates the hepatoprotective effects of GalNAc-Mdm2ASO.

A key event in the pathophysiology of the disease is the transition from simple steatosis to MASH, where the immune system becomes activated and promote the transition [109]. Anti-inflammatory cytokines, including Interleukin-10 (IL-10), play a crucial role by inhibiting immune cell activation and reducing cytokine production in innate immune cell types [110]. It has been reported that IL-10 serves as a protective factor against diet-induced insulin resistance in the liver [111] and it also helps attenuate liver fibrosis [112, 113]. In both HFHC- and CDAHFD-fed mice, IL10 signaling pathway was upregulated by GalNAc-Mdm2ASO treatment, which might partially contribute to the hepatoprotective effects of GalNAc-Mdm2ASO.

Additionally, we show that treatment with GalNAc-Mdm2ASO treatment increased the markers associated with Kupffer cell (KC) populations in the HFHC-fed mice (Figure S1C). KCs are the liver resident macrophage, which are defined by their expression of CLEC4F, TIM4, F4/80 and CD64 [82, 114]. Notably, resident KCs often links to an improved inflammation [115]. They also possess all the necessary genetic machinery to uptake and metabolize excess lipids [82]. Although

the extent of resident Kupffer cell (resKC) activation is somewhat debated—largely influenced by factors such as diet composition and the duration of dietary intervention—a common observation across NASH studies is a reduced abundance of resKCs [115]. Therefore, the upregulated KC markers observed in our study may indicate a protective effect against MASLD. However, it remains unclear how GalNAc-Mdm2ASO mediates alterations in IL-10 signaling or KC markers. It is possible that:(1) GalNAc-Mdm2ASO alters the secretory profile of hepatocytes, thereby changing the immune microenvironment and (2) GalNAc-Mdm2ASO acts directly on the immune cell population.

Fibrosis, characterized by the excessive deposition of collagen-rich matrix that replaces healthy tissue to form scar tissue, can develop following tissue injury [116]. Importantly, we observed a consistent prevention in fibrosis, irrespective of the diet condition or the ASO-mediated knockdown or knockout of MDM2 in our previous study, suggesting a generalized mechanism at play. The anti-fibrotic effect of MDM2 inhibition can be secondary to the alleviated steatosis and lipotoxicity in HFHC-fed mice [25]. However, in CDAHFD-fed mice which displayed similar steatosis between the two groups, the reduced fibrosis in GalNAc-Mdm2ASO-treated mice can be attributed to direct effect of MDM2 on fibrogenesis. Of note, MDM2 inactivation directly suppresses inflammation and fibrosis in various cell types [117-119]. Although we showed that GalNAc-Mdm2ASO mainly reduced MDM2 expression in hepatocytes, yet whether MDM2 expression in HSCs can be reduced by GalNAc-Mdm2ASO remains to be determined.

We clearly showed that GalNAc-Mdm2ASO treatment improve hepatic steatosis and fibrosis, however, the underlying mechanisms appear distinct from those observed in our previous study using a hepatocyte-specific Mdm2 knockout model [25]. In our earlier study, reduced hepatic TG content was attributed to enhanced TG-VLDL secretion, driven by reduced ApoB degradation. However, in the present study, despite a modest increase in hepatic ApoB100/48 levels in both HFHC- and CDAHFD-fed mice, TG-VLDL secretion remained lower in the HFHC model. This suggests that factors beyond ApoB availability—such as enhanced TG clearance rate and/or reduced hepatic TG supply—may govern VLDL assembly and secretion under GalNAc-Mdm2ASO treatment. The

marked reduction in hepatic TG can be due to a reduced cholesterol content [96, 103], which might exert a stronger influence on hepatic TG metabolism than ApoB expression in GalNAc-Mdm2ASO-treated mice, especially under HFHC feeding.

Several factors may also contribute to the differences observed between the knockout and ASO-mediated knockdown models. First, complete gene knockout can trigger compensatory upregulation of other related genes, potentially masking the expected loss-of-function phenotype [120]. This compensatory response is less likely to occur with partial knockdown using ASO, as some protein remains functional [120]. Second, knockdown methods—particularly ASOs and short interfering RNAs (siRNAs)—can still have off-target effects despite their high specificity, potentially resulting in the silencing of unintended genes [121]. These off-target effects can confound the interpretation of knockdown experiments and lead to phenotypic differences compared to clean knockouts, which are less prone to such issues. Additionally, the timing of gene inactivation differs between the two approaches. In the previous study, we utilized genetic knockout, resulting in permanent gene deletion during embryonic development. In contrast, ASO-mediated knockdown temporarily silences the gene during adulthood. This difference in the timing of gene inactivation may significantly impact the phenotypes, as embryonic gene deletion can trigger developmental adaptations do not present with adult-stage interventions [122].

In summary, we have demonstrated that the conjugation of MDM2 ASO with GalNAc facilitated targeted delivery to the liver and greatly enhances the effectiveness of ASO in suppressing hepatic MDM2 expression in preclinical MASLD mouse models. The administration of GalNAc-Mdm2ASO mitigated the onset and progression of diet-induced MASLD. As addressing MASLD/MASH remains a critical unmet medical need, further research into the therapeutic potential of GalNAc-Mdm2ASO is essential.

6.2 Limitations of the study

While this study presents a compelling preclinical investigation of the hepatocyte-targeted antisense oligonucleotide (ASO), GalNAc-Mdm2ASO, which silences hepatic MDM2 to address metabolic

dysfunction-associated steatotic liver disease (MASLD), several key limitations should be considered when interpreting the findings:

1) In the oligonucleotide screening process conducted by Ionis Pharmaceuticals, the experimental details from the preliminary screening and the criteria used to select the final candidates remained confidential.
2) For the 14 selected oligonucleotides, information regarding the specific regions of the Mdm2 mRNA they target was limited, and it is unclear whether they inhibit translation initiation or interfere with pre-mRNA splicing.
3) GalNAc-Mdm2ASO did not affect Mdm2 expression in the heart, muscle, or pancreas. However, a modest reduction observed in the kidney could possibly be attributed to ASGPR expression in kidney cells facilitating the uptake of the ASO. It is important to note that I did not measure ASGPR expression in the kidney.
4) Regarding potential off-target effects, I have not examined whether GalNAc-Mdm2ASO alters the expression of other MDM family proteins, such as MDM1 and MDM3, in liver tissue.

Reference

1. Rinella, M.E., et al., *A multisociety Delphi consensus statement on new fatty liver disease nomenclature.* Journal of Hepatology, 2023. **79**(6): p. 1542-1556.

2. Emma, B., et al., *The challenges of assessing adiposity in a clinical setting*. 2024. p. 615-626.

3. Neuschwander-Tetri, B.A. and S.H. Caldwell, *Nonalcoholic steatohepatitis: summary of an AASLD Single Topic Conference.* Hepatology, 2003. **37**(5): p. 1202-19.

4. Friedman, S.L., et al., *Mechanisms of NAFLD development and therapeutic strategies.* Nat Med, 2018. **24**(7): p. 908-922.

5. Dowman, J.K., J.W. Tomlinson, and P.N. Newsome, *Pathogenesis of non-alcoholic fatty liver disease.* Qjm, 2010. **103**(2): p. 71-83.

6. Shivakumar, C., et al., *Non-alcoholic fatty liver disease in the Asia–Pacific region: Definitions and overview of proposed guidelines.* Wiley, 2007. **22**(6): p. 778-787.

7. Mingjuan, L., et al., *Corilagin prevents non-alcoholic fatty liver disease via improving lipid metabolism and glucose homeostasis in high fat diet-fed mice.* Frontiers Media, 2022. **9**.

8. Hudgins, L.C., et al., *Human fatty acid synthesis is stimulated by a eucaloric low fat, high carbohydrate diet.* J Clin Invest, 1996. **97**(9): p. 2081-91.

9. Xu, X., et al., *Transcriptional control of hepatic lipid metabolism by SREBP and ChREBP.* Semin Liver Dis, 2013. **33**(4): p. 301-11.

10. Donnelly, K.L., et al., *Sources of fatty acids stored in liver and secreted via lipoproteins in patients with nonalcoholic fatty liver disease.* J Clin Invest, 2005. **115**(5): p. 1343-51.

11. Barrows, B.R. and E.J. Parks, *Contributions of different fatty acid sources to very low-density lipoprotein-triacylglycerol in the fasted and fed states.* J Clin Endocrinol Metab, 2006. **91**(4): p. 1446-52.

12. Alves-Bezerra, M. and D.E. Cohen, *Triglyceride Metabolism in the Liver.* Compr Physiol, 2017. **8**(1): p. 1-8.

13. Kapourchali, F.R., et al., *The Role of Dietary Cholesterol in Lipoprotein Metabolism and Related Metabolic Abnormalities: A Mini-review.* Crit Rev Food Sci Nutr, 2016. **56**(14): p. 2408-15.

14. Simons, K. and E. Ikonen, *How Cells Handle Cholesterol.* Science, 2000. **290**(5497): p. 1721-1726.

15. Trapani, L., M. Segatto, and V. Pallottini, *Regulation and deregulation of cholesterol homeostasis: The liver as a metabolic "power station".* World J Hepatol, 2012. **4**(6): p. 184-90.

16. Brown, M.S., A. Radhakrishnan, and J.L. Goldstein, *Retrospective on Cholesterol Homeostasis: The Central Role of Scap.* Annu Rev Biochem, 2018. **87**: p. 783-807.

17. Pai, J.-t., et al., *Differential stimulation of cholesterol and unsaturated fatty acid biosynthesis in cells expressing individual nuclear sterol regulatory element-binding proteins.* Journal of Biological Chemistry, 1998. **273**(40): p. 26138-26148.

18. Foresti, O., et al., *Sterol homeostasis requires regulated degradation of squalene monooxygenase by the ubiquitin ligase Doa10/Teb4.* Elife, 2013. **2**: p. e00953.

19. Gill, S., et al., *Cholesterol-dependent degradation of squalene monooxygenase, a control point in cholesterol synthesis beyond HMG-CoA reductase.* Cell Metab, 2011. **13**(3): p. 260-73.

20. Zelcer, N., et al., *The E3 ubiquitin ligase MARCH6 degrades squalene monooxygenase and affects 3-hydroxy-3-methyl-glutaryl coenzyme A reductase and the cholesterol synthesis pathway.* Mol Cell Biol, 2014. **34**(7): p. 1262-70.

21. Maxfield, F.R. and I. Tabas, *Role of cholesterol and lipid organization in disease.* Nature, 2005. **438**(7068): p. 612-21.

22. Levitan, I., S. Volkov, and P.V. Subbaiah, *Oxidized LDL: diversity, patterns of recognition, and pathophysiology.* Antioxid Redox Signal, 2010. **13**(1): p. 39-75.

23. Ikonen, E., *Cellular cholesterol trafficking and compartmentalization.* Nat Rev Mol Cell Biol, 2008. **9**(2): p. 125-38.

24. Ipsen, D.H., J. Lykkesfeldt, and P. Tveden-Nyborg, *Molecular mechanisms of hepatic lipid accumulation in non-alcoholic fatty liver disease.* Cell Mol Life Sci, 2018. **75**(18): p. 3313-3327.

25. Lin, H., et al., *Hepatic MDM2 Causes Metabolic Associated Fatty Liver Disease by Blocking Triglyceride-VLDL Secretion via ApoB Degradation.* Adv Sci (Weinh), 2022. **9**(20): p. e2200742.

26. Heymann, F. and F. Tacke, *Immunology in the liver--from homeostasis to disease.* Nat Rev Gastroenterol Hepatol, 2016. **13**(2): p. 88-110.

27. Balmer, M.L., et al., *The liver may act as a firewall mediating mutualism between the host and its gut commensal microbiota.* Sci Transl Med, 2014. **6**(237): p. 237ra66.

28. McDonald, B., et al., *Programing of an Intravascular Immune Firewall by the Gut Microbiota Protects against Pathogen Dissemination during Infection.* Cell Host Microbe, 2020. **28**(5): p. 660-668.e4.

29. Eipel, C., K. Abshagen, and B. Vollmar, *Regulation of hepatic blood flow: the hepatic arterial buffer response revisited.* World J Gastroenterol, 2010. **16**(48): p. 6046-57.

30. Ficht, X. and M. Iannacone, *Immune surveillance of the liver by T cells.* Sci Immunol, 2020. **5**(51).

31. Remmerie, A., et al., *Osteopontin Expression Identifies a Subset of Recruited Macrophages Distinct from Kupffer Cells in the Fatty Liver.* Immunity, 2020. **53**(3): p. 641-657.e14.

32. Xiong, X., et al., *Landscape of Intercellular Crosstalk in Healthy and NASH Liver Revealed by Single-Cell Secretome Gene Analysis.* Mol Cell, 2019. **75**(3): p. 644-660.e5.

33. Ramachandran, P., et al., *Resolving the fibrotic niche of human liver cirrhosis at single-cell level.* Nature, 2019. **575**(7783): p. 512-518.

34. Jackson, P.K., et al., *The lore of the RINGs: substrate recognition and catalysis by ubiquitin ligases.* Trends Cell Biol, 2000. **10**(10): p. 429-39.

35. Marine, J.C. and G. Lozano, *Mdm2-mediated ubiquitylation: p53 and beyond.* Cell Death & Differentiation, 2010. **17**(1): p. 93-102.

36. Cahilly-Snyder, L., et al., *Molecular analysis and chromosomal mapping of amplified genes isolated from a transformed mouse 3T3 cell line.* Somatic Cell and Molecular Genetics, 1987. **13**(3): p. 235-244.

37. Momand, J., et al., *The mdm-2 oncogene product forms a complex with the p53 protein and inhibits p53-mediated transactivation.* Cell, 1992. **69**(7): p. 1237-45.

38. Oliner, J.D., et al., *Amplification of a gene encoding a p53-associated protein in human sarcomas.* Nature, 1992. **358**(6381): p. 80-83.

39. Jang, H., et al., *SREBP1c-CRY1 signalling represses hepatic glucose production by promoting FOXO1 degradation during refeeding.* Nature Communications, 2016. **7**(1): p. 12180.

40. Li, X., et al., *The MDM2–p53–pyruvate carboxylase signalling axis couples mitochondrial metabolism to glucose-stimulated insulin secretion in pancreatic β-cells.* Nature Communications, 2016. **7**(1): p. 11740.

41. Liu, Y., et al., *Ribosomal protein–Mdm2–p53 pathway coordinates nutrient stress with lipid metabolism by regulating MCD and promoting fatty acid oxidation.* Proceedings of the National Academy of Sciences, 2014. **111**(23): p. E2414-E2422.

42. Minamino, T., et al., *A crucial role for adipose tissue p53 in the regulation of insulin resistance.* Nature Medicine, 2009. **15**(9): p. 1082-1087.

43. Kodama, T., et al., *Increases in p53 expression induce CTGF synthesis by mouse and human hepatocytes and result in liver fibrosis in mice.* The Journal of Clinical Investigation, 2011. **121**(8): p. 3343-3356.

44. Hallenborg, P., et al., *Mdm2 controls CREB-dependent transactivation and initiation of adipocyte differentiation.* Cell Death & Differentiation, 2012. **19**(8): p. 1381-1389.

45. Hallenborg, P., et al., *Adipose MDM2 regulates systemic insulin sensitivity.* Scientific Reports, 2021. **11**(1): p. 21839.

46. Liu, Z., et al., *The Dysfunctional MDM2-p53 Axis in Adipocytes Contributes to Aging-Related Metabolic Complications by Induction of Lipodystrophy.* Diabetes, 2018. **67**(11): p. 2397-2409.

47. Mohs, R.C. and N.H. Greig, *Drug discovery and development: Role of basic biological research.* Alzheimer's & dementia (New York, N. Y.), 2017. **3**(4): p. 651-657.

48. Zuberi, A. and C. Lutz, *Mouse Models for Drug Discovery. Can New Tools and Technology Improve Translational Power?* ILAR journal, 2016. **57**(2): p. 178-185.

49. Wilson, R.C. and J.A. Doudna, *Molecular Mechanisms of RNA Interference.* Annual Review of Biophysics, 2013. **42**(1): p. 217-239.

50. Walters, B.J., et al., *Advanced In vivo Use of CRISPR/Cas9 and Anti-sense DNA Inhibition for Gene Manipulation in the Brain.* Frontiers in Genetics, 2016. **6**.

51. Zhang, R., H. Wang, and S. Agrawal, *Novel antisense anti-MDM2 mixed-backbone oligonucleotides: proof of principle, in vitro and in vivo activities, and mechanisms.* Curr Cancer Drug Targets, 2005. **5**(1): p. 43-9.

52. Nair, J.K., et al., *Multivalent N-Acetylgalactosamine-Conjugated siRNA Localizes in Hepatocytes and Elicits Robust RNAi-Mediated Gene Silencing.* Journal of the American Chemical Society, 2014. **136**(49): p. 16958-16961.

53. Prakash, T.P., et al., *Targeted delivery of antisense oligonucleotides to hepatocytes using triantennary N-acetyl galactosamine improves potency 10-fold in mice.* Nucleic Acids Research, 2014. **42**(13): p. 8796-8807.

54. Prakash, T.P., et al., *Comprehensive Structure–Activity Relationship of Triantennary N-Acetylgalactosamine Conjugated Antisense Oligonucleotides for Targeted Delivery to Hepatocytes.* Journal of Medicinal Chemistry, 2016. **59**(6): p. 2718-2733.

55. Matsumoto, M., et al., *An improved mouse model that rapidly develops fibrosis in non-alcoholic steatohepatitis.* Int J Exp Pathol, 2013. **94**(2): p. 93-103.

56. Millar, J.S., et al., *Determining hepatic triglyceride production in mice: comparison of poloxamer 407 with Triton WR-1339.* J Lipid Res, 2005. **46**(9): p. 2023-8.

57. Schotz, M.C., A. Scanu, and I.H. Page, *Effect of triton on lipoprotein lipase of rat plasma.* Am J Physiol, 1957. **188**(2): p. 399-402.

58. Chen, Y., et al., *SOAPnuke: a MapReduce acceleration-supported software for integrated quality control and preprocessing of high-throughput sequencing data.* Gigascience, 2018. **7**(1): p. 1-6.

59. Dobin, A., et al., *STAR: ultrafast universal RNA-seq aligner.* Bioinformatics, 2013. **29**(1): p. 15-21.

60. Liao, Y., G.K. Smyth, and W. Shi, *featureCounts: an efficient general purpose program for assigning sequence reads to genomic features.* Bioinformatics, 2014. **30**(7): p. 923-30.

61. Love, M.I., W. Huber, and S. Anders, *Moderated estimation of fold change and dispersion for RNA-seq data with DESeq2.* Genome Biol, 2014. **15**(12): p. 550.

62. Matyash, V., et al., *Lipid extraction by methyl-tert-butyl ether for high-throughput lipidomics.* J Lipid Res, 2008. **49**(5): p. 1137-46.

63. Pavlides, J.M.W., et al., *Predicting gene targets from integrative analyses of summary data from GWAS and eQTL studies for 28 human complex traits.* Genome medicine, 2016. **8**: p. 1-6.

64. Zhu, Z., et al., *Integration of summary data from GWAS and eQTL studies predicts complex trait gene targets.* Nature genetics, 2016. **48**(5): p. 481-487.

65. Cadby, G., et al., *Comprehensive genetic analysis of the human lipidome identifies loci associated with lipid homeostasis with links to coronary artery disease.* Nature communications, 2022. **13**(1): p. 3124.

66. Li, H.-J., et al., *Further confirmation of netrin 1 receptor (DCC) as a depression risk gene via integrations of multi-omics data.* Translational psychiatry, 2020. **10**(1): p. 98.

67. Hemani, G., et al., *The MR-Base platform supports systematic causal inference across the human phenome.* elife, 2018. **7**: p. e34408.

68. Crooke, S.T., et al., *RNA-Targeted Therapeutics.* Cell Metab, 2018. **27**(4): p. 714-739.

69. Santhekadur, P.K., D.P. Kumar, and A.J. Sanyal, *Preclinical models of non-alcoholic fatty liver disease.* J Hepatol, 2018. **68**(2): p. 230-237.

70. Van Herck, M.A., L. Vonghia, and S.M. Francque, *Animal Models of Nonalcoholic Fatty Liver Disease-A Starter's Guide.* Nutrients, 2017. **9**(10).

71. Ito, M., et al., *Longitudinal analysis of murine steatohepatitis model induced by chronic exposure to high-fat diet.* Hepatol Res, 2007. **37**(1): p. 50-7.

72. Svegliati-Baroni, G., et al., *A model of insulin resistance and nonalcoholic steatohepatitis in rats: role of peroxisome proliferator-activated receptor-alpha and n-3 polyunsaturated fatty acid treatment on liver injury.* Am J Pathol, 2006. **169**(3): p. 846-60.

73. Mari, M., et al., *Mitochondrial free cholesterol loading sensitizes to TNF- and Fas-mediated steatohepatitis.* Cell Metab, 2006. **4**(3): p. 185-98.

74. Savard, C., et al., *Synergistic interaction of dietary cholesterol and dietary fat in inducing experimental steatohepatitis.* Hepatology, 2013. **57**(1): p. 81-92.

75. Tirosh, O., *Hypoxic Signaling and Cholesterol Lipotoxicity in Fatty Liver Disease Progression.* Oxid Med Cell Longev, 2018. **2018**: p. 2548154.

76. Hui, S.T., et al., *The Genetic Architecture of Diet-Induced Hepatic Fibrosis in Mice.* Hepatology, 2018. **68**(6): p. 2182-2196.

77. Matsuzawa, N., et al., *Lipid-induced oxidative stress causes steatohepatitis in mice fed an atherogenic diet.* Hepatology, 2007. **46**(5): p. 1392-403.

78. Anstee, Q.M., G. Targher, and C.P. Day, *Progression of NAFLD to diabetes mellitus, cardiovascular disease or cirrhosis.* Nat Rev Gastroenterol Hepatol, 2013. **10**(6): p. 330-44.

79. Kleiner, D.E., et al., *Design and validation of a histological scoring system for nonalcoholic fatty liver disease.* Hepatology, 2005. **41**(6): p. 1313-21.

80. Friedman, S.L., *Molecular regulation of hepatic fibrosis, an integrated cellular response to tissue injury.* J Biol Chem, 2000. **275**(4): p. 2247-50.

81. Leonarduzzi, G., et al., *The lipid peroxidation end product 4-hydroxy-2,3-nonenal up-regulates transforming growth factor beta1 expression in the macrophage lineage: a link between oxidative injury and fibrosclerosis.* FASEB J, 1997. **11**(11): p. 851-7.

82. Scott, C.L., et al., *Bone marrow-derived monocytes give rise to self-renewing and fully differentiated Kupffer cells.* Nat Commun, 2016. **7**: p. 10321.

83. Balwani, M., et al., *Phase 3 Trial of RNAi Therapeutic Givosiran for Acute Intermittent Porphyria.* N Engl J Med, 2020. **382**(24): p. 2289-2301.

84. Snel, M., et al., *Ectopic fat and insulin resistance: pathophysiology and effect of diet and lifestyle interventions.* Int J Endocrinol, 2012. **2012**: p. 983814.

85. Janssen, J., *Overnutrition, Hyperinsulinemia and Ectopic Fat: It Is Time for A Paradigm Shift in the Management of Type 2 Diabetes.* Int J Mol Sci, 2024. **25**(10).

86. Miyake, K., et al., *Hyperinsulinemia, glucose intolerance, and dyslipidemia induced by acute inhibition of phosphoinositide 3-kinase signaling in the liver.* J Clin Invest, 2002. **110**(10): p. 1483-91.

87. Yamauchi, T., et al., *Targeted disruption of AdipoR1 and AdipoR2 causes abrogation of adiponectin binding and metabolic actions.* Nat Med, 2007. **13**(3): p. 332-9.

88. Maffeis, C., et al., *Insulin sensitivity is correlated with subcutaneous but not visceral body fat in overweight and obese prepubertal children.* J Clin Endocrinol Metab, 2008. **93**(6): p. 2122-8.

89. Kamagate, A., et al., *FoxO1 mediates insulin-dependent regulation of hepatic VLDL production in mice.* J Clin Invest, 2008. **118**(6): p. 2347-64.

90. Kim, D.H., et al., *FoxO6 integrates insulin signaling with MTP for regulating VLDL production in the liver.* Endocrinology, 2014. **155**(4): p. 1255-67.

91. Hirano, T., et al., *Apoprotein C-III deficiency markedly stimulates triglyceride secretion in vivo: comparison with apoprotein E.* Am J Physiol Endocrinol Metab, 2001. **281**(4): p. E665-9.

92. Horn, C.L., et al., *Role of Cholesterol-Associated Steatohepatitis in the Development of NASH.* Hepatol Commun, 2022. **6**(1): p. 12-35.

93. Chen, Z., et al., *Role of oxidative stress in the pathogenesis of nonalcoholic fatty liver disease.* Free Radic Biol Med, 2020. **152**: p. 116-141.

94. Davey Smith, G. and G. Hemani, *Mendelian randomization: genetic anchors for causal inference in epidemiological studies.* Human molecular genetics, 2014. **23**(R1): p. R89-R98.

95. Ma, D., W. Liu, and Y. Wang, *ApoA-I or ABCA1 expression suppresses fatty acid synthesis by reducing 27-hydroxycholesterol levels.* Biochimie, 2014. **103**: p. 101-8.

96. Su, K., et al., *Acceleration of biliary cholesterol secretion restores glycemic control and alleviates hypertriglyceridemia in obese db/db mice.* Arterioscler Thromb Vasc Biol, 2014. **34**(1): p. 26-33.

97. Jia, W., et al., *Targeting the alternative bile acid synthetic pathway for metabolic diseases.* Protein Cell, 2021. **12**(5): p. 411-425.

98. Sugasawa, T., et al., *One Week of CDAHFD Induces Steatohepatitis and Mitochondrial Dysfunction with Oxidative Stress in Liver.* Int J Mol Sci, 2021. **22**(11).

99. Sakuma, I., et al., *Liver lipid droplet cholesterol content is a key determinant of metabolic dysfunction-associated steatohepatitis.* Proc Natl Acad Sci U S A, 2025. **122**(18): p. e2502978122.

100. Zhang, X., et al., *Defective Phosphatidylglycerol Remodeling Causes Hepatopathy, Linking Mitochondrial Dysfunction to Hepatosteatosis.* Cell Mol Gastroenterol Hepatol, 2019. **7**(4): p. 763-781.

101. Montefusco, D.J., et al., *Non-alcoholic fatty liver disease: Insights from sphingolipidomics.* Biochem Biophys Res Commun, 2018. **504**(3): p. 608-616.

102. Shama, S., et al., *Phosphatidylethanolamines Are Associated with Nonalcoholic Fatty Liver Disease (NAFLD) in Obese Adults and Induce Liver Cell Metabolic Perturbations and Hepatic Stellate Cell Activation.* Int J Mol Sci, 2023. **24**(2).

103. Wang, Y.M., et al., *The mechanism of dietary cholesterol effects on lipids metabolism in rats.* Lipids Health Dis, 2010. **9**: p. 4.

104. Su, K., et al., *The ABCG5 ABCG8 sterol transporter opposes the development of fatty liver disease and loss of glycemic control independently of phytosterol accumulation.* J Biol Chem, 2012. **287**(34): p. 28564-75.

105. Chiang, J.Y.L., et al., *Bile Acid and Cholesterol Metabolism in Atherosclerotic Cardiovascular Disease and Therapy.* Cardiol Plus, 2020. **5**(4): p. 159-170.

106. Pandak, W.M. and G. Kakiyama, *The acidic pathway of bile acid synthesis: Not just an alternative pathway(☆).* Liver Res, 2019. **3**(2): p. 88-98.

107. Biddinger, S.B., et al., *Hepatic insulin resistance directly promotes formation of cholesterol gallstones.* Nat Med, 2008. **14**(7): p. 778-82.

108. Chen, C., et al., *Bile acid profiles in diabetic (db/db) mice and their wild type littermates.* J Pharm Biomed Anal, 2016. **131**: p. 473-481.

109. Mladenic, K., et al., *The "Domino effect" in MASLD: The inflammatory cascade of steatohepatitis.* Eur J Immunol, 2024. **54**(4): p. e2149641.

110. Saraiva, M. and A. O'Garra, *The regulation of IL-10 production by immune cells.* Nat Rev Immunol, 2010. **10**(3): p. 170-81.

111. Cintra, D.E., et al., *Interleukin-10 is a protective factor against diet-induced insulin resistance in liver.* J Hepatol, 2008. **48**(4): p. 628-37.

112. Huang, Y.H., et al., *Interleukin-10 induces senescence of activated hepatic stellate cells via STAT3-p53 pathway to attenuate liver fibrosis.* Cell Signal, 2020. **66**: p. 109445.

113. Zhou, Y.C., et al., *Adenovirus-mediated viral interleukin-10 gene transfer prevents concanavalin A-induced liver injury.* Dig Liver Dis, 2012. **44**(5): p. 398-405.

114. Tran, S., et al., *Impaired Kupffer Cell Self-Renewal Alters the Liver Response to Lipid Overload during Non-alcoholic Steatohepatitis.* Immunity, 2020. **53**(3): p. 627-640.e5.

115. Zwicker, C., A. Bujko, and C.L. Scott, *Hepatic Macrophage Responses in Inflammation, a Function of Plasticity, Heterogeneity or Both?* Front Immunol, 2021. **12**: p. 690813.

116. Talbott, H.E., et al., *Wound healing, fibroblast heterogeneity, and fibrosis.* Cell Stem Cell, 2022. **29**(8): p. 1161-1180.

117. Ye, C., et al., *MDM2 mediates fibroblast activation and renal tubulointerstitial fibrosis via a p53-independent pathway.* Am J Physiol Renal Physiol, 2017. **312**(4): p. F760-F768.

118. Thomasova, D., et al., *p53-independent roles of MDM2 in NF-κB signaling: implications for cancer therapy, wound healing, and autoimmune diseases.* Neoplasia, 2012. **14**(12): p. 1097-101.

119. Wu, Y., et al., *Nutlin-3 inhibits epithelial-mesenchymal transition by interfering with canonical transforming growth factor-β1-Smad-Snail/Slug axis.* Cancer Lett, 2014. **342**(1): p. 82-91.

120. El-Brolosy, M.A. and D.Y.R. Stainier, *Genetic compensation: A phenomenon in search of mechanisms.* PLoS Genet, 2017. **13**(7): p. e1006780.

121. Lindow, M., et al., *Assessing unintended hybridization-induced biological effects of oligonucleotides.* Nat Biotechnol, 2012. **30**(10): p. 920-3.

122. Kontarakis, Z. and D.Y.R. Stainier, *Genetics in Light of Transcriptional Adaptation.* Trends Genet, 2020. **36**(12): p. 926-935.